5-1-2011

# A three-dimensional heat and mass transport model for a tree within a forest

Jerrell Ray Ballard

# A THREE-DIMENSIONAL HEAT AND MASS TRANSPORT MODEL FOR A TREE WITHIN A FOREST

By

Jerrell Ray Ballard, Jr.

A Dissertation
Submitted to the Faculty of
Mississippi State University
in Partial Fulfillment of the Requirements
for the Degree of Doctor of Philosophy
in Computational Engineering
in the Bagley College of Engineering

Mississippi State, Mississippi

August 2011

A THREE-DIMENSIONAL HEAT AND MASS TRANSPORT MODEL FOR A TREE WITHIN A FOREST

By

Jerrell Ray Ballard, Jr.

Approved:

| | |
|---|---|
| Pasquale Cinnella<br>Professor of Aerospace Engineering<br>(Director of Dissertation) | Edward A. Luke<br>Associate Professor of Computer Science<br>(Committee Member) |
| C. Wayne Mastin<br>Professor Emeritus of Mathematics<br>(Committee Member) | Stacy E. Howington<br>Associate Professor of Civil Engineering<br>(Committee Member) |
| James A. Smith<br>National Aeronautics and<br>Space Administration<br>(Committee Member) | Roger L. King<br>William L. Giles Distinguished Professor<br>Director of the Center for Advanced<br>Vehicular Systems<br>(Graduate Coordinator) |

Sarah A. Rajala
Dean of the Bagley College of Engineering

Name: Jerrell Ray Ballard, Jr.

Date of Degree: August 6, 2011

Institution: Mississippi State University

Major Field: Computational Engineering

Major Professor: Pasquale Cinnella

Title of Study: A THREE-DIMENSIONAL HEAT AND MASS TRANSPORT MODEL FOR A TREE WITHIN A FOREST

Pages in Study: 132

Candidate for Degree of Doctor of Philosophy

A three-dimensional computational tool was developed that simulates the heat and mass transfer interaction in a soil-root-stem system (SRSS) for a tree in a seasonally varying deciduous forest. The development of the SRSS model involved the modification and coupling of existing heat and mass transport tools to reproduce the three-dimensional diurnal internal and external temperatures, internal fluid distribution, and heat flow in the soil, roots, and stems. The model also required the development of a parallel Monte-Carlo algorithm to simulate the solar and environmental radiation regime consisting of sky and forest radiative effects surrounding the tree. The SRSS was tested, component-wise verified, and quantitatively compared with published observations.

The SRSS was applied to simulate a tree in a dense temperate hardwood forest that included the calculations of surface heat flux and comparisons between cases with fluid flow transport and periods of zero flow. Results from the winter simulations indicate that the primary influence of temperature in the trunk is solar radiation and radiative energy from the soil and surrounding trees. Results from the summer simulation differed with previous results, indicating that sap flow in the trunk altered the

internal temperature change with secondary effects attributed to the radiative energy from the soil and surrounding trees. Summer simulation results also showed that with sap flow, as the soil around the roots become unsaturated, the flow path for the roots will be changed to areas where the soil is still saturated with a corresponding increase in fluid velocity.

# DEDICATION

To my lovely wife, Elizabeth, without her support none of this would have been possible.

ACKNOWLEDGEMENTS

The author would like to express his gratitude to his major professor, Dr. Pasquale Cinnella, for his guidance, understanding, and willingness to work with a non-traditional graduate student. Dr. Cinnella was always available to discuss plans and guidance essential to the completion of this work. Next, the author would like to thank Dr. Stacy E. Howington for providing entertaining discussions regarding modifying fluid flow in porous media. Next, the author would like to thank his long-time mentor, Dr. James A. Smith, for sharing his deep interest of the thermal physics of trees and instilling the confidence to pursue this problem. Finally, the author would also like to thank his committee members for their advice and encouragement during the development of this work. Funding and data for this research was provided by the U. S. Army Engineer Research and Development Center.

The author expresses his thanks to his family and the sacrifices that they have made during this endeavor. He could not have finished this program without their love and support.

TABLE OF CONTENTS

Page

LIST OF TABLES

LIST OF FIGURES

# NOMENCLATURE

*Variables*

| | |
|---|---|
| $A$ | area, ($m^2$) |
| $A_j$ | surface area of surface *j*, ($m^2$) |
| $a$ | square root of porosity, (%) |
| $b$ | weighting bridge factor, (0-1) |
| $c$ | specific heat ( $J\ kg^{-1}\ K^{-1}$ ) |
| $C_p$ | specific heat at a constant pressure ( $J\ kg^{-1}\ K^{-1}$ ) |
| $E_{bj}$ | blackbody emissive power of surface *j*, ($W/m^2$) |
| $e$ | energy associated with each packet in the Monte-Carlo method (W) |
| $F_{i,j}$ | view factor from surface *i* to surface *j*, (%) |
| $G$ | specific gravity (dimensionless) |
| $I$ | total radiative energy received on a surface, ($W/m^2$) |
| $i_b$ | total blackbody intensity, (W) |
| $K_\varepsilon$ | Kersten number, (dimensionless) |
| $k$ | thermal conductivity, ( W/(m K) ), also permeability ($m^2$) |
| $k_r$ | normalized soil thermal conductivity, (dimensionless) |
| $M$ | volumetric moisture content, ( $m^3\ m^{-3}$ ) |
| $N_e$ | total number of discrete energy packets simulated in Monte-Carlo method |
| $n_j$ | number of discrete energy packets emitted by a surface in the Monte-Carlo method |
| $n_j^*$ | number of discrete energy packets received by a surface in the Monte-Carlo method |
| $\mathrm{Pe}_x$ | Péclet number, (dimensionless) |
| $q_j$ | heat flux of surface *j*, ($W/m^2$) |
| $R$ | distance between two surfaces, (m) |
| $S_M$ | normalized soil water content, (dimensionless) |
| $S_r$ | residual saturation of the soil, ( $m^3\ m^{-3}$ ) |
| $S_s$ | soil specific storage, ($m^{-3}$) |

| | |
|---|---|
| $T$ | temperature, (K) |
| $T_j$ | temperature of surface *j*, (K) |
| $t$ | time |
| $V$ | volume, ($m^3$) |
| $v$ | volumetric content of a medium, ($m^3\,m^{-3}$) |
| W | source or sink flux |
| $w_i$ | weighting factor, (0-1) |
| $x, y, z$ | Cartesian coordinates |

*Greek symbols*

| | |
|---|---|
| $\alpha$ | thermal diffusivity, (%), also soil texture parameter |
| $\varepsilon$ | emissivity, (%) |
| $\kappa_r$ | relative permeability, (%) |
| $\lambda$ | spectral wavelength, (nm) |
| $\nu$ | kinematic viscosity, ($m^2s^{-1}$) |
| $\xi$ | porosity, (%) |
| $\Pi$ | osmotic potential, (MPa) |
| $\rho$ | density, ($kg/m^3$), also spectral reflectance, (%) |
| $\sigma$ | Stefan-Boltzman constant, ($W/(m^2K^4)$) |
| $\psi$ | water potential, (MPa), also pressure head (m) |

*Subscripts*

| | |
|---|---|
| $\parallel$ | parallel |
| $\perp$ | perpendicular |
| *B* | bark |
| *dry* | dry |
| *eff* | effective |
| *ext* | external |
| *gas* | gas |
| $H_2O$ | water |
| *rad* | radiative energy |
| *S* | soil, also water storage |
| *sat* | saturated |
| *solid* | solid |
| *wet* | wet |
| *W* | wood |

# CHAPTER I

# INTRODUCTION

Forests have significant effects on the earth's energy balance, hydrologic cycle, and carbon balance. The forests impact the local meteorological conditions by the exchange of water and carbon dioxide through evapotranspiration and respiration processes [1-7] and heat storage [8]. They alter the earth's surface albedo by the reflection and absorption of different wavelengths of the solar radiation spectrum [9-11]. At a global scale, forests play an important part in the earth's carbon balance: they sequester carbon and release it [12-13]. At regional scales, the spatial and temporal variation of near-surface air flow is altered by the geometry and shape of the tree crowns [14-17]. And at a local scale, forests and trees impact the movement of water and contaminants in the soil, where now specific tree species are used in phytoremediation studies to absorb and degrade organic contaminants and certain heavy metals from the soil [18-22]. To facilitate our understanding of the importance and impact of these effects, modeling and simulation of these processes is often used in both large- and small-scale studies.

## 1.1 Motivation

For more than 100 years, researchers have observed that the temperature and moisture regimes are important components in forest ecosystem dynamics. For example, the distribution of temperature and moisture content within the tree influences its growth and development [23], the onset and cessation of cambial activity [24], its capability to

prevent insect predation [25-27], and the population dynamics of the parasitic insects [28-29]. Moreover, temperature directly affects the uptake and metabolism of pollutants from the soil into the tree tissue [19, 21]. For certain avian species and bats, the orientation of tree cavities used for nesting and the selection of tree size for excavating such cavities are crucial for success of the population [30-32]. Specifically, studies showed that the microclimate of the south-facing nesting cavities is warmer than similar north-facing cavities, and thus the adult birds and nestlings expend less energy to keep warm and improve their survival [32]. With respect to tree growth and survival, observations showed that soil and atmospheric temperatures are significant parameters that limit the growth of trees and set treeline elevation limitation [33-36].

In addition to forest growth and affected fauna, the moisture content of the soil and forest is also important during forest fires. The ability of the tree bark to protect the inner cambial layer from fire determines the survival of the individual tree [37]. In the late 1950s and early 1960s, researchers began to study and measure the heating of tree trunks during forest fires [37-38] and explored modeling trunk temperatures [39-40]. These measurements are used as guidelines today to determine the mortality rates of different tree species.

Throughout these studies, the individual thermal and hydraulic processes that occur in the soil, roots, and tree were measured and modeled. Simulations typically consisted of simple one- and two-dimensional abstractions. These processes are rarely modeled in a coupled centimeter-scale three-dimensional environment. Where high-resolution computations are reported in literature [41-44], they either focus on heat transport or fluid flow, but not both. Throughout the literature, researchers [40-41, 43, 45] indicated a desire to simulate a coupled heat and moisture flow three-dimensional

system, but the computational technology to do so was unavailable. To address this need, this dissertation documents the development of a computational tool that provides current and future researchers the capability to simulate the three-dimensional spatial and temporal interaction of thermal and hydraulic processes among the soil, roots, and tree.

## 1.2 Objectives

This research has two principal objectives. One objective is to develop a three-dimensional computational tool that simulates the radiative energy, conductive heat, and mass transfer interaction in a soil-root-stem system (SRSS). A simplistic diagram of the interacting processes is shown in Figure 1.1. The development of the SRSS model involved modifying and coupling existing heat and mass transport tools to create a specific application capable of reproducing the three-dimensional diurnal, internal, and external temperatures, internal fluid distribution, and heat flow in the soil, roots, and stems (tree trunk[1]). Additionally described is a technique developed to account for and simulate the varying external radiation regime within the forest that surrounds the SRSS.

The second objective of this research is to verify the components of the SRSS through comparisons with published and newly measured field data, ultimately presenting the simulation results applied to a seasonally varying deciduous forest in a temperate environment.

[1] Tree trunk and stem will be used interchangeably in this document. Basically, trunks are large stems.

The purpose of the SRSS model is to answer these questions.

1. *Is the SRSS model sufficiently accurate to simulate the physics of thermal radiation without explicitly modeling the entire forest?*
2. *During periods of high mass transfer, how much heat is transported by the fluid flow in the stem compared to conduction and radiative effects?*
3. *What is the effect of the root system on the spatial and temporal distributions of temperature and moisture content in the soil?*

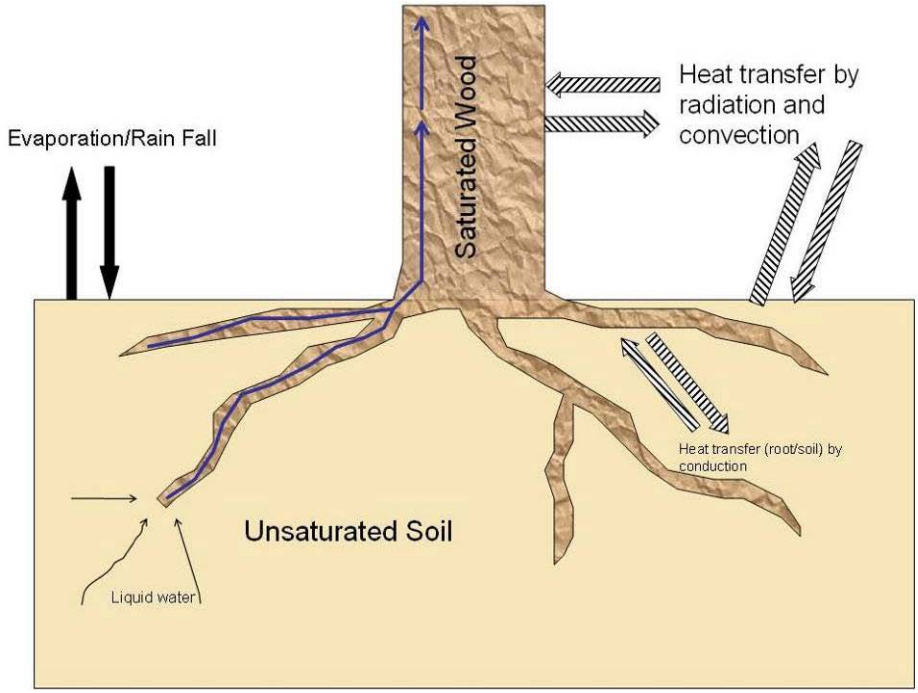


Figure 1.1 Schematic of the Soil-Root-Stem System (SRSS) Model

## 1.3 Description of the Soil-Root-Stem-System

The Soil-Root-Stem-System (SRSS) is a three-dimensional, unsteady simulation solving simultaneous heat and mass transfer in porous media. The SRSS considers all the properties of the materials in the simulation to be time-varying and dependent on moisture content and temperature. The soil, root, and stem materials are treated as a

continuum with effective hydraulic and thermal properties based on the composition of solids, water, and air in the material. Fluid movement through these materials occurs as bulk fluid flow driven by pressure gradients. For radiative heat calculations, all external surfaces are treated as spectrally diffuse grey black bodies.

### 1.4 Technical Contributions of the Proposed Study

The governing equations for thermal and mass transport used in this research are well described and analyzed in the literature. Therefore, it is not the purpose of this research to develop new equations but to provide a robust computational engineering tool that will advance the science of tree physiology and forest ecology, and to apply this tool to explore the relative importance of the many fluid flow and thermal processes in a SRSS. Several examples are in the literature [40-41, 46, 45] where researchers expressed a strong interest in modeling the complete system in three dimensions at centimeter scales but were unable to accomplish this task, due in part to a lack of computational tools. Therefore, the main technical contributions of the proposed research are:

- A computational tool that simulates the heat and moisture interactions for a soil-root-tree system at a discretization scale of a few centimeters.
- Application of this tool to:
    - Three-dimensional convective heat transport by sap flow in the living wood tissue;
    - Diurnally and spatially varying soil moisture due to the evaporative demand by the root-tree system;
    - Three-dimensional radiative energy budget for the surface soil and stem with interaction to the surrounding forest and canopy.

## 1.5 Dissertation Outline

This document is organized in three parts. The first part is the introduction of the work and literature review discussed in Chapters 1 and 2. The second part (Chapters 3 and 4) is the description of the SRSS and verification of the SRSS subcomponents. The final part (Chapters 5 and 6) is the numerical simulation of the SRSS and analysis of the results of the simulation applied to a conceptual system of a deciduous tree in a mature canopy forest. Finally, some conclusions are drawn in Chapter 7, including recommendations for future work.

# CHAPTER II

# BACKGROUND AND LITERATURE REVIEW

The purpose of this chapter is to introduce the background of the research, describe the terminology used throughout this document, and provide a historical context of published literature pertaining to this subject.

## 2.1 Background and Terminology

This section provides a descriptive framework of the three main study areas explored in the SRSS, i.e., radiation in the forest environment, soil science, and plant physiology.

### 2.1.1 Radiation in the Forest Environment

All matter in nature emits electromagnetic radiation. This emitted electromagnetic radiation spans the full electromagnetic spectrum, but 99% of the terrestrial radiation is confined between 0.2 and 100.0 μm. The maximum peak of the emitted spectral radiation is determined by the temperature of the matter and is described by Planck's Law.

In discussions of this research, the radiative flux from the continuous spectral solar and environmental radiation is divided into two regions; shortwave and longwave radiation. The shortwave radiation covers the 0.2 to 3.0 μm wavelengths and is significant for plant development and growth. The longwave radiation, spanning from 3.0 to 100.0 μm, describes the visible to near-infrared wavelengths.

Efficiency of radiation flux into an object is affected by the spectral absorption, transmission, and reflection of the surface properties. Radiation power is defined as the amount of radiant energy emitted, transmitted, or absorbed per unit time. Radiative flux is defined as the amount of energy transferred per unit area of a surface. The spectral absorption (or absorptivity) of a surface is defined as the fraction of incident radiation flux at a given wavelength that is absorbed by the surface. The spectral reflectivity, $\rho$, of a surface is defined as the fraction of incident radiation flux at a given wavelength that is reflected by the surface. The spectral transmission (transmissivity) of a surface is defined as the fraction of incident radiation flux at a given wavelength that is transmitted by a surface.

In the forest environment, solar radiation is the principal source of shortwave radiation while the longwave sources are about equally distributed between solar, atmospheric, and environmental sources [47]. For all of these sources, the primary receptors of the radiative flux are the soil, wood, and foliage. Of these three, only foliage has a transmission fraction that is greater than zero.

### 2.1.2 Soil Physiology

The soil is modeled as a macroscopic porous medium that can be both saturated and unsaturated with fluid. The Darcian flux through this porous medium is defined as the volume of fluid passing through a unit cross-sectional porous area per unit of time [48] and is determined by the fluid pressure gradient, fluid viscosity, fluid density, hydraulic conductivity, and gravity.

Soil has three primary interrelated thermal properties: thermal conductivity, thermal diffusivity, and heat capacity. Thermal conductivity is defined as the property of

a material to conduct heat, thermal diffusivity is the rate at which heat flows through a material, and heat capacity is defined as the property of a material to store internal energy. Common to each of these properties for soils is that the property is determined by the porosity, moisture content, and thermal conductivity of the solid matter in the soil volume. In a dynamic unsaturated soil environment, these properties can vary significantly during a 24-hour cycle.

### 2.1.3 Plant Physiology

In a vascular plant system, the xylem and phloem cell structures are present throughout the plant and are responsible for most of the fluid transport in the system. Primarily, the xylem transports water and nutrients from the soil up through the roots to the rest of the plant [49-50]. Similarly in a reverse manner, the phloem transports nutrients down from the photosynthetic members (primarily leaves) through the plant and eventually to the root system. Located between these two vascular systems is meristemic tissue that is called the vascular cambium. The vascular cambium tissue is one of the growth regions of the plant and produces both xylem and phloem cells. In the trunk and root region of a plant, the continued growth in the cambium tissue increases the circumference of the plant. Depending on the seasonal growth, the cambium tissue produces large or small xylem cells that appear as annual growth rings [49].

## 2.2 Literature Review

Because of the interdisciplinary nature of this research, the following literature review consists of published work conducted within both the engineering and biological disciplines. The literature review is divided by the nature of the work, i.e., experiments and their resulting measurements and theoretical and analytical models.

### 2.2.1 Tree Temperature Experiments and Measurements

Early studies of heat flow through trees were primarily focused on mortality rates of trees during forest fires or severe freezing events. Forest fire events were of particular importance to forest managers and botanists for the determination of tree resistance to fire damage.

In 1964, Fahnestock and Hare [37] instrumented live longleaf pine trees and measured cambium temperatures of trees exposed to prescribed burning. One of their conclusions from their experiments indicated that the leeward side (facing away from the fire) of the tree was subjected to more intense heating than the windward side (facing the fire) due to natural convection processes. Thermal measurements under the bark during a controlled burn ranged from an average of 380 deg C windward and 700 deg C leeward.

Vines [38] studied fire resistance in Australian eucalypts trees in 1968 and made several measurements of cambium temperatures of living trees in different fire settings. Vines noted that the rate of change in cambium temperature was related to the bark's thermal diffusivity, bark structure, and bark moisture content. Within the same time period, Gill and Ashton [51] conducted a laboratory study in 1968 to observe fire resistance of three different types of Victorian eucalypts that possessed different types of bark. Their laboratory approach used radiant heaters and measured the rise and fall of temperatures in the bark, phloem, and xylem.

Studies of the thermal conductivity and diffusivity of live fruit trees was conducted by Turrell et al. [52-53] between 1962 and 1967 to explore the effects of freezing temperatures on crop citrus trees. Their measurements and subsequent analysis provided tables and functions to estimate the time required for various diameters of citrus tree branches to reach to -8 deg C and develop permanent tissue damage.

Similarly, Derby and Gates [40] in 1964 measured normal diurnal temperatures of apple and peach trees in orchards and aspen trees at high elevations to observe the freezing and thawing effects on cambial temperatures and compared these data with the results from a two-dimensional finite difference model. The observed temperature in the wood ranged from 10 – 12 deg C.

From 1964-1969, Herrington [39, 54] developed specific techniques for internal temperature measurements of softwood and hardwood trees using carefully placed thermocouples. Using these measurements, he developed an analytical model that predicted the diurnally varying temperatures in the trunks.

From the mid-1960's to the present time, the procedures and overall purposes for observing internal tree temperatures have not significantly changed. In examples of recent work by Li [30] in 1991 and Wiebe [32] in 2001, both authors use internal tree temperature measurements to characterize the suitability of tree cavities for nesting by various boreal animals. Observations by Wiebe showed daily cavity temperatures ranging from 2.2 to 22.1 deg C during July 1998 in British Columbia.

### 2.2.2 Tree Hydraulic Experiments and Measurements

Since before the 1900's, the scientific community has studied and analyzed fluid (sap) flow through plants and trees for various purposes such as syrup production and understanding the significance of transpiration [55]. In 1933, Woodhouse [56] coined the term "sap hydraulics" which describes the study of entrance of water into the roots, passage of fluid through the plant, and exit of water through the leaves. Water uptake by the plant roots is determined by several factors [42]. Some of these factors include the hydraulic conductivity of the soil, hydraulic conductivity of the wood, root system

architecture, moisture content of the soil, and absorption capability of the roots. Accurate measurements of plant water use were difficult to obtain and were not commonly conducted until recently. Swanson [57] has an excellent description of the historical techniques used to determine plant water use and mentions that the first reported use of heat as a tracer to indicate flow was conducted by Huber in 1932. Huber placed a heat source on the stem and measured temperature changes upstream and downstream in the sap flow. The distance between the heated probe and the temperature measurement (thermocouple) was divided by the measured time to obtain fluid velocity. In 1958, Marshall [58] conducted similar studies but used an implanted heater rather than a surface heater. Additionally, Marshall conducted a theoretical analysis and calculated the sap flux and the rate of sap flow per unit area of xylem. This heated pulsed probe method became popular in the mid-1980s and is now commonly used. Using this method or similar methods (steady diffusive techniques), researchers frequently measure water uptake from roots and radial spatial distribution throughout individual trees [59-65].

### 2.2.3 Tree Thermal Simulations

Early interest in the temperature distribution within trees came partly because of the difficulty in the ability to effectively measure the spatially varying nature of the problem. In these early studies, the common approach to thermal simulation included the classical equations of heat transfer. In 1964, as previously metioned, Herrington [39, 54] conducted measurement studies but also developed an analytical model that predicted temperature and heat flow variations with time as sinusoidal waves or sums of sinusoidal waves. The two-dimensional simulation was represented as a circular cylinder with no radiation heat exchange on the surface, and the temperature at any point in the trunk was

specified by its axial, radial, and angular coordinates. Near the same time, Derby and Gates [40] developed a finite difference model in 1966 based on Dusinberre's [66] finite difference heat transfer calculations in two dimensions. From that time until the early 1990's, there appears to be little progress in the literature with regard to thermal modeling of trees. In 1990, Rego and Rigolot [67] developed a one-dimensional simulation to calculate the heat flow into a trunk to predict cambium damage by a fire. One year later in 1991, Hummel et al. [41] extended Derby and Gates method into three dimensions and changed the solver method to a Crank-Nicholson finite difference method. In this method, a branch or trunk was represented by a cylinder composed of single prisms that spanned the length. Their simulations were not coupled to the soil or roots and did not include fluid flow. In 2002, Potter and Andresen [68] described a two-dimensional finite difference model of a horizontal section of a tree stem that closely duplicates the work by Derby and Gates but included sensitivity analyses of the model parameters.

Finally, some of the recent work reported in the scientific literature was conducted by Jones in 2003. In Jones' thesis [46] and later publication [45], a one-dimensional temperature simulation of a tree trunk during a forest fire is described. This work is notable because it is the first simulation to simultaneously account for bark and wood swelling, devolitization, charring, desiccation, and moisture variability during burning. Additionally, this work includes the temperature and moisture dependence of the thermal conductivity and the heat capacity of the wood and bark as described by Simpson and TenWolde [69] and Martin [70].

### 2.2.4 Tree Hydraulic Simulations

Water uptake and transport in trees is a hydraulic flow process that is controlled by resistances in the flow system and hydraulic gradients. Understanding the hydraulic resistances in a soil and tree system is one of the more important aspects of the SRSS. In a 1965 paper published by Cowan [71], the pathways of water transport in the soil and plant are represented by electrical analogues (Figure 2.1).

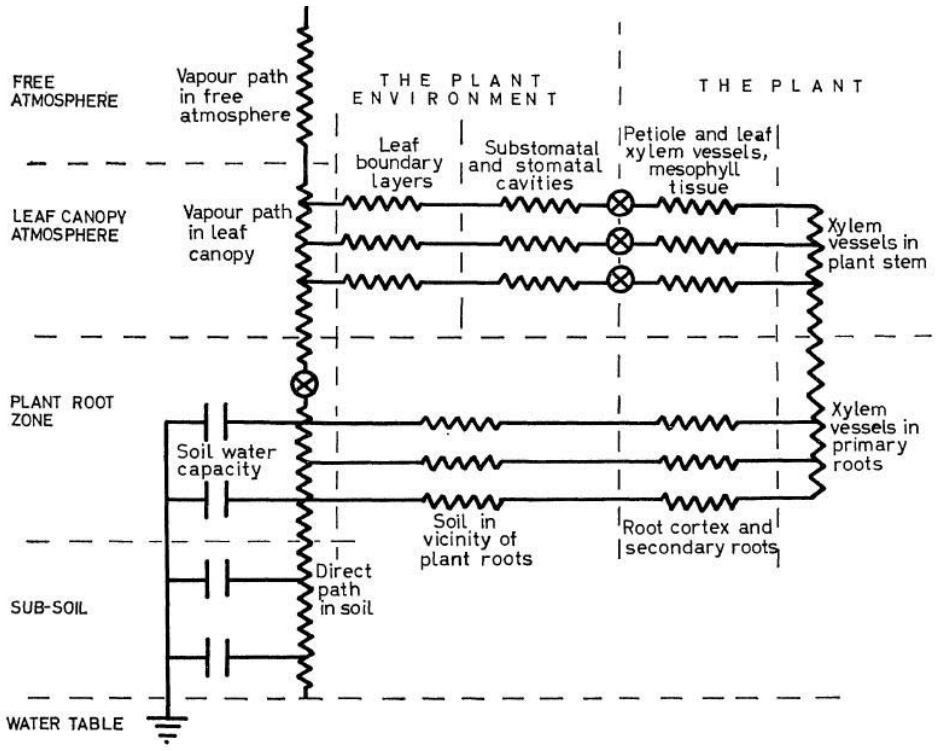


Figure 2.1 Water transport path as described by Cowan [71]

In work by Farnum and Carey [72] in 1981, the two-dimensional water transport in a soil-plant was modeled through finite element analyses. The resulting model analyzed the diffusion rates between the different components of the soil-plant system and was solved using a Galerkin semi-discrete finite element method.

With recent advances in the ability to measure and monitor plant fluid flows and resistances, the traditional view of plant hydraulics is expanding to include the dynamic response of xylem flow resistance to environmental conditions. The most recent work by Sperry et al. [73-75] improved our understanding of how these hydraulic resistances change with soil and plant water content, thus also improving our ability to predict how the plant water use responds to environmental conditions.

### 2.2.5 Soil Thermal Simulations

One of the most widely cited and referenced work in soil thermal simulations is the work conducted by Deardorff in 1978, where he presents the framework of a one-dimensional surface temperature model coupled with a layer of vegetation [76]. In this paper, Deardorff presents a time-dependent equation for predicting the surface and subsurface temperatures of a 12-layer soil model and compares its results with those from five other approximate models. The energy balance method used also includes the presence of a layer of vegetation to account for changes in the evaporation and radiation regime. Oke [47], Campbell [77-78], and Buchan [79] presented variations in the mid-1980's on the soil energy balance model and increased the complexity of the simulation by coupling in atmospheric conditions, vegetation canopies, and improved forced convection conditions. Since these model and simulation studies, most current research is focused on global coupled soil-water-atmosphere transfer models [80-82].

### 2.2.6 Thermal Conductivity Theoretical Models

In this subsection, two types of thermal conductivity models are discussed: wood thermal conductivity models and soil thermal conductivity models. Because both are

modeled as porous media, models typically share common properties such as moisture content, density, and porosity.

To correctly model the heat flow and effects of moisture in heterogeneous wood, the thermal properties of the material must be quantified. Of these properties, thermal conductivity ($k$), moisture content ($M$), density ($\rho$), and porosity ($\xi$) are considered to be the most important.

Since wood has a heterogeneous structure (Figure 2.2 for example), the thermal characteristics are significantly anisotropic with regard to heat flow perpendicular, tangent, or parallel to the growth axis of the wood. As a general rule, the parallel thermal conductivity is typically 1.5 to 2.5 times greater than the perpendicular thermal conductivity.

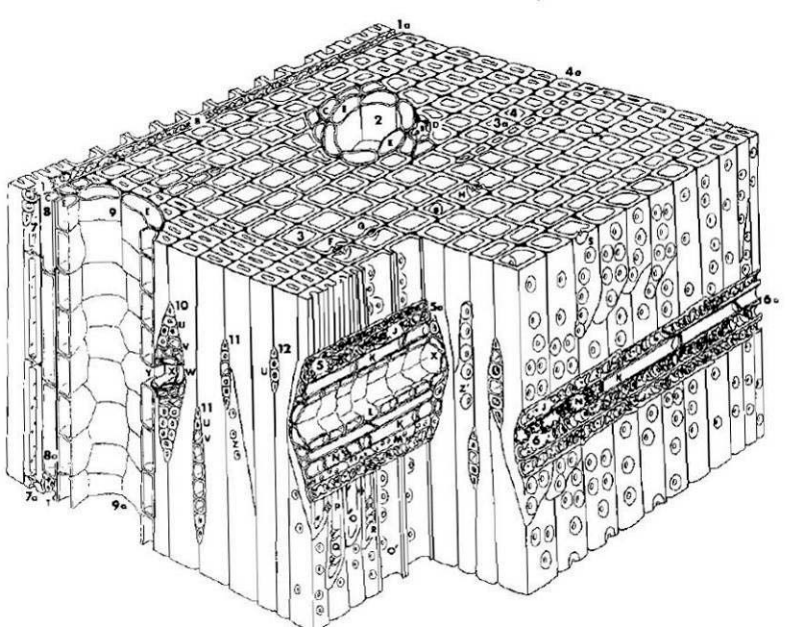

Figure 2.2 Structure of southern pine softwood from Siau [83]

In 1941, MacLean [84] measured the thermal conductivity of wood with varying moisture contents by the hot-plate (steady-state) method. From these measurements, two different empirical equations were developed based on moisture content and the porosity of the wood. For wood moisture content ($M$) of < 40%, the first empirical equation is

$$k_{W\perp} = [G(5.18 + 0.096M) + 0.57\xi)] \times 10^{-4} \text{ cal/(cm K sec)} \quad (0.1)$$

For a wood moisture content of > 40%, the second empirical equation is

$$k_{W\perp} = [G(5.18 + 0.131M) + 0.57\xi)] \times 10^{-4} \text{ cal/(cm K sec)} \quad (0.2)$$

where $k_{W\perp}$ is the thermal conductivity perpendicular to the wood grain, and G is the specific gravity of the wood. The increased coefficient for M in Equation (2.2) accounts for the increased thermal conductivity of "free water" as opposed to bound water in the cells. To calculate thermal conductivity parallel to the wood grain, MacLean approximated that it increased roughly 2.5 times so that it becomes

$$k_{W\square} = 2.5 k_{W\perp} \quad (0.3)$$

In one of the first studies of the thermal properties of tree bark, Martin [70] developed in 1963 empirical moisture and temperature relationships for the thermal properties of tree bark using a heated probe method for three pine and seven hardwood species. The empirical equation for thermal conductivity of bark ($k_B$) (converted to SI units[46]) is

$$k_B = 0.0419\left[0.005026\rho_{Bdry} + 0.013241\rho_{Bwet} + 0.0078(T_B - 273.15) - 0.397\right] \quad (0.4)$$

where $\rho_{Bdry}$ is the density of the dry bark ($\text{kg m}^{-3}$), $\rho_{Bwet}$ is the bark moisture density, and $T_B$ is the bark temperature (K). In this study, the difference in thermal conductivity between parallel and perpendicular to the wood grain was not as significant. About the same time, Siau developed a wood thermal conductivity model based on the cellular

geometry of the wood [85-86, 83] and compared its results with previously published measurements [84]. This model is

$$k_{W\perp} = \frac{(1-a)k_{W_{solid}}^2 + ak_{gas}k_{W_{solid}}}{(1-a)^2 k_{W_{solid}} + a(1-a)k_{gas} + a^2 k_{W_{solid}}} \tag{0.5}$$

where the parameter $a$ is equal to the square root of porosity $\left(a = \sqrt{\xi}\right)$. Siau [87] also refined MacLean's [84] empirical model for the perpendicular thermal conductivity such that

$$k_{W\perp} = G(0.2 + 0.0038M) + 0.024\,. \tag{0.6}$$

Siau's development was a departure from empirical models to a model that considered the physiology of the wood.

In recent times, the majority of thermal models in the literature use the physiology of wood as a basis. Examples of this are the works by Suleiman et al. [88] and Gu [89-92]. In 1999, Suleiman et al. [88] published a wood thermal conductivity model that used a weighting bridge-factor between two limiting cases. The effective thermal conductivity ($k_{Beff}$) is modeled as

$$k_{Beff} = bk_{B\square} + (1-b)k_{B\perp} \tag{0.7}$$

where $b$ is the weighting bridge factor (0-1), $k_{B\square}$ is the parallel thermal conductivity, and $k_{B\perp}$ is the perpendicular thermal conductivity. The parallel thermal conductivity is defined as

$$k_{B\square} = (1-\xi)k_{B_{solid}} + \xi\left(k_{gas} + k_{rad}\right) \tag{0.8}$$

and the perpendicular thermal conductivity is defined as

$$k_{B\perp} = \left(\frac{(1-\xi)}{k_{B_{solid}}} + \frac{\xi}{k_{gas}}\right)^{-1} \tag{0.9}$$

where $k_{B_{solid}}$ is the solid thermal conductivity (i.e., no voids), and $k_{gas}$ is the air thermal conductivity.

In several publications from 2001-2005, Gu [89-92] describes a microscopic cellular two-dimensional geometric model for wood that incorporated anisotropic thermal properties. This model represents the most recent description of geometric cellular modeling of thermal conductivity where the two-dimensional model includes the cell walls, voids, and free water in the heat flow calculations. In summary, a review of the literature related to the estimation of thermal conductivity of the wood shows that models historically have progressed from empirical equations to physiological models down to cellular simulations. For the proposed work, the cellular model described by Gu [89] is too detailed for the proposed simulation resolution. Thus the effective thermal conductivity model for wood described and subsequently matured by Siau [85-87] (Equation 2.7) is used in this study.

The thermal conductivity of soil varies as a function of temperature, composition, porosity, and moisture content. An example of this is shown in Figure 2.3 from a study by Hiraiwa and Kasubuchi [93]. The soil thermal property theoretical models reviewed in this section are similar to the thermal property models of wood and bark, where the effective thermal conductivity is defined by the individual parts of the medium, i.e., solid, air, and water fraction.

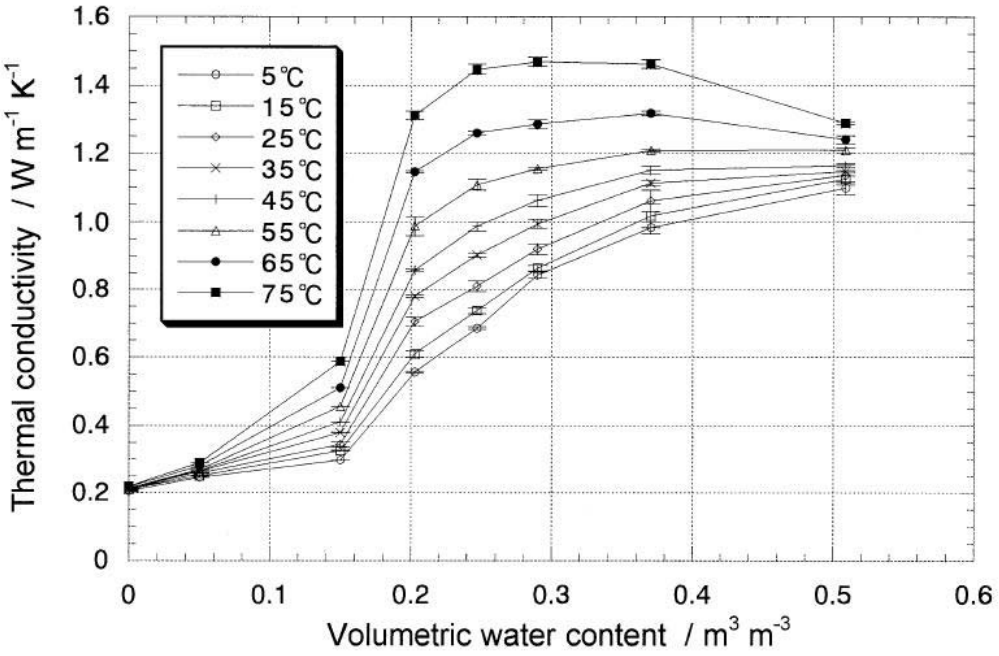


Figure 2.3 An example found in Hiraiwa and Kasubuchi [93] of the soil thermal conductivity variation as a function of temperature and water content

As identified by Cosenza et al. [94], there are four commonly used mathematical expressions to describe the thermal behavior of a mixed porous medium. The first is the simple mixing law,

$$k = \sum_{i=1}^{N} k_i v_i \tag{0.10}$$

where $k_i$ is the thermal conductivity of the $i$th component, $v_i$ is the volumetric content, and $N$ is the number of components in the medium. Similarly, a "series" equation (described by de Vries [95] in 1963) can be used.

$$k = \left( \sum_{i=1}^{N} k_i^{-1} v_i \right)^{-1} \tag{0.11}$$

The third equation is the "geometric" equation,

$$k = \prod_{i=1}^{N} k_i^{v_i} \tag{0.12}$$

where this type of equation is used in thermal conductivity of two-phase saturated media. The fourth equation, referred to as the "quadratic parallel" is

$$k = \left( \sum_{i=1}^{N} v_i \sqrt{k_i} \right)^2 \tag{0.13}$$

The soil thermal conductivity model described by Ochsner et al. [96] in 2001 uses a modified "series" equation described by de Vries [95] described as

$$k = \frac{\sum_{i=0}^{n} w_i k_i v_i}{\sum_{i=0}^{n} w_i v_i} \tag{0.14}$$

where the thermal conductivity of the soil is calculated as the weighted average of the conductivities of the various soil components with the addition of weighting factors. The weighting factors depended on the shape and orientation of the granules of the soil components and on the ratio of the conductivities of the components.

Work published by Cosenza et al. [94] in 2003 proposes that there exists no simple and general relationship between thermal conductivity of a soil and the volumetric water content because of the internal geometry of the porosity and the thermal conductivity of the soil components. They describe several models and polynomial fitting functions that were compared with published experimental data. Of these comparisons, the polynomial fitting and quadratic parallel consistently performed the best.

In 2005, Côté and Konrad [97-98] presented a generalized thermal conductivity model for moist soils that is based on the concept of a normalized thermal conductivity with respect to the dry and saturated states. The model represents the effects of porosity, fluid saturation, mineral content, grain-size distribution, and particle shape. The normalized soil thermal conductivity proposed by Johansen [99] in 1975 is

$$k_r = \frac{k_S - k_{S_{dry}}}{k_{S_{sat}} - k_{S_{dry}}} \tag{0.15}$$

where $k$, $k_{dry}$, and $k_{sat}$ represent actual, dry, and saturated thermal conductivity of the soil, respectively. Côté and Konrad rewrite the normalization as

$$k_S = \left(k_{S_{sat}} - k_{S_{dry}}\right) k_r + k_{S_{dry}} \tag{0.16}$$

and improved the estimation of saturated, dry, and relative thermal conductivity using thermal conductivity of the solid particles and generalized empirical relationships with soil types which are either frozen or unfrozen.

Most recently in 2007, Lu et al. [100] describe a thermal conductivity model defined as

$$k_S = \left(k_{S_{sat}} - k_{S_{dry}}\right) K_e + k_{S_{dry}} \tag{0.17}$$

where the soil thermal conductivity ($k_S$) is defined by the saturated and dry soil thermal conductivity and modified by the Kersten number. The saturated soil thermal conductivity is defined as a combination of solid soil and water thermal conductivity modified by the porosity ($\xi$),

$$k_{S_{sat}} = k_{S_{solid}}^{1-\xi} k_{water}^{\xi} \tag{0.18}$$

the dry soil thermal conductivity is an empirical function defined as

$$k_{S_{dry}} = -0.56\xi + 0.51 \tag{0.19}$$

while the empirically derived Kersten number is redefined by Lu et al. as

$$K_e = \exp\left\{\alpha\left[1 - S_M^{(\alpha - 1.33)}\right]\right\} \tag{0.20}$$

where $\alpha$ is the soil texture parameter, and $S_M$ is the normalized soil water content ($S_M = M / M_{sat}$). The soil texture parameter, as estimated by Lu et al. [100] by fitting measured thermal conductivity and moisture content for multiple types of soils, is 0.96 for coarse-textured soils and 0.27 for fine-textured soils.

This model was compared with a wide range of soils and moisture contents and the results indicated that this model provided improved approximations of soil thermal conductivity compared to other models [100]. Thus equation (2.17) was selected for the soil thermal conductivity model in the SRSS.

# CHAPTER III

## GOVERNING EQUATIONS AND NUMERICAL METHODS

In this chapter, the governing equations for heat, fluid flow, and radiative heat transfer for the SRSS are presented. Additionally, the material mixing functions for specific heat capacity and thermal conductivity are discussed. Finally, some details on the numerical methods employed are provided.

There are several assumptions that are made in the simulations that affect the governing equations. They are:

- The fluid in the system is considered to be of a constant viscosity, density, and slightly compressible throughout the simulation;
- All fluid movement occurs through a porous medium, either in the soil or plant material;
- The simulated velocities within the above assumptions constitute a creeping flow with Reynolds' numbers below 1;
- The soil and plant material are anisotropic and heterogeneous with regard to thermal and hydraulic conductivity;
- Air is always considered to be at atmospheric pressure;
- There is no internal heat generation;
- No radiative heat transfer occurs in the pore space in the solids;

- Within a discretized element of porous media, the temperatures of the water and solid are the same;
- All surfaces are diffuse and are treated as radiative grey diffuse;
- Because of the relatively short distances between surfaces, the air between surfaces neither attenuates nor emits thermal radiation.

## 3.1 Governing Equations

In the SRSS, there are two groups of governing equations that correspond to heat and fluid flow in porous media and radiative energy of surfaces in the system. The heat and fluid flow in porous media equations are centered on the mixed form of Richards' equation, and the radiative energy equations are based in radiation transfer theory.

### 3.1.1 Fluid and Heat Flow Governing Equations

The governing equations of fluid and heat flow in the stem, roots, and soil are based on the conservation principles of mass, momentum, and energy. Because the temperature and water content of the system are time-varying, the use of non-isothermal equations is necessary. The conservation of mass and momentum equations are represented by Richards' equation [101]. The mixed form Richards' equation can be written as

$$S_S S(\psi)\frac{\partial \psi}{\partial t} + \xi \frac{\partial S(\psi)}{\partial t} = \nabla \cdot [K_S \kappa_r(\psi)\nabla(\psi + z)] + W \qquad (0.21)$$

where $S_s$ is the specific storage term that accounts for storage and elasticity of the water and medium in the soil and stem. Water saturation, $S(\psi)$, is the volumetric portion of the pore space filled with water at a pressure head $(\psi)$. The rest of the variables are porosity $\xi$, $K_s$ the water hydraulic saturation conductivity tensor, $\kappa_r(\psi)$ the relative

permeability function of the media, and $W$ the source term. The unknown term for this equation is pressure head. The water saturation function is described as

$$S(\psi) = S_r + \frac{(1 - S_r)}{\left[1 + (\alpha\psi)^n\right]^m} \tag{0.22}$$

where $S_r$ is the residual saturation in the media, and $\alpha, n,$ and $m$ are parameters specifically related to the porous media determined experimentally. The water saturation function is only valid if $\psi \leq 0$. From results by van Genuchten [102], the value of $m$ is assumed to be $m = 1 - 1/n$. The relative permeability function, $\kappa_r(\psi)$, is defined as

$$\kappa_r(\psi) = \frac{\left[1 - (\alpha\psi)^{n-1}\left[1 + (\alpha\psi)^n\right]^{-m}\right]^2}{\left[1 + (\alpha\psi)^n\right]^{m/2}} \tag{0.23}$$

For a representative control volume, the governing equation for energy is as follows [103].

$$\frac{\partial}{\partial t}(\rho_m Cp_m T) = -\rho_w Cp_w \nabla \cdot (vT) + \nabla \cdot \left(k_{m_{i,j}} \nabla T\right) + q_m \tag{0.24}$$

where $\rho_m$ is the density of the mixture, $Cp_m$ is the specific heat capacity of the mixture, $v$ is the velocity of the pore space water, $k_{m_{i,j}}$ is a symmetric tensor of the thermal conductivity of the mixture, and $q_m$ is the source of energy.

### 3.1.2 Radiative Heat Transfer

Any surface whose temperature is above absolute zero Kelvin emits electromagnetic radiation in the form of thermal energy. For a black body, the peak of this spectral thermal energy is described by Planck's law [104]. The total hemispherical grey body radiative energy emitted by a surface is calculated as

$$E = \varepsilon\sigma T^4 \tag{0.25}$$

The net heat flux of a surface *i* may be expressed as

$$q_i = -E_i + \sum_{j=1}^{n} \rho_i A_j F_{ji} q_j + q_{ext} \tag{0.26}$$

where $q_j$ is the total radiative energy of visible external surfaces emitting into the surface *i*. Since all the surfaces are assumed to be diffuse emitting and absorbing radiation, the view factor, $F_{i,j}$, can be defined as the ratio of radiation leaving surface *j* and received by surface *i* and is expressed as [105]

$$F_{j,i} = \frac{1}{A_j} \int_{A_j} \int_{A_i} \frac{\cos\theta_j \cos\theta_i}{\pi R^2} dA_i dA_j \tag{0.27}$$

As defined by the reciprocity theorem for radiative transfer [105], the view factors between the two surfaces are related as $A_j F_{j,i} = A_i F_{i,j}$.

### 3.2 Material Mixing Functions

Because a heterogeneous porous media is simulated, the effect of that heterogeneity on the thermal properties must be considered. At any point during the simulation, an element can be composed of a mixture of solid, water, and air. Specifically, mixing functions for the material properties of thermal conductivity and specific heat capacity are provided. For the thermal conductivity, the simple quasi-empirical mixing model of Lu et al. described in the previous chapter is used as

$$k_S = \left(k_{S_{sat}} - k_{S_{dry}}\right) K_e + k_{S_{dry}} \tag{0.28}$$

where $k_s$ is the soil thermal conductivity, $k_{S_{sat}}$ and $k_{S_{dry}}$ are the saturated and dry thermal conductivities of the soil, and $K_e$ is the Kersten number. For the SRSS, the Kersten number as derived by Johansen [99] is

$$K_e = 0.7\log\left(S(\psi)\right) \quad S(\psi) > 0.05 \tag{0.29}$$

for coarse grained soils and

$$K_e = \log\left(S(\psi)\right) \quad S(\psi) > 0.10 \tag{0.30}$$

for fine grained soils. The saturated and dry soil thermal conductivities may be determined from either laboratory measurements or approximated. Examples of these approximations have been shown previously in Chapter 2.

The specific heat capacity is calculated as a mass-weighted average and defined as

$$Cp_m = \frac{S(\psi)\varphi\rho_w Cp_w + \left(1-S(\psi)\right)\varphi_a\rho_a Cp_a + \left(1-\varphi\right)\rho_s Cp_s}{S(\psi)\varphi\rho_w + \left(1-S(\psi)\right)\varphi\rho_a + \left(1-\varphi\right)\rho_s} \tag{0.31}$$

where $Cp_m$ is the specific heat capacity of the mixture (subscripts *w,a,s* indicate water, air, solid, respectively), $\varphi$ is the porosity, and $\rho$ is the density. Studies by Howington et al. [106] indicate reasonable results compared to specific heat capacity measurements from field measurements of soils.

## 3.3 Numerical Methods

In this section, the numerical methods to solve the governing equations for fluid and heat flow and for radiative transfer are described. The fluid and heat flow equations are solved iteratively by Newton's method and the bi-conjugate gradient method [107]. The radiative heat transfer equations are solved by a Monte Carlo method [108-109].

### 3.3.1 Fluid Flow and Conductive Heat Transfer Numerical Method

Richards' equation and the heat flow equation are solved using a Newton-Krylov method. Both sets of equations form a system of nonlinear equations that are solved with a standard Newton's method. Given the nonlinear equation

$$F(X) = 0 \tag{0.32}$$

an approximation to $X$ is made ( $X_0$ ) and an improved approximation (Newton iteration) is calculated as

$$X_1 = X_0 - F'(X_0)^{-1} F(X_0). \tag{0.33}$$

This approximation continues iteratively until the difference between each successive approximation reaches some predefined small tolerance. During each of these iterations rather than direct calculation of the inverse Jacobian matrix in Equation (3.13) at each nonlinear iteration, an approximation of this matrix is calculated as a linear equation where

$$F'(X_i)(X_{i+1} - X_i) = -F(X_i) \tag{0.34}$$

and is solved with the Krylov method BiCGSTAB [107] with a point Jacobi preconditioner. Additional details and implementation of these numerical methods have previously been described [110-111].

### 3.3.2 Thermal Radiation Heat Transfer Numerical Method

In the simulation of a forest environment, the surface geometry of the soil, trunk, and foliage will be complex. To calculate the radiative transfer between these surfaces, view factors must be calculated from each surface to all the other surfaces [105]. For simulations where the surfaces can number in the millions, direct calculation of the view factors (Equation 3.8) may not be practical. Additionally, for complex surface geometries, there is no exact analytical solution to the radiative transfer equation [108]. Fortunately, the Monte Carlo technique can be applied to simulate the radiative heat transfer equation and provide an approximation to the exact solution.

The basis for using the Monte Carlo method [112] is illustrated with the calculation of an integral

$$I = \int_D g(x)dx \tag{0.35}$$

where $D$ is a region in $n$-dimensional space, and $g(x)$ is any continuous arbitrary function. The solution for the integral may be approximated if a set of independent randomly distributed samples $\left(x_1, \cdots, x_m\right)$ are selected from $D$ and applied as

$$\tilde{I}_m = \frac{1}{m}\left\{g\left(x_1\right) + \cdots + g\left(x_m\right)\right\} D \tag{0.36}$$

and $\tilde{I}_m$ becomes an approximation to the exact solution $I$. Applying the law of large numbers [113], as the number of $m$ samples is greatly increased, the approximation will approach the exact answer as

$$\lim_{m\to\infty} \tilde{I}_m \to I\,. \tag{0.37}$$

Following this approximation method, the Monte Carlo technique is applied to Equation 3.7. The total grey body flux from each surface is calculated, discretized into a large number of energy packets, and the packets are randomly emitted from the surface into the domain. The discretized energy packets are either absorbed or reflected until they are absorbed or exit the computational domain. Details of the Monte Carlo method applied to radiative transfer are described elsewhere [108, 114, 109], and implementation details for the SRSS are provided in Chapter 4.

# CHAPTER IV

# VERIFICATION OF THE SRSS COMPONENTS

The interaction between the processes (radiation, fluid flow, thermal conduction, and thermal convection) in the SRSS system is complex. Due to the unsteady nature of the problem, it is problematic to determine if the processes are performing as expected. Verification of the individual simulation components of the SRSS is a simpler task and can provide confidence that the complete simulation is working correctly. "Verification" in this research is used as defined by the U.S. Department of Defense, Instruction Number 5000.61 for DoD Modeling and Simulation Verification, Validation, and Accreditation, which states that verification is "the process of determining that a model or simulation implementation and its associated data accurately represents the developer's conceptual description and specifications." The verification as provided in this research is accomplished by comparison of results with analytical solutions and for a few cases, empirical approximations to a solution.

In this chapter, the following SRSS components examined:

- Longwave thermal infrared radiative heat transfer;
- Longwave downwelling sky radiative heat transfer;
- Shortwave thermal infrared direct illumination;
- Heat conduction through porous unsaturated media;
- Convective heat transfer in porous media.

## 4.1 Longwave Thermal Infrared Heat Transfer Verification

Consider a closed regular equilateral tetrahedron with edge lengths of $2\sqrt{2}$ m and whose vertices lie on a unit circumsphere centered at the origin. Assume that all four surfaces of the tetrahedron are thermally spectrally gray, diffuse, and emit, reflect, and absorb so that $\varepsilon = \alpha = 1 - \rho$. Let the temperature of the first wall be $T_1 = 1000\,\mathrm{K}$ with $\varepsilon_1 = 0.9$, the remaining walls at $T_2 = T_3 = T_4 = 600\,\mathrm{K}$ with $\varepsilon_2 = \varepsilon_3 = \varepsilon_4 = 0.4$. Due to the symmetry of this tetrahedron, all surface areas are equal (0.866 $m^2$), and the view factor ($F_{i,j}$) between any two different surfaces is 1/3.

For comparison of results, the net radiative flux is computed for each surface of the enclosure using an analytical method and the Monte Carlo simulation. For an analytical solution, the radiosity equation described by Modest [104] is applied. For an enclosed surface with no external radiation sources and known surface temperatures, the radiosity equation for the radiation interchange between surfaces may be represented as

$$-\frac{q_i}{\varepsilon_i} + \sum_{j=1}^{N}\left(\frac{1}{\varepsilon_j} - 1\right) F_{i,j} q_j = -E_{bi} + \sum_{j=1}^{N} F_{i,j} E_{bj} \tag{0.0}$$

where $E_{bi}$ and $E_{bj}$ are the black body radiative flux emitted from surfaces *i* and *j*, respectively. Applying Equation (4.1) for *i* =1 to *N* surfaces yields the solution for the net radiative exchange for each surface

$$\begin{bmatrix} q_1 \\ q_2 \\ q_3 \\ q_4 \end{bmatrix} = \begin{bmatrix} \text{-26,530.02} \\ \text{8,843.34} \\ \text{8,843.34} \\ \text{8,843.34} \end{bmatrix}. \tag{0.39}$$

Now consider the results if the enclosure is treated as if all surfaces are perfect blackbodies ($\varepsilon_1 = \varepsilon_2 = \varepsilon_3 = \varepsilon_4 = 1.0$) and repeating the processes (Equation (4.1)), the result is

$$\begin{bmatrix} q_1 \\ q_2 \\ q_3 \\ q_4 \end{bmatrix} = \begin{bmatrix} \text{-42,742.81} \\ \text{14,247.60} \\ \text{14,247.60} \\ \text{14,247.60} \end{bmatrix}. \tag{0.40}$$

Next the net radiative exchange is computed for each surface using the Monte-Carlo method [108, 115] as developed and implemented in the SRSS. The Monte Carlo technique for simulating radiative heat transfer in the enclosure consists of tracking discrete energy packets emitted from each of the surfaces and reflected until they are absorbed. The total radiative flux from all surfaces is derived by summing the fluxes from each *i*th surface. The energy associated with each discrete energy packet is calculated by dividing the total radiative flux by number of energy packets ( $N_e$ ) to be simulated.

$$e = \frac{\sum_i E_{bi}}{N_e} \tag{0.41}$$

The number of packets ( $n_i$ ) emitted from each surface is calculated by dividing the total energy of each surface *i* by the amount of energy in the energy packet,

$$n_i = \frac{E_{bi}}{e} \tag{0.42}$$

which will maintain consistent energy conservation. For example, a large surface with significant radiative flux will have more energy packets emitted from it compared to a small surface with lesser radiative flux.

In the implementation of the method in the SRSS, $N_e$ is represented as an integer, and because of round-off errors, it is frequently the case that

$$N_e e \neq \sum_i E_{bi} \tag{0.43}$$

For large values of $N_e$ (>10M) simulated with domains of a few surfaces, this is a small (1.0e-06%) error. But in order to maintain total radiative energy balance, $e$ is recalculated as

$$e = \frac{\sum_i E_{bi}}{\sum_i n_i} \tag{0.44}$$

and then $N_e$ recalculated again as

$$N_e = \sum_i n_i \tag{0.45}$$

During the SRSS simulation, an energy packet is emitted from a surface $i$ at a random zenith (0-90 deg) and azimuth angle (0-180 deg) from the surface normal $n_i$ different times. That packet is traced through the enclosure until it intersects another surface. At that time another random number is compared to the absorption of that surface. If the random number is greater, the energy packet is re-emitted from the center of the surface back into the enclosure. If the random number is less than the absorption of the surface, the packet is absorbed, and the number of packets absorbed by the surface, $n_i^*$, is incremented. Once the simulation of packet emission and bouncing is complete, the net radiative exchange of the surface ($q_i$) is given by

$$q_i = e\left(n_i - n_i^*\right) \tag{0.46}$$

Results from the Monte-Carlo technique applied to the closed regular equilateral tetrahedron are summarized in Table 4.1. For a large number of packets (~20M) and with the total emitted gray body radiance, $e$ is small (2.592e-03). Compared to the results from the radiosity method (Equation (4.2)), the Monte-Carlo results differ uniformly by less than 0.001 percent.

Applying this method for the black-body case (Equation (4.3)), again assigning $\varepsilon_1 = \varepsilon_2 = \varepsilon_3 = \varepsilon_4 = 1.0$ and keeping the surface temperatures the same, the Monte-Carlo results differ from the radiosity method by less than 0.001 percent (Table 4.2).

As stated previously, the number of total energy packets in the simulation affects the variability of the result. But as the number of packets increase then variance becomes smaller, and the result approaches the correct answer. In Figure 4.1 this effect is illustrated as the net radiative exchange was calculated for surface 1 of the tetrahedron and $N_e$ increased. As $N_e$ is increased, the variability in net radiative exchange decreases and converges to the exact solution.

Table 4.1 Monte-Carlo results for simple enclosed tetrahedron ($e$=2.592e-03) with $\varepsilon_1 = 0.9$, $\varepsilon_2 = \varepsilon_3 = \varepsilon_4 = 0.4$ and $N_e = 19,999,998$

| Surface Number | Temperature (K) | Rays Emitted | | Rays Received | | Net Radiative Exchange |
|---|---|---|---|---|---|---|
| 1 | 1000 | 17,053,204 | 85.27% | 6,815,062 | 34.07% | -26,530.12 |
| 2 | 600 | 982,264 | 04.91% | 4,395,802 | 21.98% | 8,843.79 |
| 3 | 600 | 982,264 | 04.91% | 4,399,293 | 22.00% | 8,844.61 |
| 4 | 600 | 982,264 | 04.91% | 4,389,839 | 21.95% | 8,841.72 |

Table 4.2 Monte-Carlo results for simple enclosed tetrahedron ($e$=3.410e-03) with $\varepsilon_1 = \varepsilon_2 = \varepsilon_3 = \varepsilon_4 = 1.0$ and $N_e = 19,999,997$

| Surface Number | Temperature (K) | Rays Emitted | | Rays Received | | Net Radiative Exchange |
|---|---|---|---|---|---|---|
| 1 | 1000 | 14,400,920 | 72.00% | 1,866,893 | 09.34% | -42,741.00 |
| 2 | 600 | 1,866,359 | 09.33% | 6,045,676 | 30.23% | 14,251.46 |
| 3 | 600 | 1,866,359 | 09.33% | 6,046,272 | 30.21% | 14,253.49 |
| 4 | 600 | 1,866,359 | 09.33% | 6,041,156 | 30.22% | 14,236.04 |

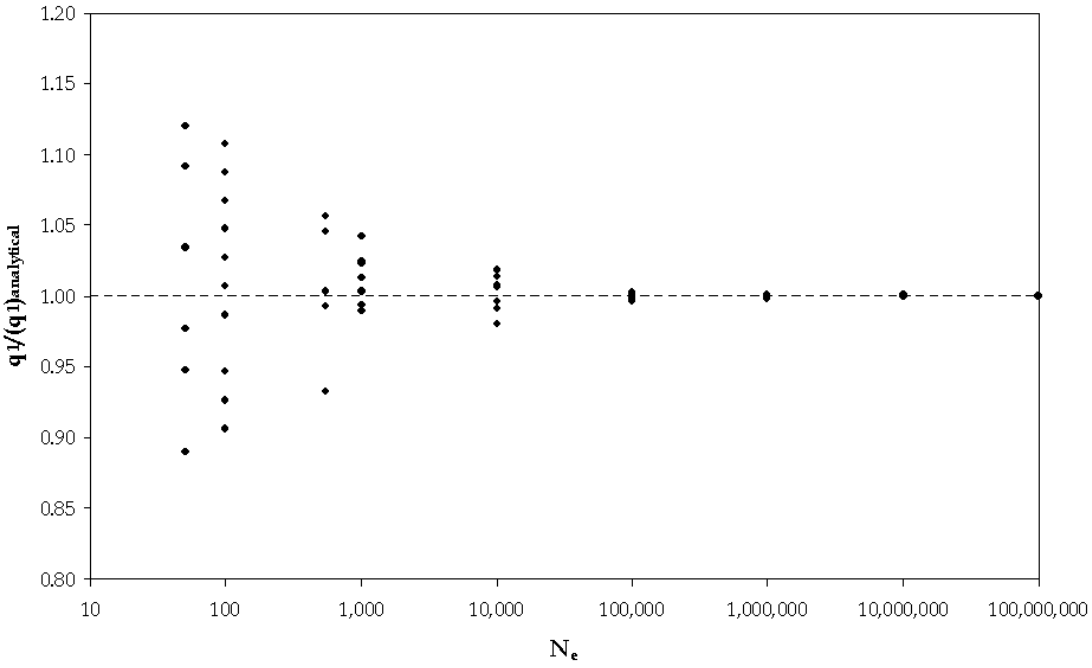


Figure 4.1 Illustration of the variability in the net radiative exchange for surface 1 of the unit tetrahedron as $N_e$ increases

## 4.2 Downwelling Longwave Sky Radiance Verification

Consider a meshed planar surface with edge lengths of 1 m (Figure 4.2) oriented with the surface normal aligned to the vertical axis. Assume that all surfaces of this plane are spectrally gray, emit, reflect, and absorb so that $\varepsilon = \alpha = 1 - \rho$. Let the integrated hemispherical downwelling longwave radiance of the sky to the surface be 500 W/m$^2$ , and the surface temperature of the surfaces be uniform at $T_n = 330$ K and with $\varepsilon_n = 0.9$.

For this trivial example, the net radiative flux of the surface can be calculated as the difference between the outgoing and inbound longwave radiance. The grey body (outgoing) emissive flux ( $L\uparrow$ ) of the surface is defined as

$$\varepsilon\sigma T_n^4 = (0.9)\,\sigma\left(330^4\right) = 605.218 \text{ W/m}^2, \tag{0.47}$$

and the inbound flux ( $L\downarrow$ ) is the integrated flux from the sky (500 W/m$^2$). Thus the net radiative flux of the surface, $L^* = \left(L\downarrow - L\uparrow\right)$, is (.9)(500) - 605.218 = -155.218 W/m$^2$.

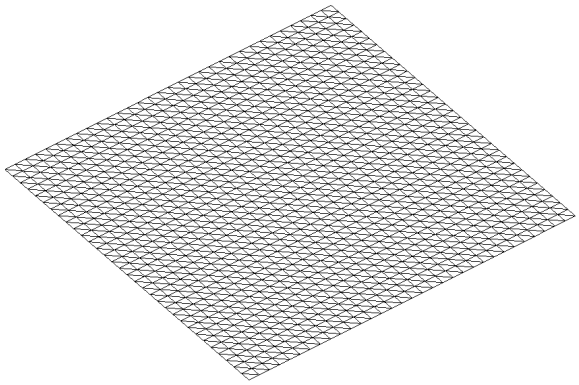

Figure 4.2 Example meshed unit surface

For an additional verification, the same meshed surface was used and alternatively decreased or increased to develop a corrugated mesh surface (Figure 4.3) containing 2048 triangular elements. The corrugation angle for the mesh is 136.4 degrees and calculating the view factors [104] in two dimensions for two infinite surfaces, the view factor for one side surface to the sky is 93%. Assuming the properties of the previous flat meshed surface and applying view factors for the wedge-like grooves, the net radiative flux of a simple non-meshed surface is -114.1 $W/m^2$. This result is approximately 93% of the net radiative flux of the flat surface which corresponds to the view factor of the surfaces to the sky.

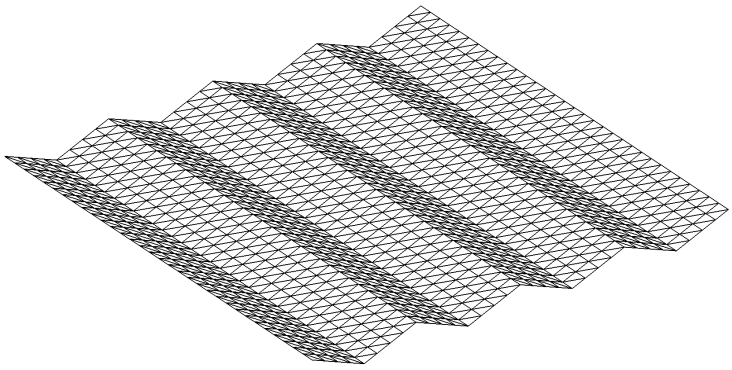

Figure 4.3 Corrugated mesh used in verification of the longwave sky radiation

### 4.2.1 Backward Monte Carlo Simulation for the Sky Longwave Radiance

The simulation of the downwelling longwave sky radiance is calculated in the SRSS using a backward (or reverse) Monte Carlo method [104, 109] . The backward Monte Carlo method is the preferred method used in a situation where the receiving surface facets are relatively small in comparison to the emitting facets. In the forward method, the number of emitted energy bundles required for some statistically significant results would be several orders of magnitude greater, computationally inefficient, than compared to the amount required for this backward method [109].

In the backward implementation, a triangulated hemisphere representing the distribution of downwelling longwave radiation from the sky is used for the sky simulation (Figure 4.4). This hemisphere is normalized, centered on each facet of the ground surface, and each of the hemisphere facets is labeled with the appropriate radiative flux from the sky. During simulation, photons are emitted from the center of the mesh element through the center of each sky facet. If the photon (energy bundle) exits the domain without intersecting another ground mesh element, then the mesh element accumulates the energy assigned to the sky facet. Otherwise if the photon intersects another mesh element, then no energy is added from the sky. Energy added to the mesh element is divided into two parts, absorbed and reflected energy. After each of the mesh elements have calculated total sky radiance, and then the reflected energy is radiated throughout the domain using the standard (forward) Monte Carlo method.

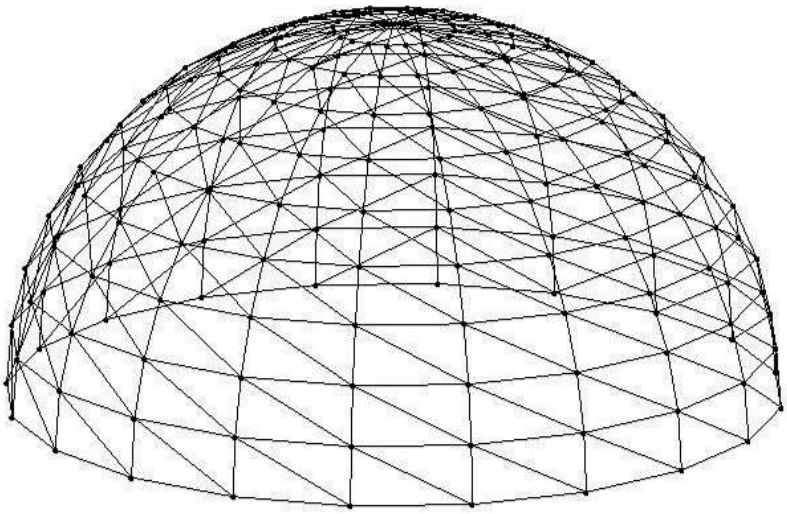

Figure 4.4 Example triangulated hemisphere used for the distribution of the longwave sky radiation

### 4.2.2 Backward Monte Carlo Results

To verify the results for the backward Monte Carlo technique in the SRSS, the simulation was conducted on the 1 $m^2$ flat surface (Figure 4.2). The surface is equally divided into 2,048 triangular mesh elements so that each mesh element area is $4.8828 \times 10^{-4}$ $m^2$. The triangulated sky hemisphere composed of 70 triangular mesh elements (Figure 4.4) was assigned so that the integrated radiance of the hemisphere equaled 500 W/$m^2$. Using the backward Monte Carlo method with a total of 2 million energy packets, each of the mesh elements emitted energy bundles backward up into the hemisphere and gathered the energy received if they were not intercepted. The resulting radiation of the sky onto the surface was 450 W/$m^2$. The radiation exiting the surface was calculated using the forward Monte Carlo method for a net radiation flux ($L\uparrow$) of 605.218 W/$m^2$. Thus the total net longwave flux for the flat surface was -155.219 W/$m^2$.

The same method was conducted on the corrugated mesh surface, where the projected length of the sides is 1 m and the surface divided into 2,048 triangular faces

(Figure 4.3). Using the backward Monte Carlo method, the average downwelling longwave radiation intercepted was 384.0 $W/m^2$, and the average net emittance was 605.3 $W/m^2$. Thus the average total net longwave flux for the corrugated surface was -165.0 $W/m^2$. Images for both the flat and corrugated simulation results are provided in Figure 4.5 and Figure 4.6.

Next, the triangulated sky hemisphere was successively refined to examine the effect of mesh refinement on the total net longwave flux. Using a simple refinement method, the triangulated sky hemisphere was refined from 70 elements to 280, 1120, and 4480 mesh elements. Each of these meshes was used with the backward Monte Carlo technique using the same parameters described previously. The results of the mesh refinement on the net longwave radiation for the corrugated surface are provided in Table 4.3 and in Figure 4.7. As the sky hemisphere is successively refined, the net longwave surface flux asymptotically approaches -172.3 $W/m^2$. These results suggest that the coarser resolution hemisphere can underestimate the magnitude of the total surface flux. Similarly, the corrugated surface was successively refined to examine the effect of surface mesh refinement on the total net longwave flux. Using a simple refinement method, the surface was progressively refined from 320 elements to 81,920 mesh elements. A triangulated sky hemisphere containing 1120 mesh elements was used with the backward Monte Carlo radiative transfer technique and the results are provided in Table 4.4

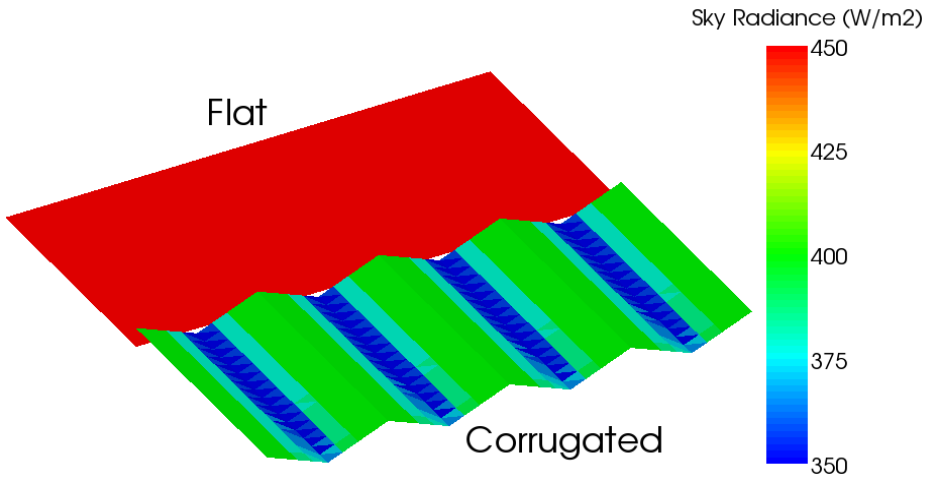


Figure 4.5 Sky radiance simulation results on both the flat and corrugated surfaces

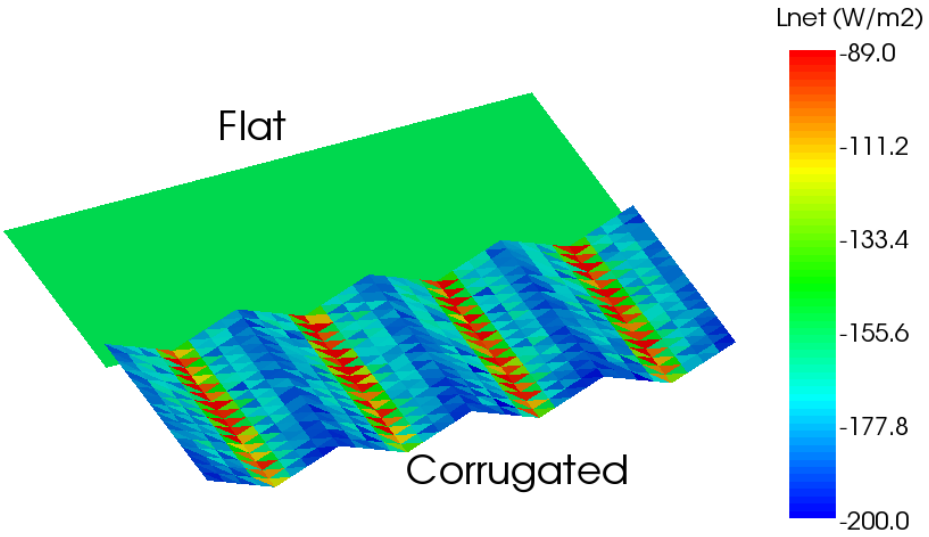


Figure 4.6 Simulation results for net longwave radiation for the flat and corrugated surfaces. Net longwave flux for the flat and corrugated surfaces are -155.2 $W/m^2$ and -165.0 $W/m^2$, respectively

Table 4.3 Triangulated sky hemisphere mesh refinement results

| **Hemisphere Mesh Elements** | **Sky Inbound Flux ($W/m^2$)** | **Surface Emissive Flux ($W/m^2$)** | **Total Surface Net Longwave Flux ($W/m^{2)}$** |
|---|---|---|---|
| 70 | 384.0 | -605.3 | -165.0 |
| 280 | 380.2 | -605.3 | -168.8 |
| 1120 | 377.3 | -605.3 | -171.7 |
| 4480 | 376.6 | -605.3 | -172.3 |

Table 4.4 Corrugated surface mesh refinement results for the 1120 element sky hemisphere mesh

| **Surface Mesh Elements** | **Sky Inbound Flux ($W/m^2$)** | **Surface Net Flux ($W/m^2$)** | **Total Surface Net Longwave Flux ($W/m^{2)}$** |
|---|---|---|---|
| 320 | 377.18 | -546.79 | -169.61 |
| 5120 | 375.11 | -544.98 | -169.87 |
| 20480 | 375.57 | -544.84 | -169.27 |
| 81920 | 375.59 | -544.65 | -169.06 |

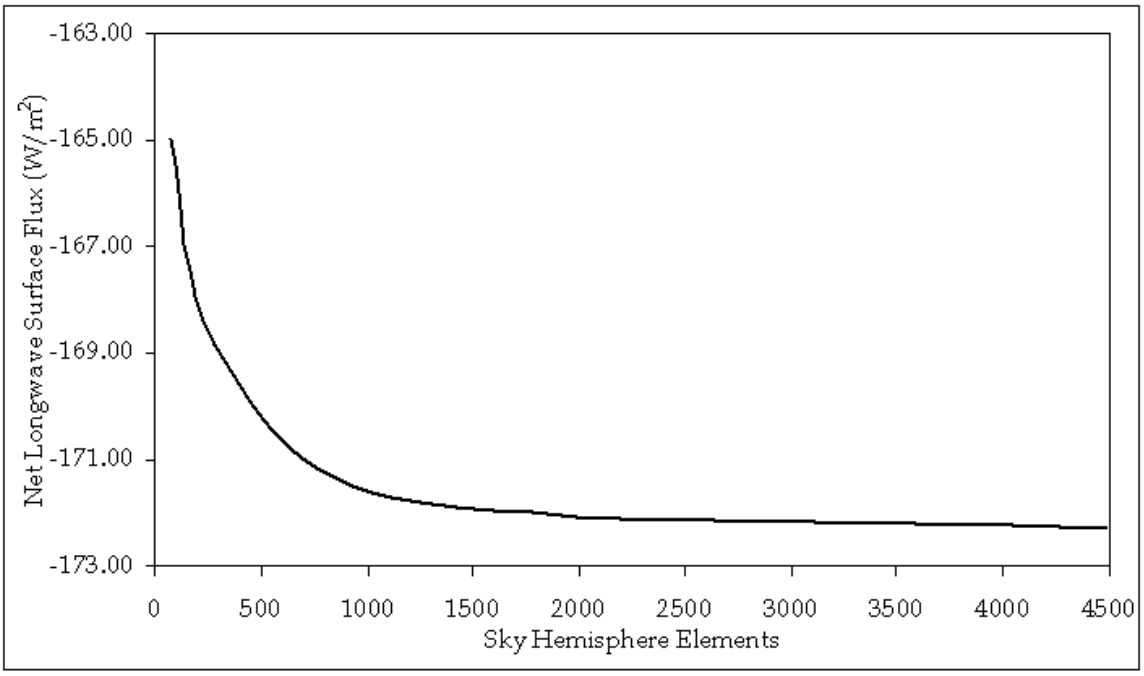


Figure 4.7 Effect of mesh refinement of the sky hemisphere on the net longwave radiation for the corrugated surface

## 4.3 Shortwave Thermal Infrared Radiance Verification

Consider a meshed unit spherical surface with a radius of 0.5 m (Figure 4.8) arranged so that the normal of the faces are oriented outward. Assume that all mesh elements of this sphere are spectrally gray in the shortwave (0.3 - 3.0 μm) spectral region with an average shortwave reflectance of 30%. Let the direct shortwave solar radiation to

the surface be $E_{sw} = 1000\,\mathrm{W/m^2}$ and the diffuse (scattered) shortwave radiation be 50.0 $\mathrm{W/m^2}$. The direct shortwave solar illumination geometry is set to a solar azimuth of 120.0 degrees measured clockwise from north and zenith of 61.0 degrees measured from vertical.

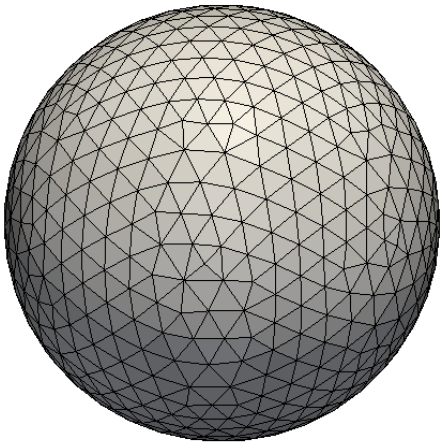

Figure 4.8 Example meshed unit sphere

To verify the simulation of the shortwave radiation in the SRSS, the distribution of energy is calculated over the surface. The distribution of radiant incident energy on the spherical surface will vary according to Lambert's cosine law [47, 116]: the amount of incident energy on the surface is directly proportional to the cosine of the angle between the surface normal and the illumination vector. A continuous perfect sphere illuminated with the given parameters will contain a uniform distribution of incidence angles from 0 to 90 degrees. For the example of a meshed sphere, a similar discrete set of angles will also exist. Thus, the expected range of incident direct shortwave radiation will be spherically distributed from 0 to $(1-\rho)E_{sw}$. In this example the maximum range will be $(1-\rho)E_{sw} = 700\,\mathrm{W/m^2}$.

### 4.3.1 Direct Shortwave Radiation Simulation Method

To simulate the direct shortwave radiation on to the surface of the sphere, the backward Monte-Carlo method is applied. As described previously in section Figure 4.3, the method emits a ray from the center of a mesh element in the direction of the illumination source. If the ray intersects any neighboring mesh element, then that face is obscured from direct radiation by the neighbor mesh element and receives only the diffuse shortwave radiation. Otherwise if the mesh element does not intersect any other face, the radiation received on the mesh element is calculated as

$$q_{sw} = (1-\rho) E_{sw} \cos\theta \tag{0.48}$$

The angle $\theta$ is calculated as the angle between the mesh element normal and the illumination source vector.

### 4.3.2 Verification of the Direct Shortwave Radiation Simulation

To verify the results for the backward Monte-Carlo technique for the direct shortwave radiation, the simulation was conducted on the meshed sphere (Figure 4.8) composed of triangular faces each having a gray diffuse reflectance of 30%. The radius of the meshed sphere is 0.5 m. The surface of the sphere is divided into 1,314 mesh elements with an area average of 2.4e-03 $m^2$. Applying the described simulation method for direct shortwave resulted in a uniform distribution of incident radiation from 0 to 700 $W/m^2$ (Figure 4.9). These results correspond to the expected values in the analytical solution.

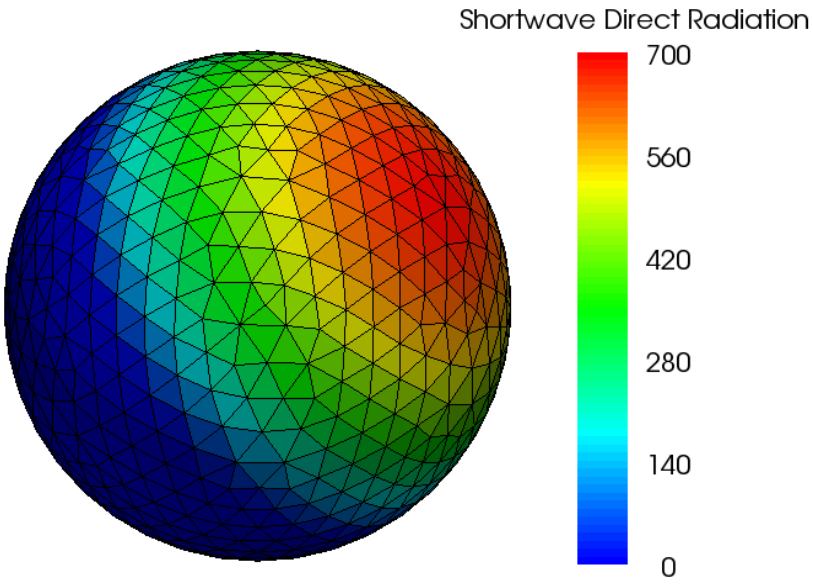


Figure 4.9 Results of simulation of the direct shortwave radiation on to the meshed unit sphere

## 4.4 Conductive Heat Transfer through Porous Media

Consider a plane wall consisting of porous media of thickness L, thermal diffusivity $\alpha$, and a uniform initial temperature $T_i$. Next consider that the wall is exposed suddenly on both surfaces to a fluid at temperature $T_\infty$. Assume that the dimensions of the wall in the y and z directions are large enough to consider this problem as a one-dimensional in the x-axis. Further assume that the properties of the wall are thermally invariant. The temperature history of the wall during the transient time period can then be found analytically and numerically, and the results compared.

The analytical solution is provided by Myers [117], and involves separation and normalization of variables. The governing partial differential equation for the wall is

$$\frac{1}{\alpha}\frac{\partial T}{\partial t} = \frac{\partial^2 T}{\partial x^2}. \tag{0.49}$$

This equation is normalized by defining

$$x^* = \frac{x}{L}, \quad t^* = \frac{\alpha t}{L^2}, \quad \text{and} \quad T^* = \frac{T - T_\infty}{T_i - T_\infty} \tag{0.50}$$

and using separation of variables, the analytical solution is obtained as a series solution as

$$u\left(x^*, t^*\right) = \frac{4}{\pi}\left(\sin \pi x^* e^{-\pi^2 t^*} + \frac{\sin 3\pi x^*}{3} e^{-9\pi^2 t^*} + \cdots\right). \tag{0.51}$$

The computational solution is addressed by constructing a wall made of 40,633 tetrahedral elements with a total thickness of 2.0 m. The wall has a porosity of 42.6 %, saturation of 53.0 %, dry thermal conductivity of 0.271 $\mathrm{W\,m^{-1}\,K^{-1}}$, quartz content of 58%, density of 1397.2 $\mathrm{kg\,m^{-3}}$, and specific heat capacity of 1040.7 $\mathrm{J\,kg^{-1}\,K^{-1}}$. The calculated bulk thermal conductivity at 53% saturation is 1.509 $\mathrm{W\,m^{-1}\,K^{-1}}$ and calculated thermal diffusivity is 1.038e-06 $\mathrm{m^2\ s^{-1}}$ using the soil thermal conductivy model described by Lu et al. [100]. The numerical results are provided in Figure 4.10 for the same non-dimensional time periods as the analytical solutions. The $L_2$-norm of the error between the numerical solution and the analytical solution at non-dimensional times of 0.05, 0.10, and 0.25 are 0.013, 0.013, and 0.006, respectively.

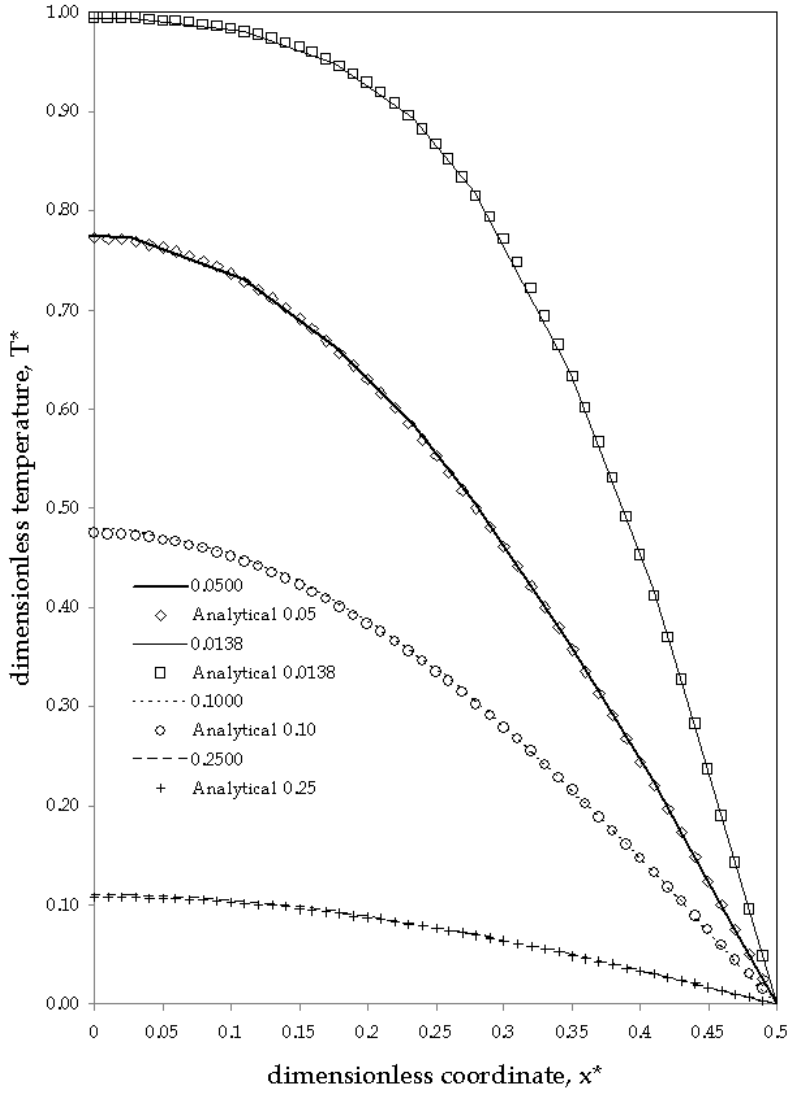


Figure 4.10 Plane-wall transient analytical and computational solution for non-dimensional times of 0.0138, 0.05, 0.10, and 0.25

## 4.5 Convective Heat Transfer in Porous Media

Consider a fluid of uniform temperature and laminar uniform slug flow velocity entering a cylinder filled with porous media. Assume that the surface of the cylinder is heated at a constant temperature that is greater than the entering fluid temperature ($T_w > T_\infty$) so that as the fluid passes through the cylinder, thermal convection occurs and a

thermal boundary layer develops (Figure 4.11). The boundary extent of the thermal boundary layer region is generally determined by the equation [118]

$$\frac{T_w - T_f}{T_w - T_\infty} = 0.99 \tag{0.52}$$

where $T_w$ is the cylinder wall temperature, $T_f$ is the fluid temperature, and $T_\infty$ is the far field fluid temperature. The length starting at the entrance of the cylinder to where the thermal boundary layer reaches the longitudinal axis of the cylinder is called the thermal entrance length. The thermal entrance length is a function of fluid velocity, diameter of the cylinder, porosity of the medium, Reynolds number, and Prandtl number and is approximated by [119]

$$\frac{x_{TEL}}{D} \approx 0.05 \mathrm{Re}_D \mathrm{Pr} \tag{0.53}$$

where $x_{TEL}$ is the thermal entrance length, and $D$ is the cylinder diameter.

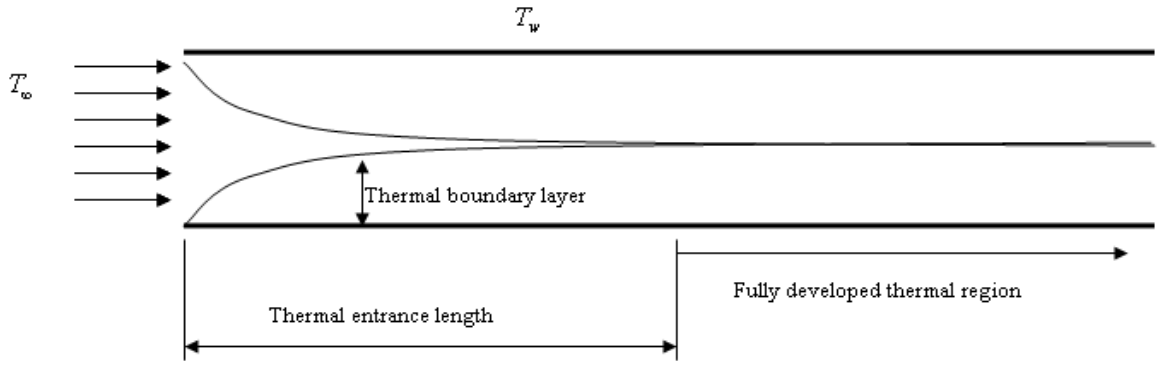


Figure 4.11 Diagram of the convective heat transfer example

This approximation is only valid when convection overwhelms conduction in the downstream wake ($u_\infty x / \alpha \gg 1$), which is also $\mathrm{Pe}_x \gg 1$. If this condition is not satisfied,

then the temperature field is dominated by the thermal conduction of the medium and not the convection of the fluid flow. Additionally for this example, the fluid velocity in the medium is a function of the pressure gradient of the fluid, hydraulic conductivity, and porosity of the media. Applying the material properties shown in Table 4.5, an approximation can be made for a thermal entry length for a given velocity (Table 4.6).

Table 4.5 Material properties for thermal convection simulation

| **Property** | **Fluid** | **Solid** |
|---|---|---|
| Density (kg $m^{-3}$) | 998.30 | 1550.00 |
| Thermal Conductivity (W $m^{-1}$ $K^{-1}$) | 0.605 | 0.271 |
| Dynamic Viscosity (kg $m^{-1}$ $s^{-1}$) | 9.77E-04 | - |
| Kinematic Viscosity ($m^2$ $s^{-1}$) | 9.79E-07 | - |
| Specific Heat (J $kg^{-1}$ $K^{-1}$) | 4183.00 | 800.00 |
| Hydraulic Conductivity (m $s^{-1}$) | 1.16E-04 | - |
| Thermal Diffusivity ($m^2$ $s^{-1}$) | 1.49E-07 | 2.19E-07 |

Table 4.6 Approximated thermal entry length for porous media in a heated cylinder with slug flow using Equation(4.16).

| **Velocity (m/s)** | **Thermal Entry Length (m)** |
|---|---|
| 0.0001 | 0.029 |
| 0.0002 | 0.058 |
| 0.0003 | 0.087 |
| 0.0004 | 0.116 |
| 0.0005 | 0.145 |
| 0.0006 | 0.174 |
| 0.0007 | 0.203 |
| 0.0008 | 0.232 |

The verify the convective heat transfer in the SRSS, a cylinder of 0.1-m diameter and 1-m length was constructed and meshed as an unstructured mesh with 477,289 tetrahedral elements. In this mesh, the elements had an average length of 0.005 m. The medium in the cylinder was assigned properties described in Table 4.5 and set to a

porosity of 45%. The far-field fluid temperature was set to 20 deg C, and the wall temperature of the cylinder was set to 30 deg C. The thermal boundary layer threshold was calculated from Equation (4.15) to be 20.1 deg C.

Simulations were conducted for a set range of fluid velocities ranging from 0.0001 m/s to 0.0008 m/s. The Reynolds numbers for these velocities indicated that the flow was laminar. Examples of these simulations are shown in Figure 4.12 as two-dimensional cross sections of the cylinder.

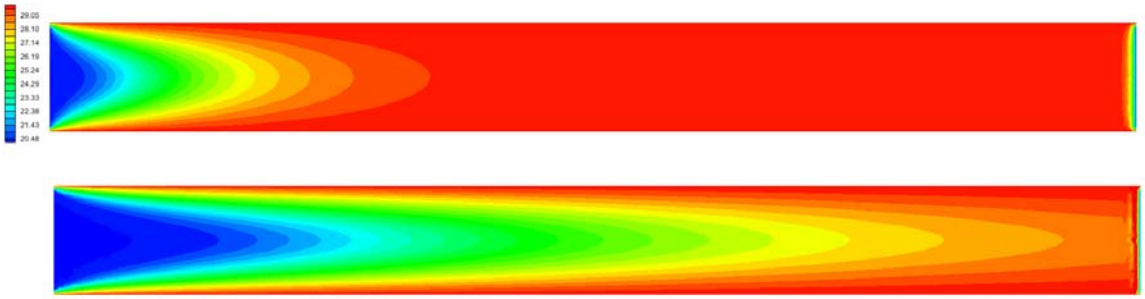

Figure 4.12 Thermal entry lengths for fluid velocities of 0.0001 (top) and 0.0008 m/s (bottom). Legend units are in degrees C

A summary of these simulations with the incremental fluid velocity changes is shown in Figure 4.13. The average error observed in the simulation is about 0.01 m, which could be attributed to several factors; the discretization of the domain, sensitivity of Equation (4.16) to diameter size, and averaging of temperature across elements at the narrowest part of the thermal entrance region. A higher resolution (3,091,204 tetrahedral elements), second computational domain was constructed by refining the elements of the previous domain to determine if the error was mesh related. Analysis of the results from the higher resolution mesh showed that the results were the same as the original resolution mesh.

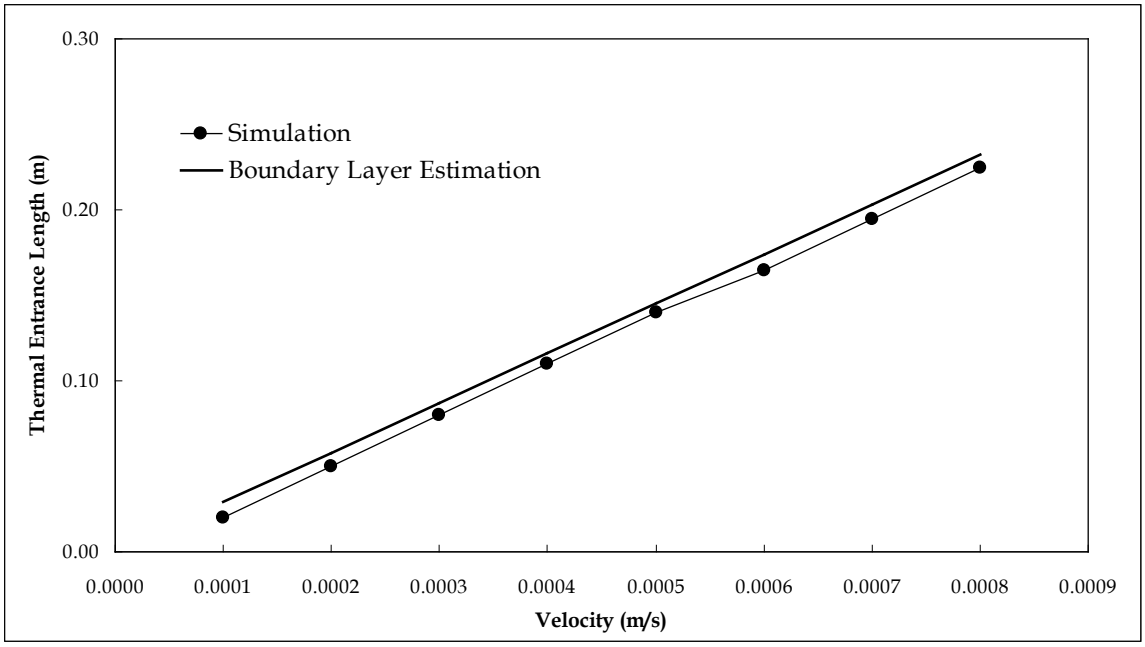


Figure 4.13 Simulated and Estimated Thermal Entry Lengths for Convective Heat Transfer in Porous Media

# CHAPTER V

# APPLICATIONS OF THE SRSS TO HISTORICAL SIMULATIONS

In the previous chapter, each of the components of the SRSS was verified against analytical solutions. In this chapter, the SRSS is applied and compared with historical simulations. In most of these historical simulations, the properties of the materials and fluxes involved are not characterized in detail, and subsequently the properties are approximated. As a consequence, the comparison of SRSS results will be qualitative rather than quantitative

Next the published studies and simulations conducted by Herrington [39, 54] and Derby and Gates [40] will be quantatively compared with the SRSS. In each of these two applications, the computational domain and material properties are described, and the assumptions and limitations explained.

## 5.1 Herrington (1964)

In 1964, Herrington conducted a study to investigate the role of tree stems in the thermal energy budget of a closed forest stand. Herrington's research addressed the coupling of tree surface temperatures to air temperature in dense canopy. In this study, a 48-year-old red pine (*Pinus resinosa*) in a mature pine plantation was selected for measurement and simulation. This selected tree in the dense canopy had a full crown, diameter at breast height of 30 cm, and average bark thickness of 1 cm.

There are a few assumptions that are considered in the Herrington study. First, because of the dense canopy, the direct shortwave radiation was blocked, and only the

diffuse or indirect shortwave radiation was considered to reach the trunk. Second, because of the diffuse shortwave radiation regime and the similar size neighboring trees, the tree would roughly be in thermal equilibrium with its environment, and subsequently the net longwave radiation balance would be zero. Finally, the last assumption is that because of the diffuse nature of the radiation, the internal temperatures would be similar in the radial direction, and the trunk could be approximated with a one-dimensional simulation. With these simplifying assumptions, Herrington developed a solution for the internal temperatures using the Fourier series relating the sinusoidal heating pattern of the surface to internal temperatures lagged by the thermal properties and diameter of the wood.

### 5.1.1 Computational and Material Properties Description for the Herrington Simulation

A computational domain was constructed (20-cm thick and 30-cm in diameter) to match the measurements and physical properties of the materials as described in Herrington's study. The average element size for this unstructured tetrahedral mesh was 0.5-cm. The mesh consisted of 140,064 elements and 26,721 nodes. The domain was divided into three distinct materials; bark, sapwood, and heartwood. The inner heartwood, sapwood, and bark radii measured from the center were 4.0, 14.0, and 15.0 cm respectively.

The properties for these materials used in the simulation are shown in Table 5.1. The shortwave reflectance and the longwave emissivity of the bark were not described in the Herrington study, so these properties were calculated from other sources of bark measurements [120]. None of the elements in the domain were designated as hydraulically active for this example. The Herrington study observed and simulated the

internal temperatures at 81.0 cm above the ground to avoid ground conduction effects and assumed that the fluid flow through the system was not sufficient to affect the internal temperatures. For this computational setup, the only boundary condition was the time-varying radiative flux at the bark surface.

Table 5.1 Material properties for the Herrington simulation

| **Material** | **Specific Heat (*J / kg K*)** | **Thermal Conductivity (*W/m K*)** | **Specific Gravity (%)** | **Shortwave Reflectance (%)** | **Longwave Emissivity (%)** |
|---|---|---|---|---|---|
| Bark | 1364 | 0.23 | 0.30 | 0.55 | 0.95 |
| Sapwood | 1420 | 0.35 | 0.46 | N/A | N/A |
| Heartwood | 1200 | 0.38 | 0.37 | N/A | N/A |

### 5.1.2 Results for the Herrington Simulation

The SRSS was applied to the conditions and geometry described for the Herrington simulation with no fluid flow conditions. The diffuse shortwave radiative energy varied diurnally and was applied uniformly on each surface element which was varied according to the reflectance of the material. Diurnal air temperature was obtained from the Herrington study, and the diffuse shortwave radiation and relative humidity were estimated as average clear sky conditions typically found in the northeastern United States [121]. Wind velocities were held constant at 1.0 m/s and barometric pressure at 1000 mb. The three-dimensional results from the SRSS are provided in Figure 5.1, and the one-dimensional comparison is shown in Figure 5.2.

### 5.1.3 Herrington Simulation Discussion

This simulation test shows that the SRSS can reproduce the qualitative temperature changes and characteristics that Herrington observed and simulated. The simulated and observed temperature changes within the tree match in timing and

magnitude throughout the diurnal cycle. This is not surprising given the number of assumptions and careful selection of the study site. By limiting the solar radiative effect to strictly the shortwave diffuse radiation, the simulation is simpler because of a lack of calculations of the spatially varying direct solar radiation. Similar studies have shown that these types of simulations are most sensitive to solar flux [68].

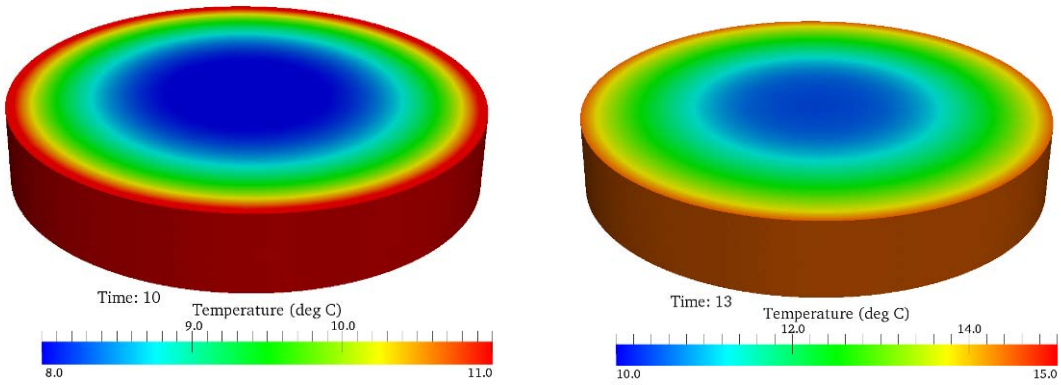


Figure 5.1 Red pine simulation results (1000 hrs and 1300 hrs) with material properties described by Herrington [54]

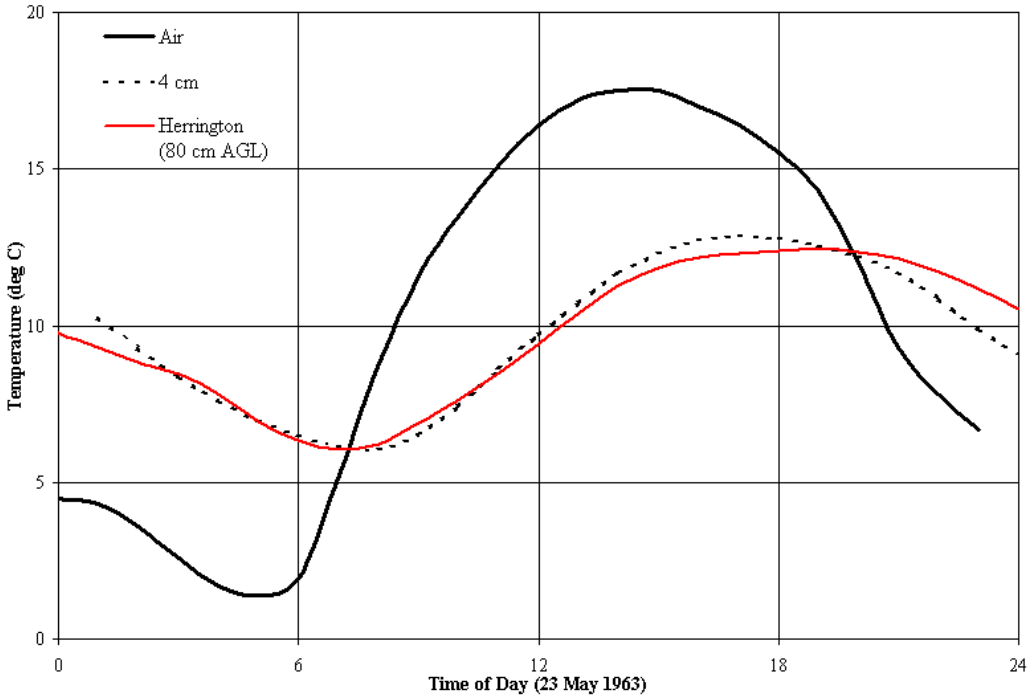


Figure 5.2 Herrington's stem temperature plots [54] and SRSS simulated stem temperatures

## 5.2 Derby and Gates (1965)

In 1965, Derby and Gates [40] provided two different sets of observed internal temperatures from different trees. One set of temperatures was observed from a 2.44-m pine log (*Pinus contorta*) 0.18 m in diameter placed vertically in a large open field in Boulder, CO, USA. The other set of temperatures was observed from a living aspen tree (*Populus* sp.) 0.15 m in diameter growing on an edge of a forest near Blackhawk, CO, USA (2 April 1964, latitude. 39.8 deg N, longitude. 105.5 deg W).

In their simulations, the tree trunk was represented as a two-dimensional cylinder perpendicular to the surface of the earth. The cylinder was divided into 12 radial sectors and five concentric rings giving the finite element domain a total of 60 trapezoidal elements (Figure 5.3). Each element center point represents an average value for

temperature, density, specific heat, and thermal conductivity. At each hourly time step in their simulation, a first-order forward difference in time and a central difference scheme in space were used to compute a solution. To control stability of the calculations, the time steps were kept equal to or smaller than 0.005 hr per step. Potter and Andresen [68] revisited the Derby and Gate simulation and used a second-order finite difference scheme with temporal derivatives using a centered leapfrog scheme. These simulation results were similar to the original simulation results.

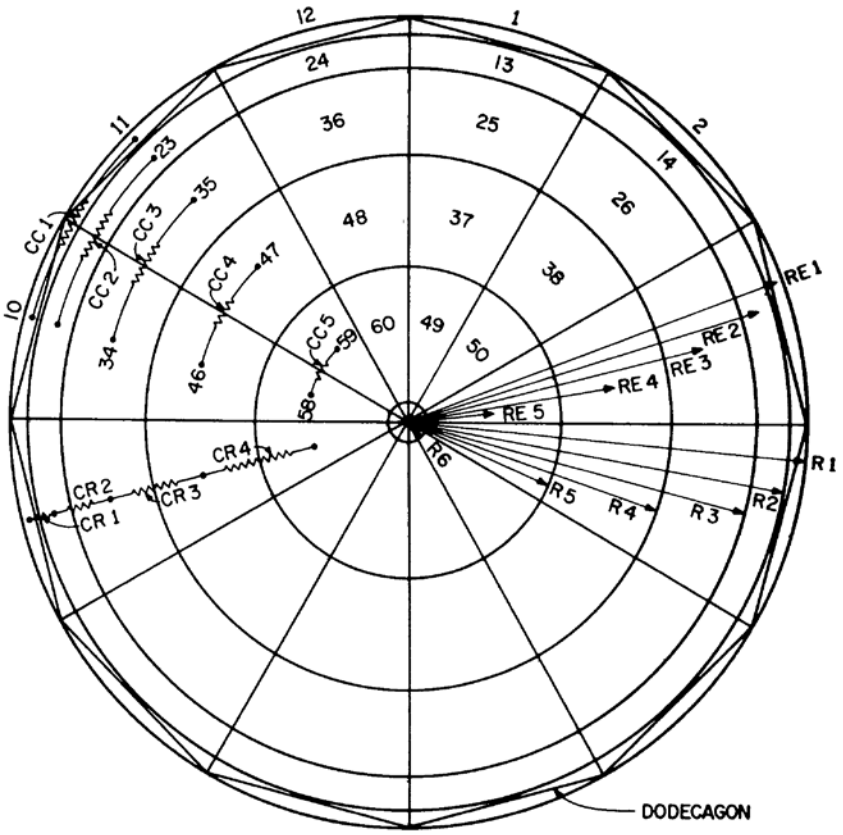


Figure 5.3 From Derby and Gates [40], finite element mapping for the aspen tree trunk

### 5.2.1 Computational and Material Properties Description for the Derby and Gates Simulation

A computational domain was constructed to match the size and dimensions of the described pine log. The log was 0.18 m in diameter, 0.3-m high, and contained 71,750 unstructured tetrahedral elements (see Figure 5.4). As described by Derby and Gates, the domain was divided into two distinct materials; bark and sapwood. The bark thickness was 0.01-m and sapwood radius was 0.16-m. The properties for these materials are shown in Table 5.2. The shortwave and longwave properties were not described in the study, so these properties were calculated from other sources of measurement. The placement of the log in the wide open field allows for the simulation of the shortwave and longwave contributions to be regarded from only the sky or the ground but not any other surrounding trees or foliage. Consequently for this simulation, complex radiative transfer calculations are not required. Air temperature history was provided in the original paper, but all other meteorological conditions were calculated for similar meteorological conditions encountered during October in Boulder, Colorado [122].

Table 5.2 Material properties for the Derby and Gates simulation

| **Material** | **Specific Heat (*J / kg K*)** | **Thermal Conductivity (*W/m K*)** | **Specific Gravity (%)** | **Shortwave Reflectance (%)** | **Longwave Emissivity (%)** |
|---|---|---|---|---|---|
| Pine Bark | 1364 | 0.23 | 0.30 | 0.27 | 0.95 |
| Pine Sapwood | 2470 | 0.46 | 0.686 | N/A | N/A |

### 5.2.2 Results for the Derby and Gates Simulation

The SRSS was applied to the conditions and geometry described for the Derby and Gates simulation with no fluid flow conditions and no radiative transfer. Results from the simulation along the north radius are provided in Figure 5.5. The simulated

temperatures show good agreement until after 1400 hrs, when the near surface simulated temperature (Sim 13) is cooler than the observed temperature (Obs 13 in Figure 5.5). In contrast the simulated center temperature (Sim 04) corresponds well with the observed temperature after 1700 hrs.

Figure 5.6 provides the cross-section simulated temperature history of the pine log from 0800 hrs to 1900 hrs. In this figure the temperature at 1 cm on the south radius of the log ranges from 4 deg C to 44 deg C. This simulated temperature range matches the observed temperature ranges at the same position. These ranges of temperatures are not unexpected, since the log was placed in an open field and received full direct illumination at a time of the year (October) when the solar incidence angle is greater for a vertical surface of the trunk than in the summer.

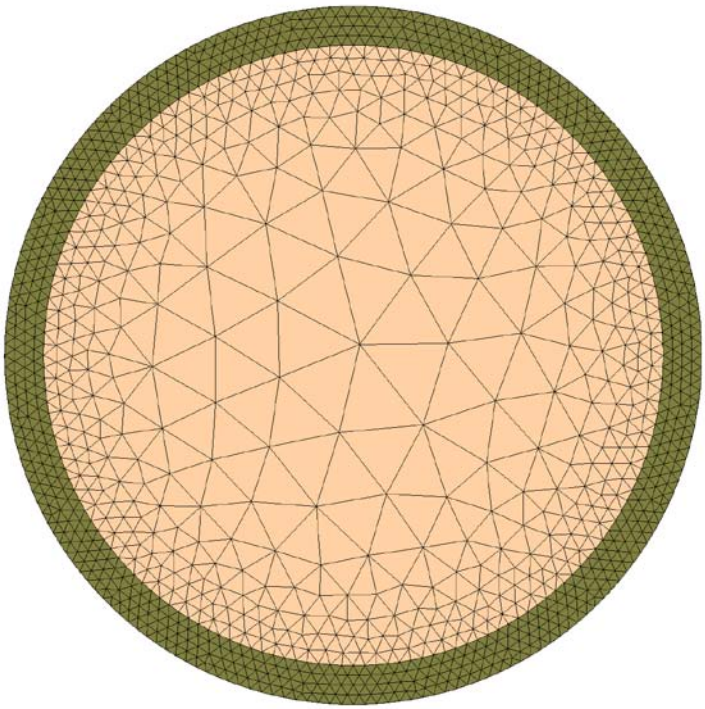

Figure 5.4 Computational domain used for the comparison of the observed temperatures from Derby and Gates

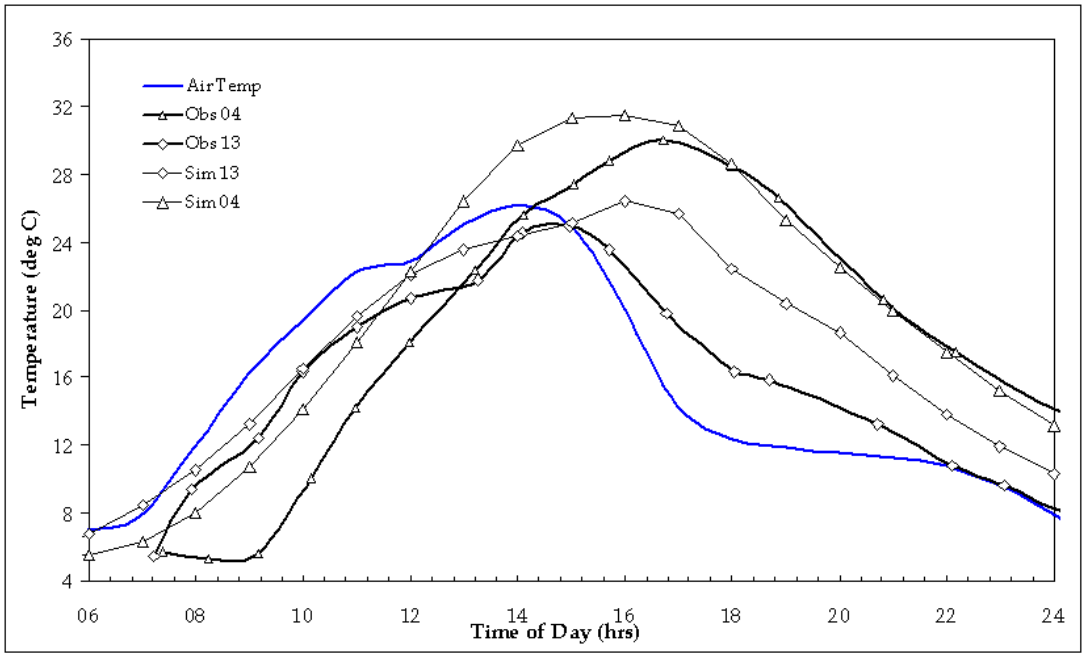


Figure 5.5 Measured and simulated temperatures for the Derby and Gates simulation

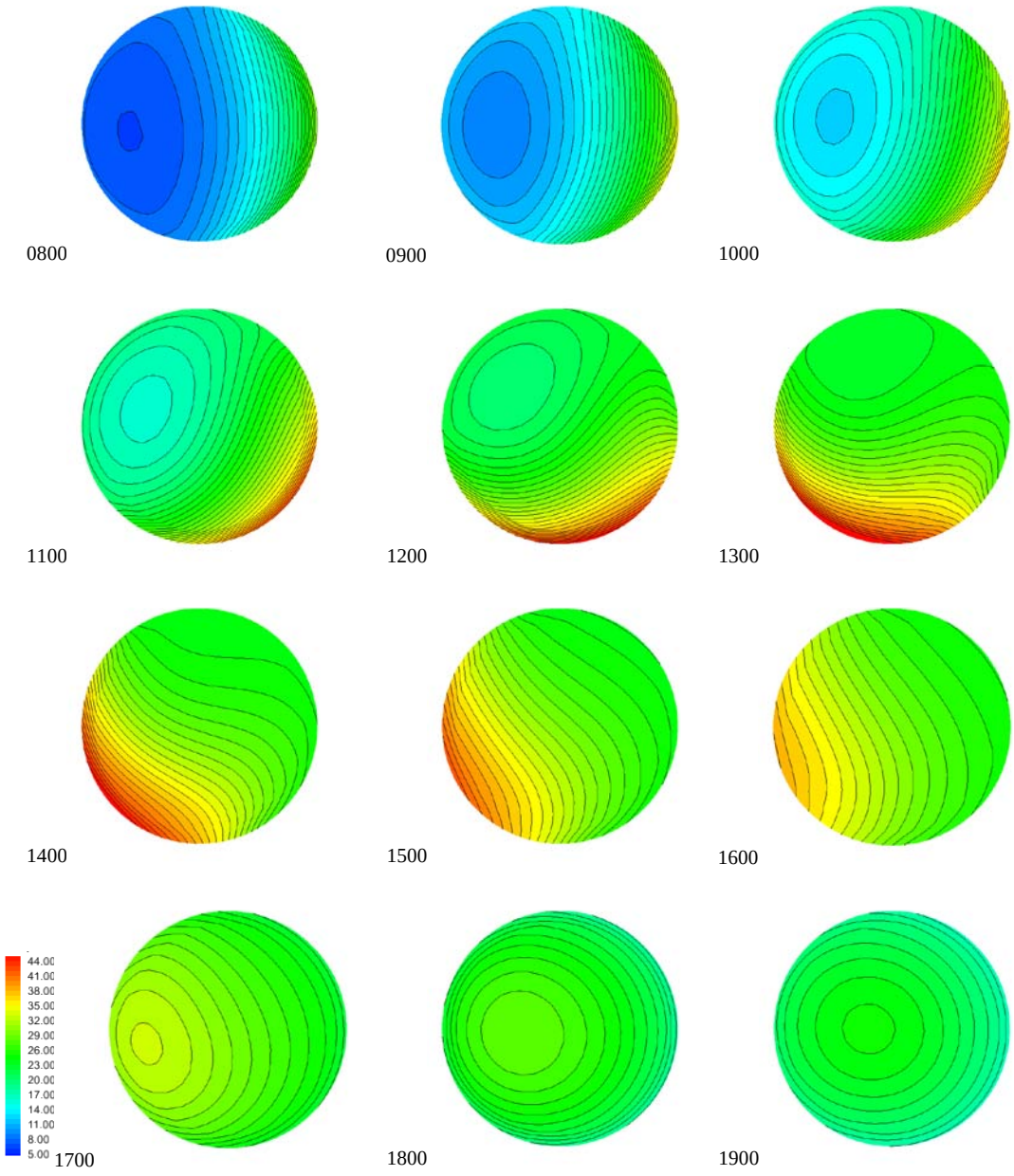


Figure 5.6 Temperature contours from the Derby and Gates pine log simulation. Time is in hours and temperature is deg C

# CHAPTER VI

# TEMPERATE FOREST COMPUTATIONAL DESIGN AND RESULTS

This chapter describes the computational design, development, simulation test matrix, and results of the SRSS as applied to a tree with a root system in a seasonally varying temperate forest.

## 6.1 Computational Design

To fully exercise the capability of the SRSS, a simulation of a tree with a root system in a soil is constructed. The simulated tree contains three different functional materials: the bark, xylem, and heartwood. The simulated soil is a porous medium that has the thermal and hydraulic properties of a sandy soil. The following describes the computational design and specifications of the simulation domain.

### 6.1.1 Background

In March of 2010, an oak tree was selected in Vicksburg, MS for root geometry analysis. A light detection and ranging (LIDAR) system was used to collect surface soil, trunk, and branches geometry. The LIDAR system scans the surfaces and calculates discrete three-dimensional locations of points on the surfaces which are later used for generation of the mesh. After the surface data were collected, the soil surrounding the roots was excavated using high pressure compressed air. This method allows efficient removal of the soil without significantly disturbing the larger roots of the system. After the roots were exposed (Figures 6.1 and 6.2), an additional LIDAR scan was collected for

the roots (Figure 6.3). These data were merged with the previous LIDAR data and used to construct the mesh geometry for the temperate forest simulation.

Figure 6.1 Excavated root system of the Vicksburg tree

Figure 6.2 Side view of the excavated root system of the Vicksburg tree

### 6.1.2 Geometric Design

The computational domain was developed in three sections. The trunk, roots, and soil were divided because of the complexity of the construction of the root system. First the external mesh of the trunk was derived directly from the LIDAR point data. The trunk section starts at the soil surface and extends approximately 2-m above the soil. The point data were cleaned of errors and redundant points. The cleaned data set was meshed as a triangular mesh with an average element size of 0.01-m.

The root mesh was developed independently from the trunk mesh. The LIDAR data of the roots contained some noise, and direct meshing of the point data was not successful. Instead, the point data was used to determine the centerline, width, and length of the roots (Figure 6.3). From the root centerline data, the roots were constructed as solid geometry segments then merged and meshed as a triangular mesh. The average mesh element size was 0.01m. Once the root mesh was completed, it was merged with the trunk mesh and formed into a watertight composite mesh (Figure 6.4). This merged mesh was cleaned of intersecting and overlapping triangles. Next the soil mesh was constructed using a LIDAR scan of a soil surface. The surface contains a variety of heights ranging from -0.01 to 0.2 m. This surface was meshed into a soil volume to a depth of 6.0 m below ground surface. The tree and root surface meshes were merged into the soil mesh shell. The tree depth was set to a similar soil depth as observed in the original measurements. The area intersected by the trunk on the soil surface mesh was removed, and the edges of that area of the soil mesh were stitched to the trunk mesh surface.

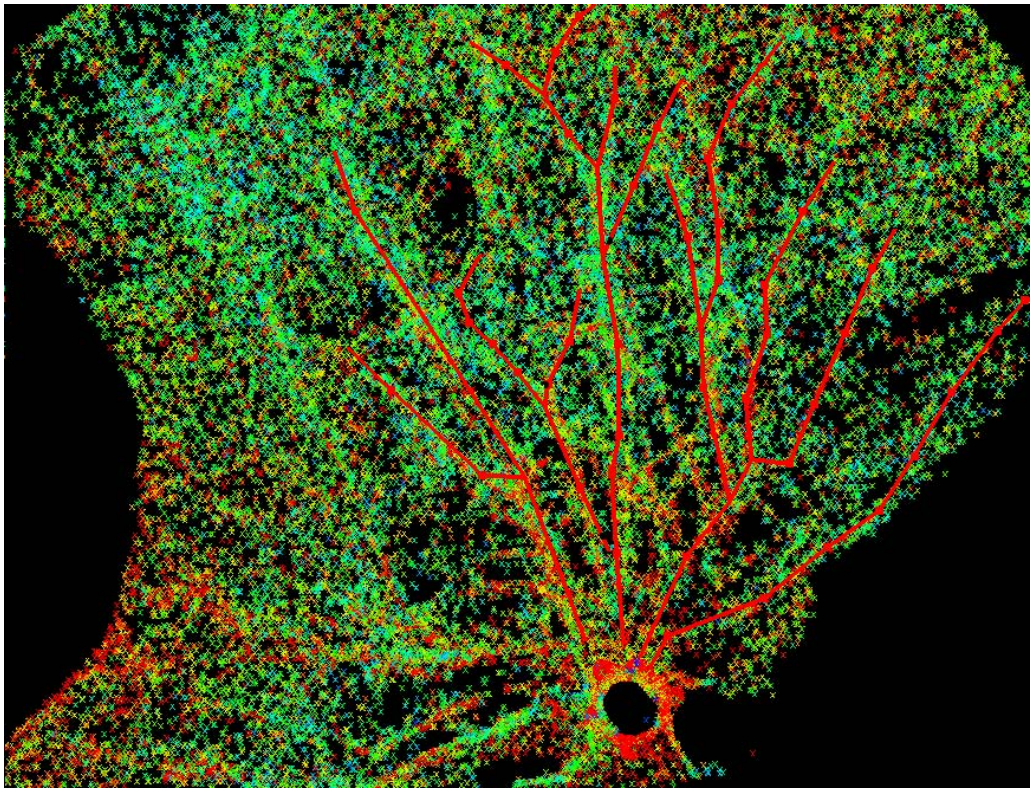

Figure 6.3 Root LIDAR data overlaid with root centerlines

Inner root and trunk meshes were developed last. The first inner layer, which is used to delineate the bark, was generated by extending the trunk and root surface mesh inward (0.006 m) from the surface normal of each of the mesh elements. The inner xylem layers were generated similarly but using only the trunk mesh (Figure 6.5). These inner surfaces were subsequently smoothed and decimated to reduce the computational requirements. This method was chosen so that the inner surfaces matched the shape of the external surface, similar to how the growth rings in the trunk also conform to the external trunk surface (Figure 6.6).

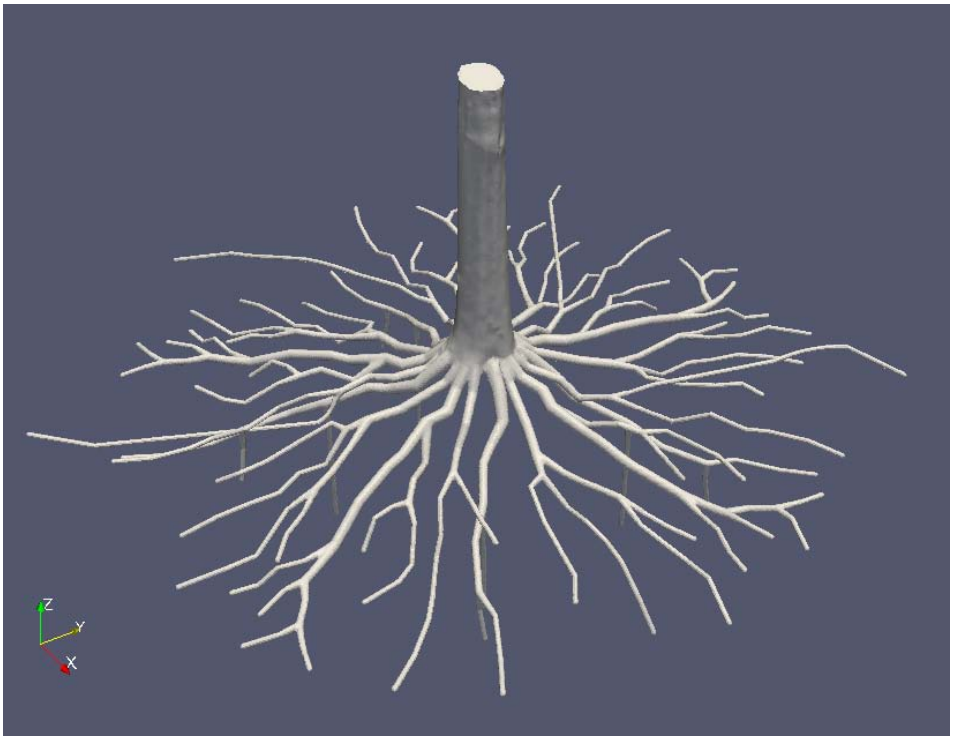


Figure 6.4 Completed trunk and root mesh shell before intersection with the soil

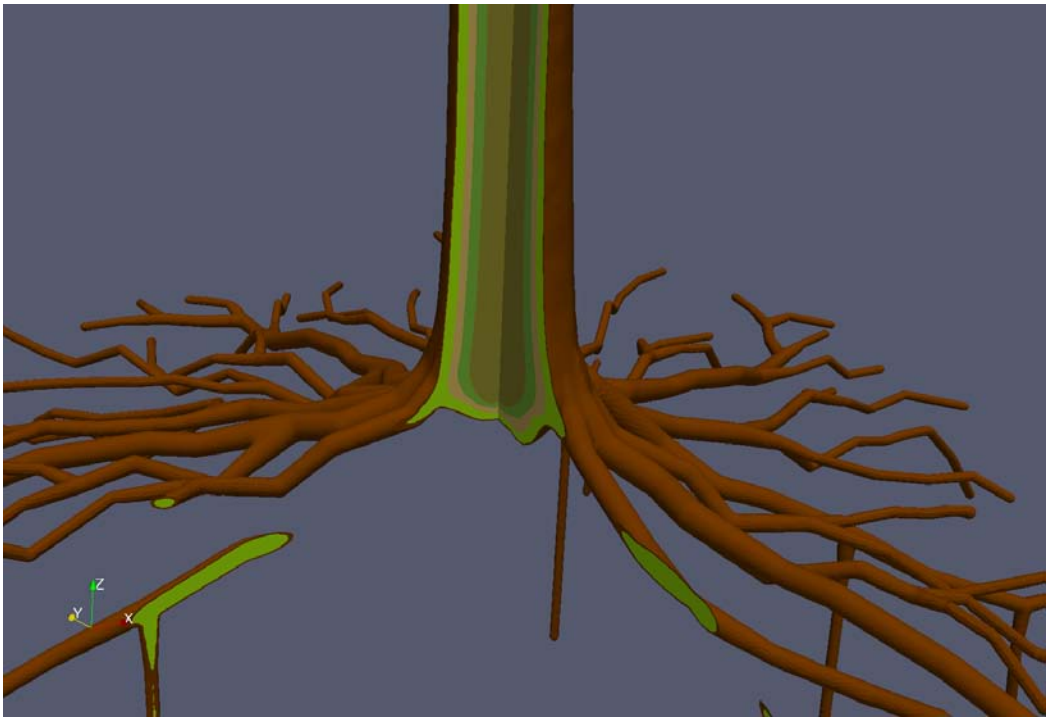


Figure 6.5 The stem and root mesh geometry. The different colors indicate different material types (bark, xylem layers, and heartwood)

The final volume mesh was generated using TetGen[123]. In the meshing process, each of the functional material areas (soil, bark, and xylem areas) was given a maximum region constraint. This allowed control over the tetrahedral sizes for each material region. The meshing was executed on a Cray XT3 with an execution time of approximately 5 hours, and the resulting mesh contained approximately 4.3 million tetrahedral elements (Figure 6.7). The stem of the trunk extends above the surface for 2 m, which is the top of the domain for the simulation. The roots of the simulation extend down into the soil to a depth of 3 m. The stem diameter is 0.4 m, bark thickness is 0.006 m, total xylem thickness is 0.12 m, and heartwood thickness is 0.08 m. The roots in the soil are smaller than the trunk and roughly 2 to 3 m in length with a minimum diameter of 0.05 m. Sections of the roots near the tips of the roots were constructed to allow the passage of fluid from the soil by the fine roots into the root structure. The fine root structure is not modeled at this scale.

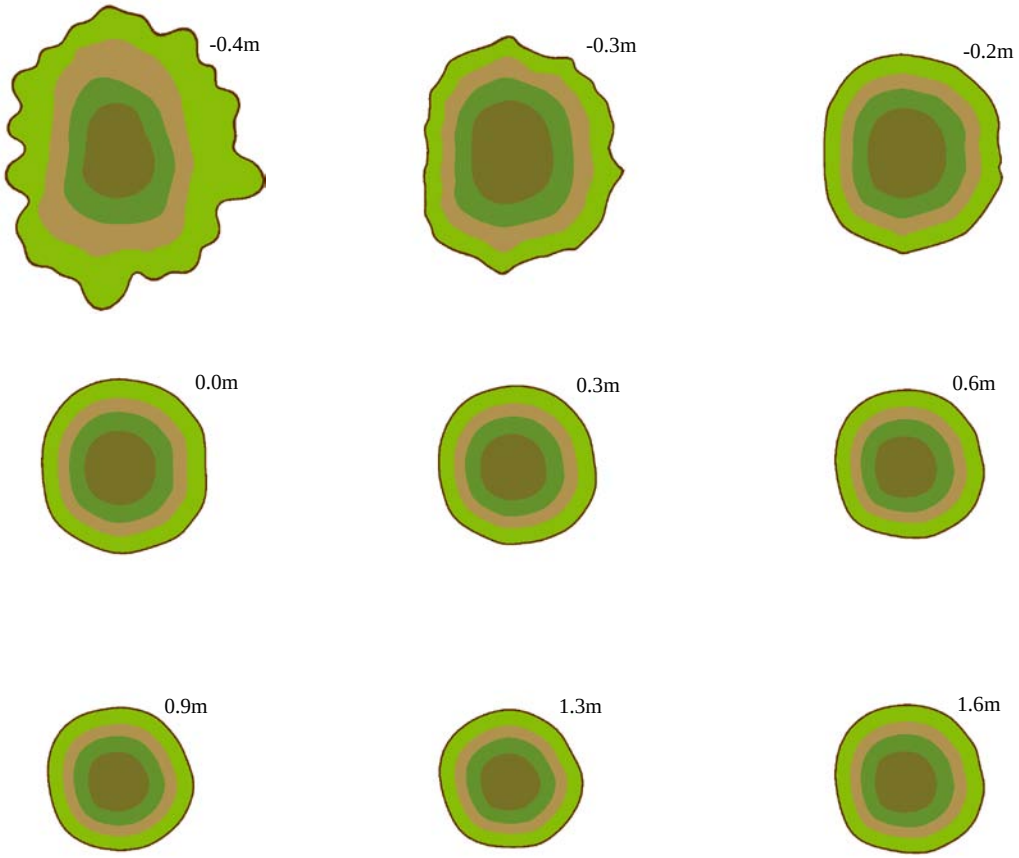


Figure 6.6 Cross section of the trunk at different heights in the computational domain. The layers shown are bark, three xylem layers, and heartwood

### 6.1.3 Material Properties

To correctly simulate the spectral, thermal, and fluid processes of the simulation, the physical, hydraulic, thermal, and spectral properties of the material must be correct. This section describes all the material properties used in the simulation and are consistent with properties of a typical hardwood tree and of a silty sand soil (Table 6.1 and Table 6.2). Physically and thermally, the tree materials are distinct from the soil. The specific gravity of the soil is roughly 3-4 times the specific gravity of the wood and bark. At

saturation, the soil has twice the specific heat capacity of the wood, but porosities are similar.

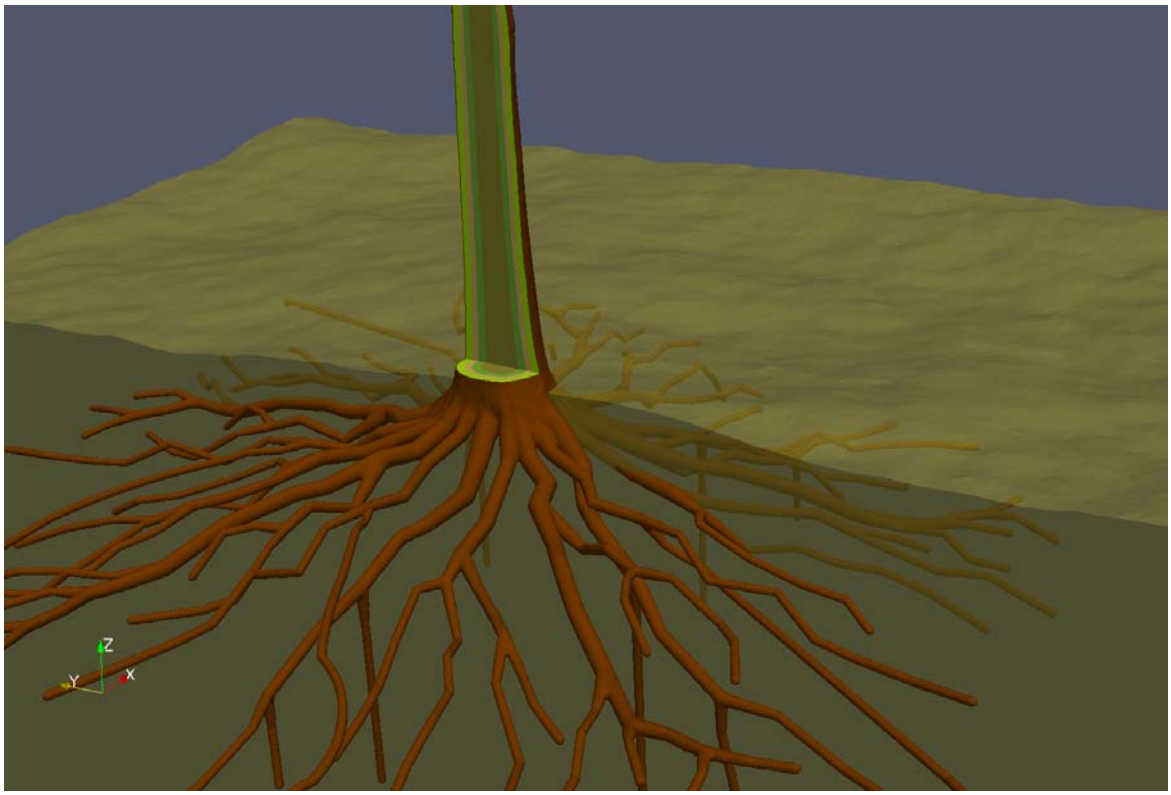


Figure 6.7 Complete meshed domain used in the study. Part of the stem is cut-away to show the different layers inside the stem and root system and part of the soil is hidden to show the root structure

Table 6.3 provides the spectral properties used for the external surfaces in the simulation. These spectral properties are derived from measured samples of oak bark and bare silt soil. The radiative energy calculations in the SRSS are specified as broadband calculations with the distinction made between the shortwave and longwave infrared spectra.

Table 6.1 Physical and thermal properties of the materials in the temperate forest simulation

| Material | Specific Heat ($J\ kg^{-1}\ K^{-1}$) | Thermal Conductivity ($W\ m^{-1}\ K^{-1}$) | Porosity (%) | Specific Gravity | Quartz Fraction (%) |
|---|---|---|---|---|---|
| Bark | 1364.0 | 0.205 | 0.0 | 0.48 | 0.0 |
| Xylem1-3 | 1172.0 | 0.350 | 55.0 | 0.36 | 0.0 |
| Heartwood | 1172.0 | 0.350 | 10.0 | 0.36 | 0.0 |
| Soil (dry) | 1040.7 | 0.271 | 42.6 | 1.40 | 58.0 |
| Soil (saturated) | 2671.0 | 1.904 | 42.6 | 1.83 | 58.0 |

Table 6.2 Hydraulic properties of xylem and soil in the temperate forest simulation

| Material | Saturated Hydraulic Conductivity ($m\ hr^{-1}$) | Residual Saturation Fraction | Alpha[102] ($m^{-1}$) | N[102] |
|---|---|---|---|---|
| Xylem1 | 6.16E-03 | - | - | - |
| Xylem2 | 6.16E-03 | - | - | - |
| Xylem3 | 0.33E-04 | - | - | - |
| Heartwood | 1.33E-06 | - | - | - |
| Soil (saturated) | 6.59E-04 | 0.0223 | 0.36 | 1.425 |

Table 6.3 Spectral properties of surface materials in the temperate forest simulation

| Material | Shortwave Broadband Reflectance (%) | Longwave Infrared Emissivity (%) |
|---|---|---|
| Bark | 36.8 | 98.0 |
| Soil | 42.0 | 90.0 |

### 6.1.4 Boundary Conditions

Boundary conditions for the simulation include both thermal energy and moisture. The bottom of the domain is set to Dirichlet boundary conditions. For unsaturated soil conditions, the water table is set to 17.0 m below the soil surface, and the soil temperature is held to a constant temperature at 6.0 m below the soil surface for the

duration of the simulation. The sides of the domain are set, by default, to no-flow and no-heat flux exchange.

An evaporative exchange boundary condition is specified for the surface of the soil with the atmosphere in the form of evaporation and rainfall interception. The surface of the trunk is not hydraulically conductive, and no moisture exchange occurs. Both the soil and stem surfaces intercept thermal radiation.

Within the soil column, the soil water pressure is initially assumed to be hydrostatic, with the soil moisture depending on the local pressure. Figure 6.8 provides the initial computed soil saturation as a function of elevation calculated by Equation 3.2. As the depth increases, the saturation increases until it reaches the depth of the soil water table. As the pressure field evolves, the local saturation is updated using the constitutive data in Figure 6.9 derived by laboratory measurements of the soil.

For this simulation, it is assumed that the upward transport of fluid is caused by evapotranspiration in the foliage. The xylem cell radii for deciduous trees in a temperate environment can range from 20 - 100 μm in thickness. Observed sap velocity magnitudes for healthy trees in bright solar conditions can range from 0.2 to 0.5 m/h. Using measured sap flow rates, an average velocity rate was developed for full sun conditions. Figure 6.10 illustrates the flow function imposed on the upper boundary of the stem. Considering these flow rates and assuming that the fluid in the xylem has a kinematic viscosity similar to water, Reynolds numbers are approximately 0.03 indicating smooth laminar flow through the sieve-tube cells of the wood.

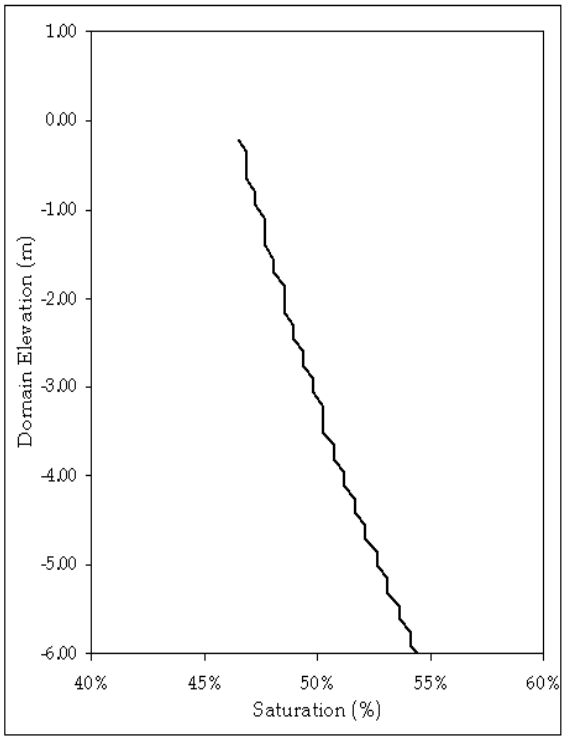


Figure 6.8 Soil saturation as a function of soil depth for the simulated soil

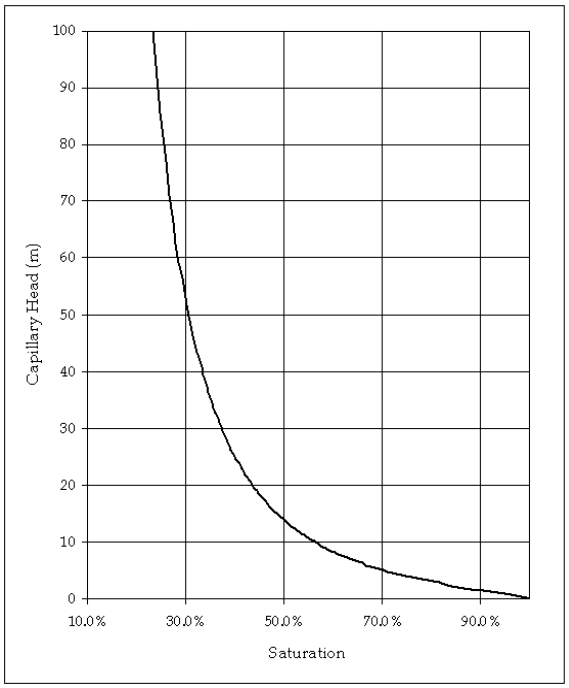


Figure 6.9 Capillary head as a function of the simulated soil saturation

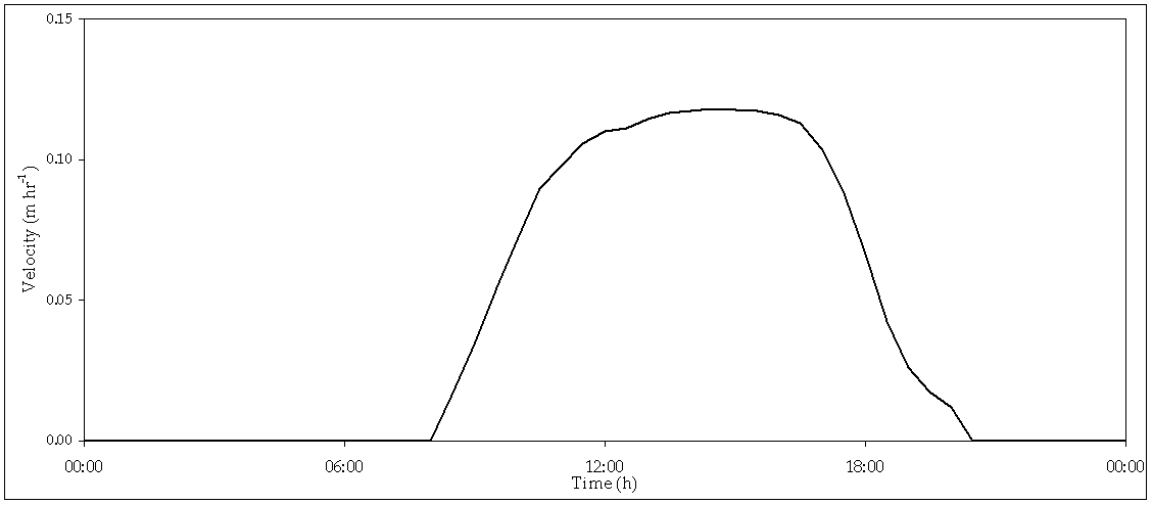


Figure 6.10 Sap velocity function imposed on the upper boundary of the stem

To account for the surrounding forest canopy radiation effects and direct solar radiation, a hemispherical projection image of the surrounding stems and foliage is used. This image projection reduces the computational requirements of the simulation compared to an explicit model of the surrounding forest. The hemispherical image is converted into a two-valued map using image segmentation (simple thresholding [124] ) and removing small gaps resulting in a gap fraction map. The map is then projected back into a three-dimensional hemisphere. For each time step in the simulation, the solar position is calculated and projected through the canopy image hemisphere. If the solar vector intersects an opaque pixel of the image, then no direct solar radiation will reach the surface element of the mesh for that solar position. The surface element instead receives the diffuse part of the solar radiation.

In the simulation, synthetic canopy images generated from a previously validated hardwood forest simulation [125] are used. The viewer is positioned under the center tree, and the surrounding vegetation is mapped 180 degrees into a hemispherical projection. Figure 6.11 illustrates both the summer and winter canopy images used for this method. Figure 6.12 provides simulation examples of each image applied to the computational domain. To complete the radiative transfer processes and to calculate the within-domain radiative transfer between surfaces, the Monte Carlo method described previously in Chapter 4 is used.

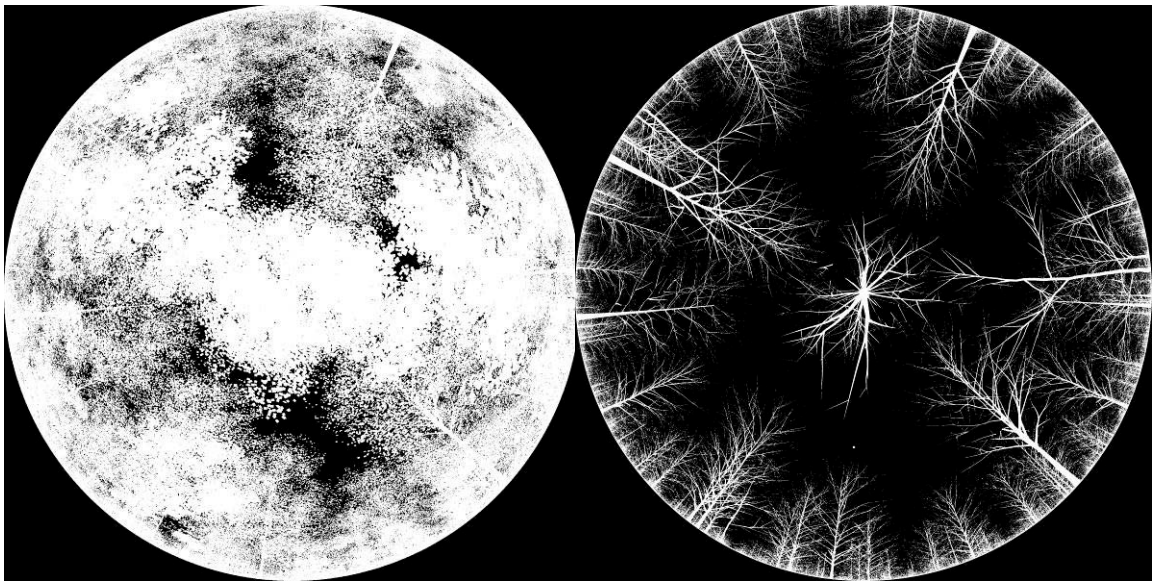

Figure 6.11 Summer (left) and winter (right) hemispherical images used for radiative transfer calculations

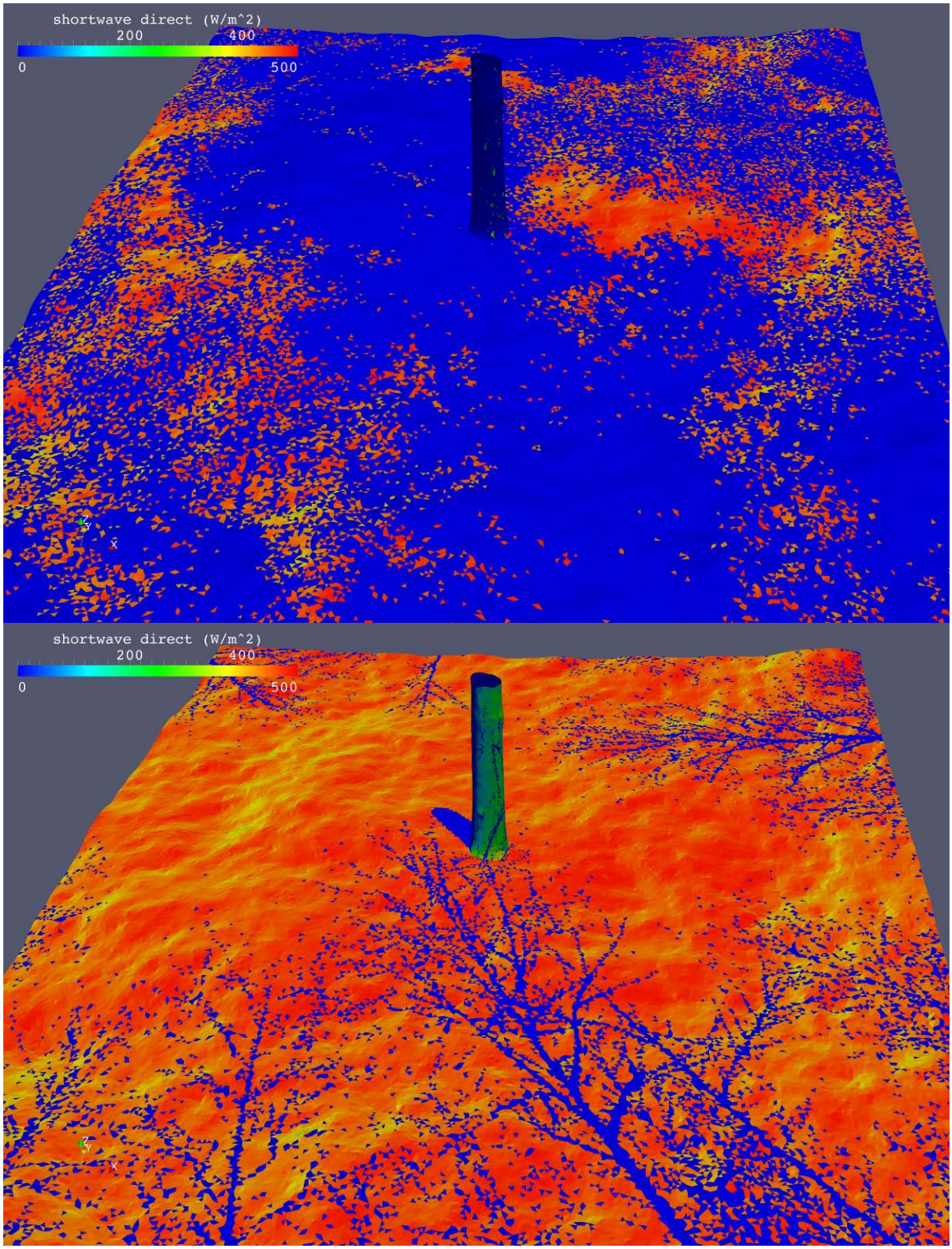


Figure 6.12 Corresponding direct solar radiation calculations using the summer and winter hemispherical images. For purposes of comparison, the external solar radiation flux and angle are held constant for both scenes

### 6.1.5 Meteorological Conditions

The SRSS requires external meteorological and solar data to drive the simulations. The driving meteorological parameters are air temperature, relative humidity, solar radiation (direct, diffuse, downwelling longwave infrared), wind speed, and precipitation. These parameters used in the simulation are typically collected by instruments *in-situ*.

For the temperate forest simulation, two distinct seasonal time periods are selected to illustrate the seasonal effects on the system. The time periods selected are early summer and winter.

The early summer time period is 2-23 May 2010. These data were collected in Vicksburg, MS, USA at approximately 32.0 latitude and 32.304 longitude. The minimum air temperature during that period was 10 deg C, and the maximum was 33 deg C (Figure 6.13). Peak solar radiation was 900 $W/m^2$ (Figure 6.14). Daily near surface temperatures averaged 23 deg C with daily temperature variability of ±10 deg C. Average soil temperature at 1.0-m depth in the soil was 25 deg C with total temperature variability of ±2.6 deg C (Figure 6.15) for the time period.

The winter time period selected for the simulations spans 7 – 21 Jan 2009. These data were collected at the same location as the early summer data and used the same instruments. The minimum air temperature during that period was -5 deg C, and the maximum air temperature was 25 deg C (Figure 6.16). Relative humidity varied diurnally having a typical range from 30 to 90% (Figure 6.17). Peak solar radiation under clear sky conditions was 550 $W/m^2$ (Figure 6.18). Average daily near surface soil temperature was 10.9 deg C with daily temperature variability of ±8.6 deg C. Average

daily soil temperature at 1.0 m depth was 11.3 deg C with a variability of ±4.1 deg C for the time period (Figure 6.19).

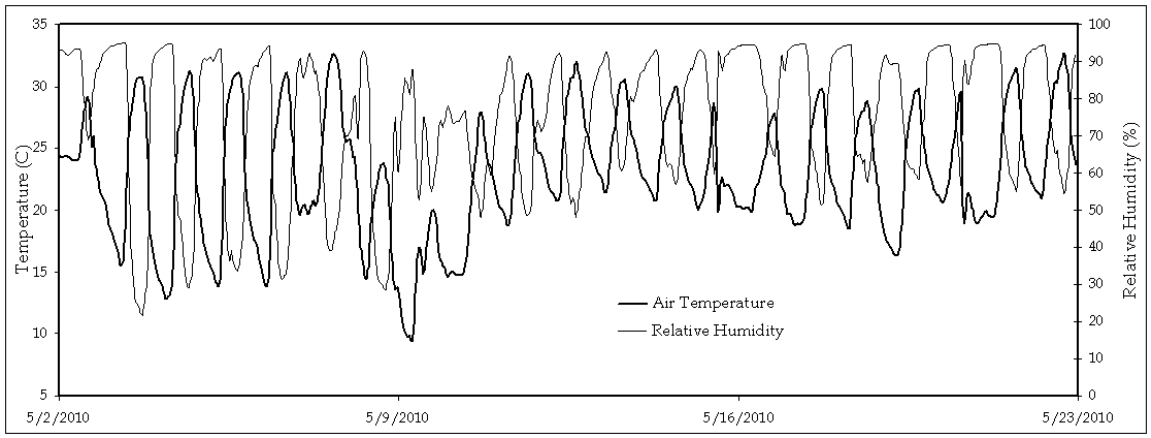


Figure 6.13 May 2010 Air temperature and relative humidity

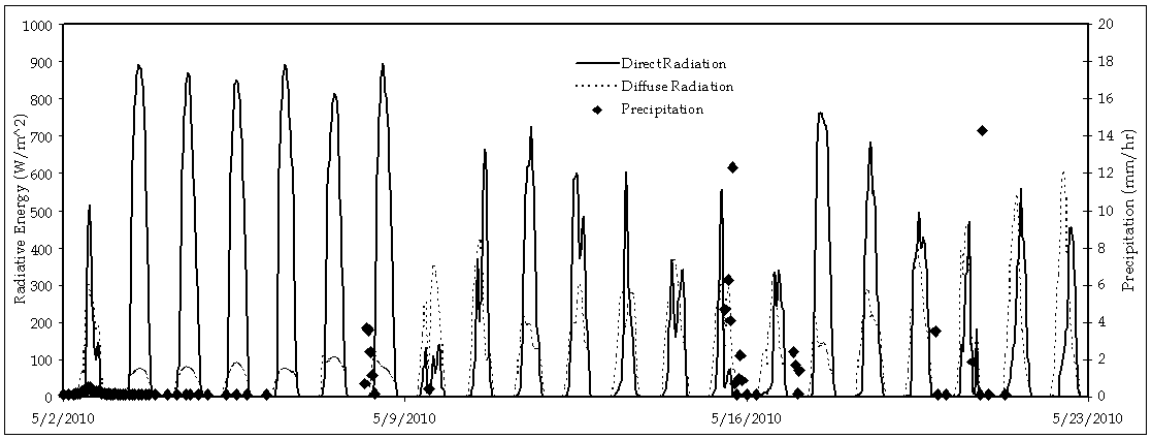


Figure 6.14 May 2010 Solar radiation and precipitation

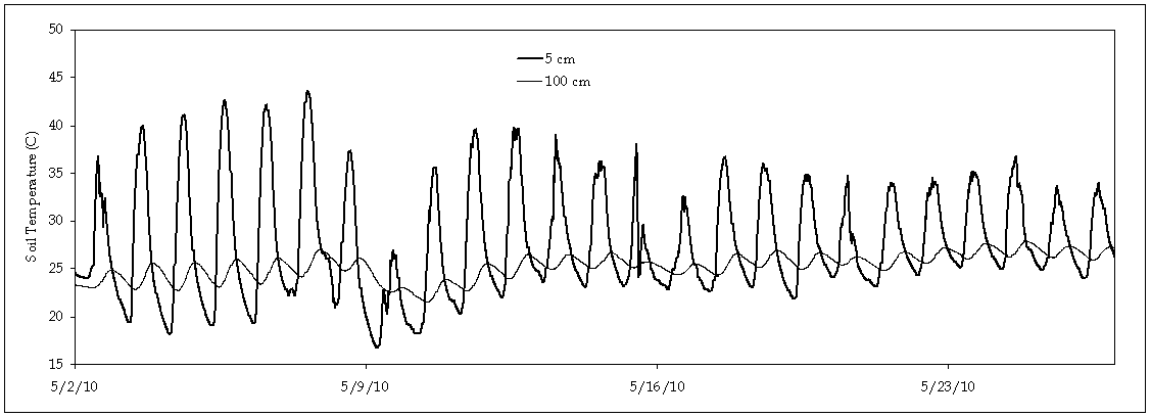


Figure 6.15 May 2010 Soil temperature

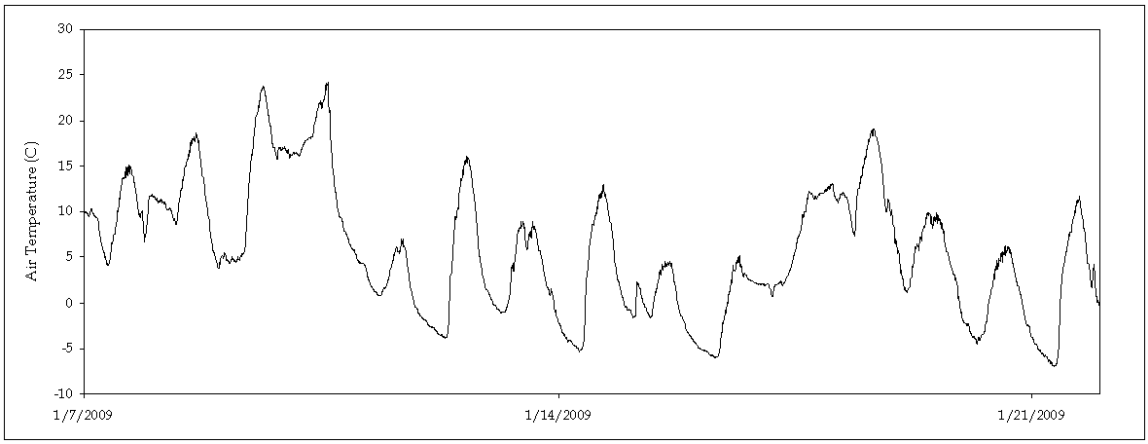


Figure 6.16 January 2009 Air temperature

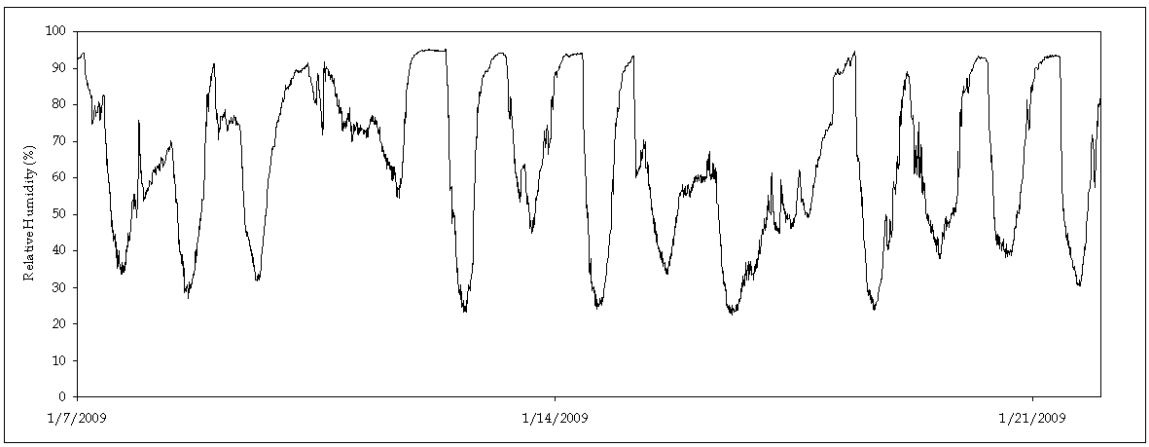


Figure 6.17 January 2009 Relative humidity

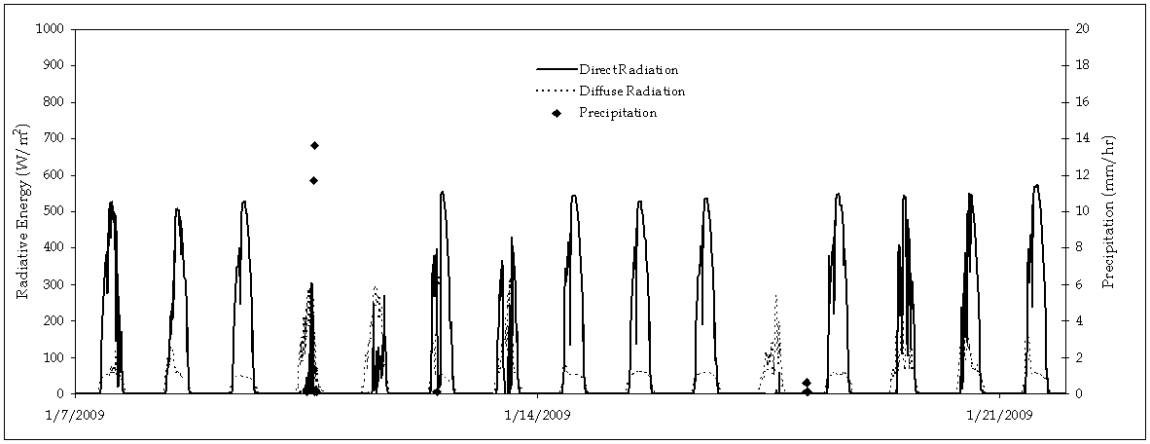


Figure 6.18 January 2009 Solar radiation and precipitation

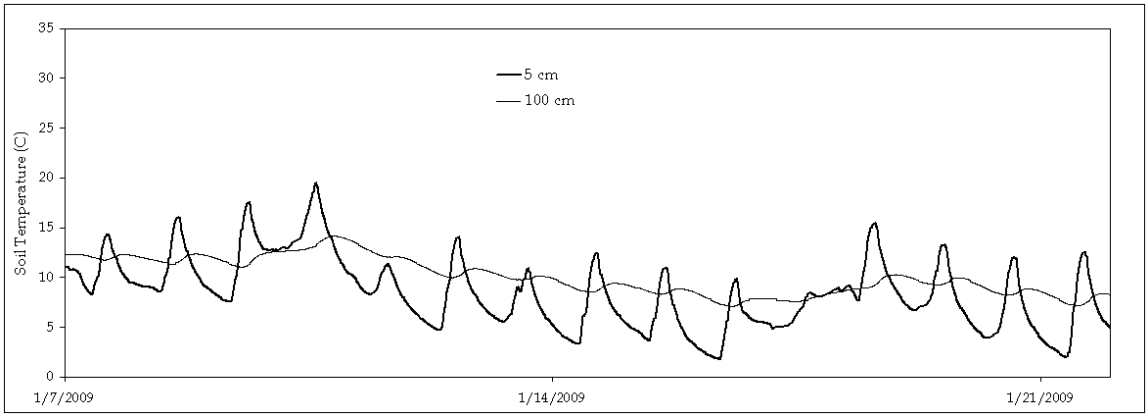


Figure 6.19 January 2009 Soil temperature

## 6.2 Simulation Matrix

This section describes the simulation test matrix used to examine the effects of the stem-root system on the spatial and seasonal distributions of temperature and moisture content in the soil. A combination of seasons, transpirational flow, soil state, and solar environment are varied for each simulation (Table 6.4). In the simulations, a solar dependent time step strategy is specified. When no solar illumination is present, the time step is one hour. But when solar illumination is present, the time step is shortened to 15 minutes. In previous simulations, not presented here, larger time steps during solar illumination created artificial, discontinuous thermal patterns on the external surfaces.

Table 6.4 Simulation matrix for the temperate forest

| Name | Seasonal Setting | Fluid Flow | Soil State | Solar Conditions |
|---|---|---|---|---|
| Alpha | Winter | N | Saturated | Winter Canopy |
| Bravo | Winter | N | Unsaturated | Winter Canopy |
| Charlie | Early Summer | N | Saturated | Summer Canopy |
| Delta | Early Summer | N | Unsaturated | Summer Canopy |
| Echo | Early Summer | Y | Saturated | Summer Canopy |
| Foxtrot | Early Summer | Y | Saturated | Open Canopy |

First the winter simulations (Alpha and Bravo) are considered. During the winter, the transpirational demand by the leaves on the tree is stopped, and subsequently the diurnal flow within the tree and roots is diminished to a zero flow condition. Therefore the main aspect of the winter simulation is the examination of the temperature history of the trunk, the temperature differences between the saturated and unsaturated soil, and solar radiative effects. The external solar environment for the winter simulation is the winter sky map image (Figure 6.11b) which contains more sky exposure than the summer sky map image due to the lack of foliage.

The summer simulation set (Charlie, Delta, Echo, and Foxtrot) is larger as a result of the presence of fluid flow in the stem caused by actively transpiring leaves. Table 6.4illustrates the combination of fluid flow with saturated and unsaturated soils. The fluid flow is turned on and off so any thermal convective effects in the simulation can be isolated from the thermal conduction effects. The external solar environment for the canopy is the summer fully leaved canopy (Figure 6.11a) with the exception for the open canopy simulation where it is an unobstructed sky similar to conditions encountered when a tree is isolated in an open field or after a clear cutting harvest of a forest.

These simulations were all executed on a Cray XT3 using 1072 processors. The Monte-Carlo radiative model of the SRSS used 1024 processors, and the ADH soil model

used 48 processors. Walltime for each time step of the simulation was approximately 55 minutes.

## 6.3 Winter Simulation Results

This section of the chapter presents the results of the winter simulations. First, the analysis includes description of the diurnal solar radiation patterns and magnitude. Second the temperature history of the trunk at various heights and along cardinal radius points in the trunk is presented and discussed. Finally for this section, the soil temperature history is compared between the saturated and unsaturated soils.

### 6.3.1 Winter Solar Radiation

Figure 6.20 illustrates the dynamic range of total shortwave radiation in the scene for the simulated day of 8 Jan 2009. At 0900 hrs the total shortwave radiation range was 15.6 to 20.0 $W/m^2$, and at solar noon (1300 hrs) the range increased to 33.0 to 356.6 $W/m^2$. The seasonal lower solar zenith angle of the sun causes the longer shadows during the day. With a leafless tree canopy, the trunk surface receives a significant amount of shortwave radiation flux.

### 6.3.2 Tree Trunk Winter Temperature History

The group of Figures 6.22 – 6.27 presents the internal temperature history of the trunk at a height of 0.6m above the ground for both the Alpha and Bravo simulations. The 0.6m above ground height is the standard height for basal measurements used in the forest industry. The internal trunk temperature history in both Alpha and Bravo are identical since there is no fluid flow, and the external thermal radiation is the same. For the analyses, points are selected along the cardinal axis from the trunk surface to the center of the trunk (Figure 6.21). The temperatures of the north radius (Figure 6.22)

show a moderate increase, and the near surface temperature tracks closely with air temperature. This is the north side of the trunk surface that is not directly illuminated, and the surface energy flux is primarily from longwave thermal radiation and scattered shortwave radiation. The other internal temperatures follow the classic expected sinusoidal pattern over time.

The east radius of the trunk at 0.6m (Figure 6.23) is similar to the north radius except that the east surface receives some early direct solar radiation (Figure 6.20) as demonstrated by the elevated temperature at the 0.034 m depth. The south radius (Figure 6.24) is drastically different as expected. The near surface temperatures are 10 deg C greater than the north or east radius at solar noon. The penetration of the heating is also evident into a 0.12m depth in the wood. Also noticeable at the near surface temperature is the effect of shading on the surface of the trunk. The neighboring trees cast shadows over the surface of the tree (Figure 6.20 1200 hrs for example) and cause a rapid change in incident shortwave radiation and near-surface temperatures.

The west radius (Figure 6.25) illustrates the afternoon heating of the tree. Peak temperature in the afternoon (1700 hrs) is indicative of the radiative heating also combined with the increase in air temperature. Both of these factors contribute to increased temperatures in the trunk as compared to the east radius. Figure 6.26 is a temperature difference history between the east and west radius. West nodes from the mesh along the axis were compared to east nodes at a similar distance from the surface of the trunk. So when the temperature difference is negative, the west temperature is warmer than the same location along the east axis. At solar noon, the east near surface is 2 deg C warmer than the west side, and later during the day at 1500 hrs, the west side is 5 deg C warmer than the east side.

Similarly for Figure 6.27, the temperature differences between the north and south cardinal axes are shown. Throughout the 24 hour period, the south is 1 deg C warmer than the north side, and at solar noon the south is 10 deg C warmer. Subsequent conduction of the heat is observed in the deeper positions of the trunk. Late in the evening (2000 hrs) after the sun has set, the deeper wood (0.18-m) is still 5 deg C warmer than the same position on the north axis.

Next the conductive and radiative effects of the ground on the trunk are analyzed. Figure 6.28 presents the temperature history for a south radius at three different heights referenced from the ground surface. These heights are 0.3, 0.6, and 1.3-m. The lowest south radius (0.3-m) receives relatively more radiative energy from the soil surface because of the increased view factor geometry with the soil than with the lower radiative energy from the sky and surrounding trees. The total effect of this is an increase of a maximum 1.0 deg C at solar noon when the soil surface reaches a maximum of 15 deg C. The uppermost radius (1.3m) has the cooler temperature of the near surface, influenced by the larger view factor geometry with the sky than with the ground.

### 6.3.3 Winter Soil Temperature History

Figures 6.29 – 6.30 provide the temperature history for the soil in both the saturated (Alpha simulation) and unsaturated conditions (Bravo simulation). By definition, a saturated soil has all the void space completely filled with fluid, and the unsaturated soil has a combination of both fluid and air in the void space. The bulk effect of this is an effective change in thermal conductivity and specific heat of the soil. Consequently a change is expected in thermal response between the two different states of the soil as illustrated in Figure 6.29. For the temperatures in the figure, several nodes

of the surface mesh were selected and the temperatures averaged over the nodes. The unsaturated soil has an increased temperature magnitude compared to the saturated soil. The unsaturated soil has a lower specific heat and subsequently loses and gains heat more quickly than the saturated soil. At 40% saturation, the unsaturated soil has a thermal conductivity of 0.271 W $m^{-1}$ $K^{-1}$, and the saturated soil has a thermal conductivity of 1.904 W $m^{-1}$ $K^{-1}$. Figure 6.30 provides the temperature history of the soil (Alpha simulation) for several depths. At 0.6-m, there are no significant diurnal temperature changes. At the surface depth, the surface reaches a maximum of 15 deg C, and some temperature variation is observed from shadows on the surface.

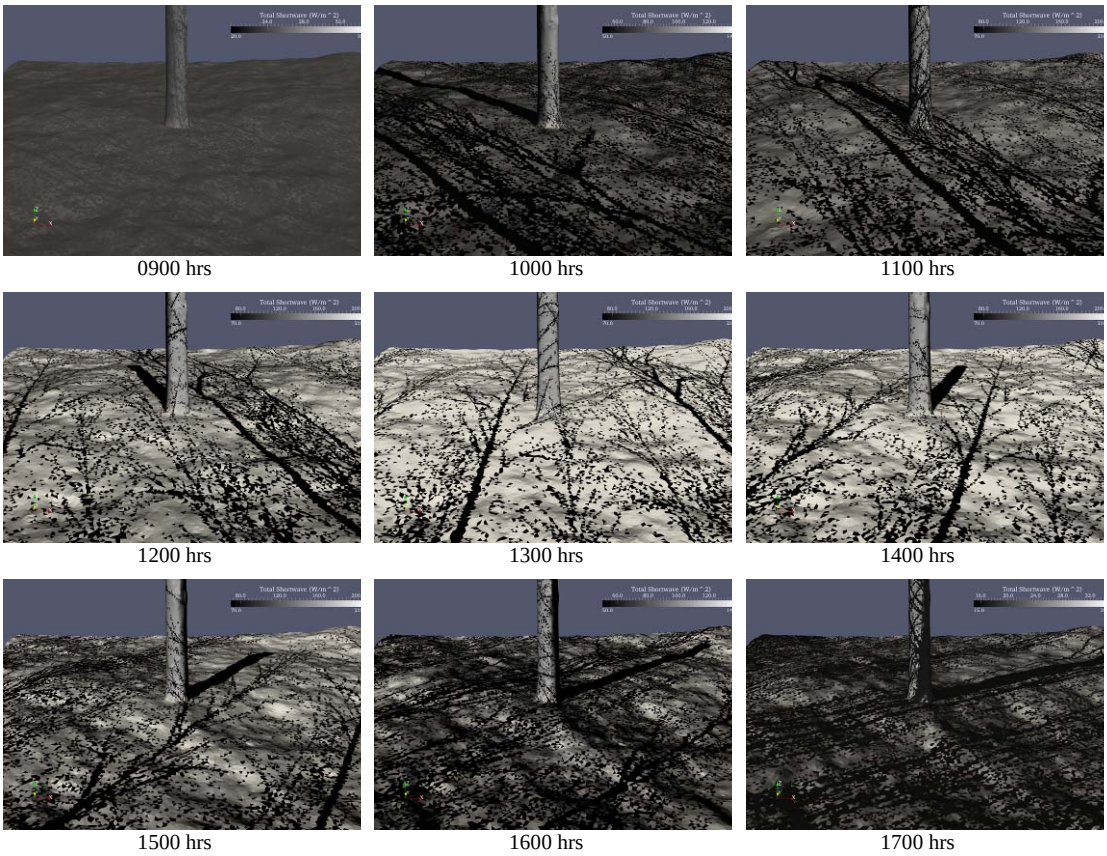


Figure 6.20 SRSS results for the simulated shortwave radiation temporal distribution from 8 Jan 2009, 0900 – 1700 hrs

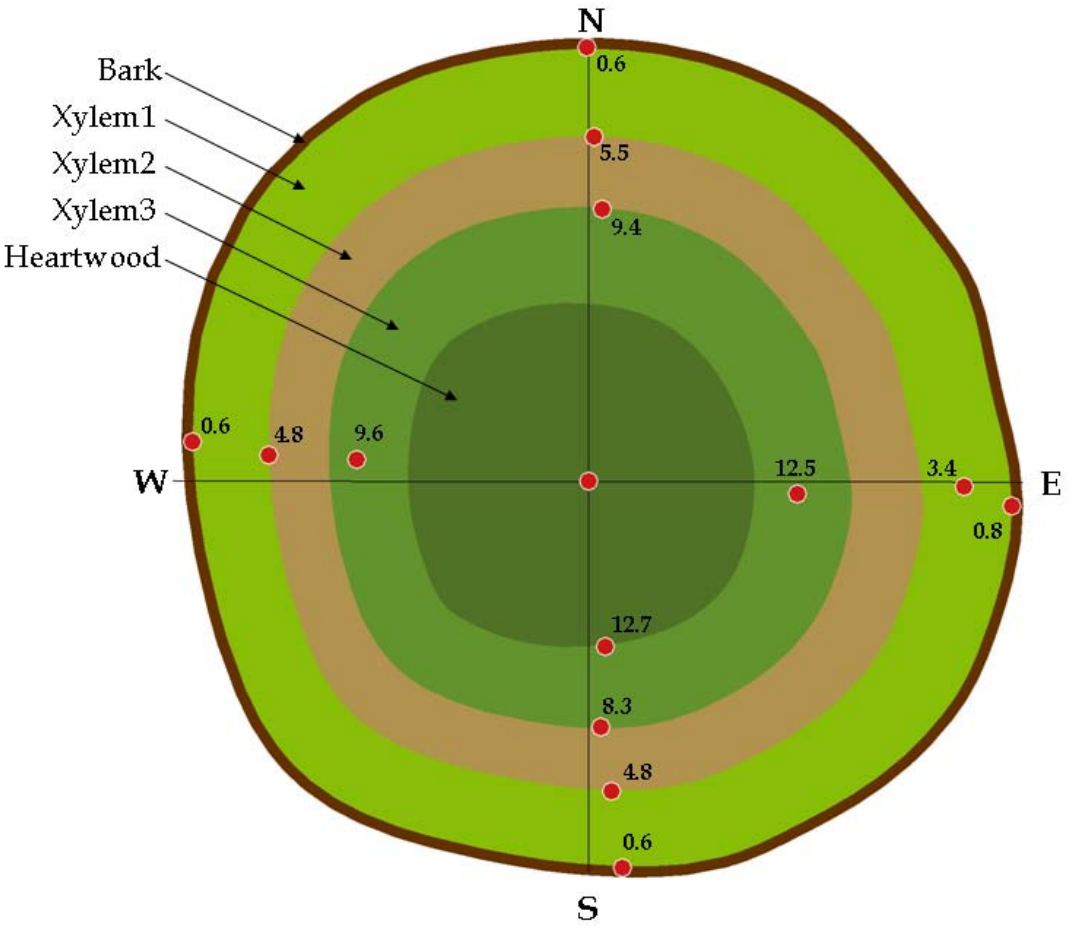


Figure 6.21 Cross-section of the trunk at 0.6m above the ground. The numbers along each cardinal axis indicate distance in centimeters from the trunk surface. These distances correspond with distances shown in the following temperature history charts

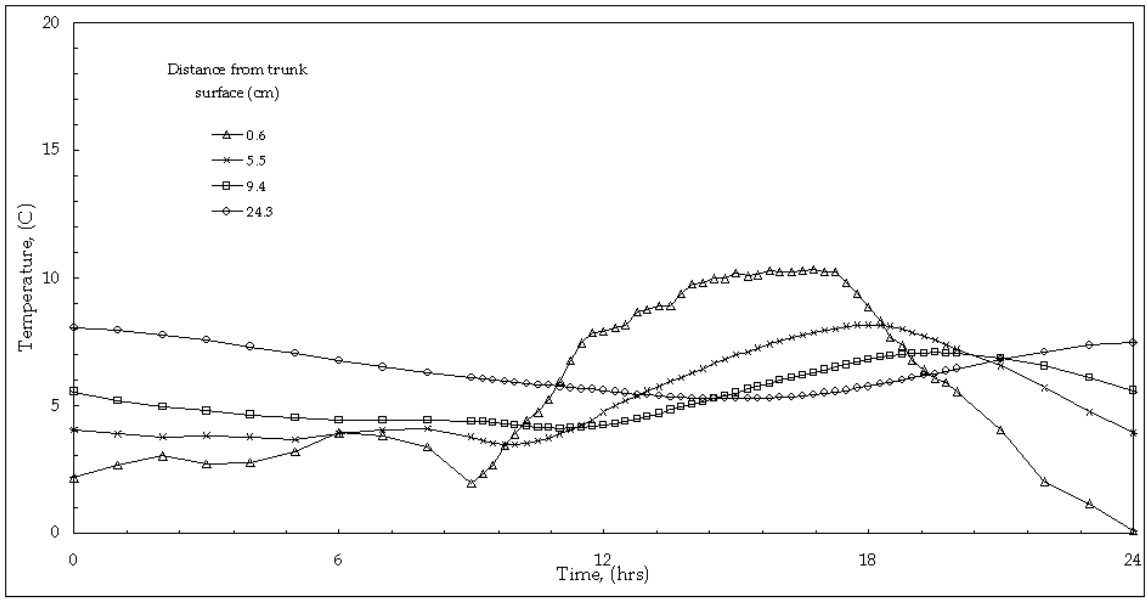


Figure 6.22 SRSS temperature history of the trunk at 0.6 m along the north radius for 8 Jan 2009 (simulation Alpha)

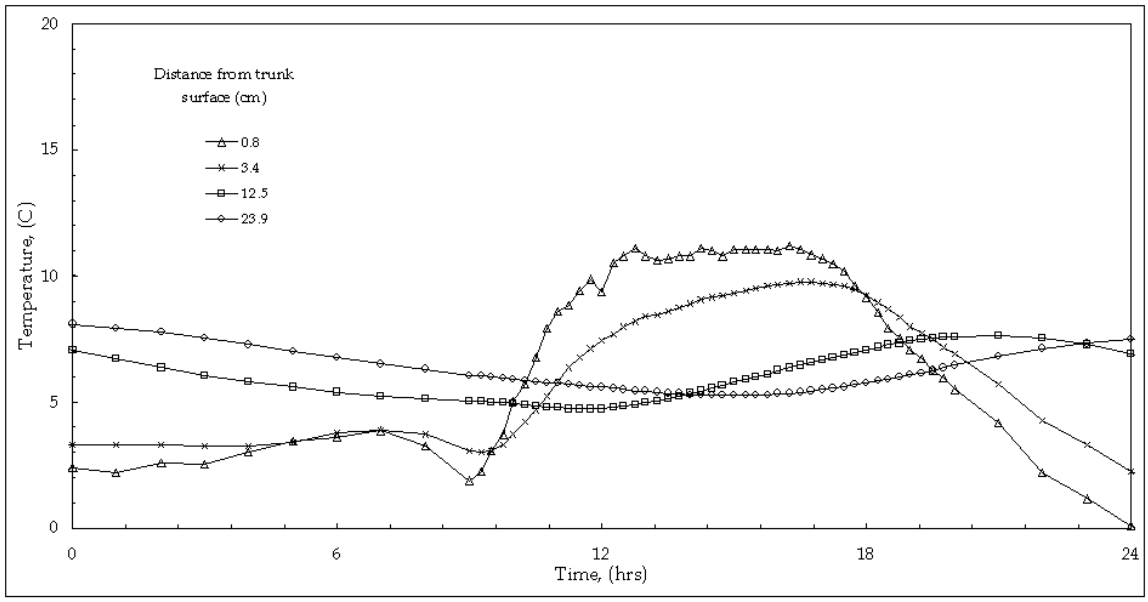


Figure 6.23 SRSS temperature history of the trunk at 0.6m along the east radius for 8 Jan 2009 (simulation Alpha)

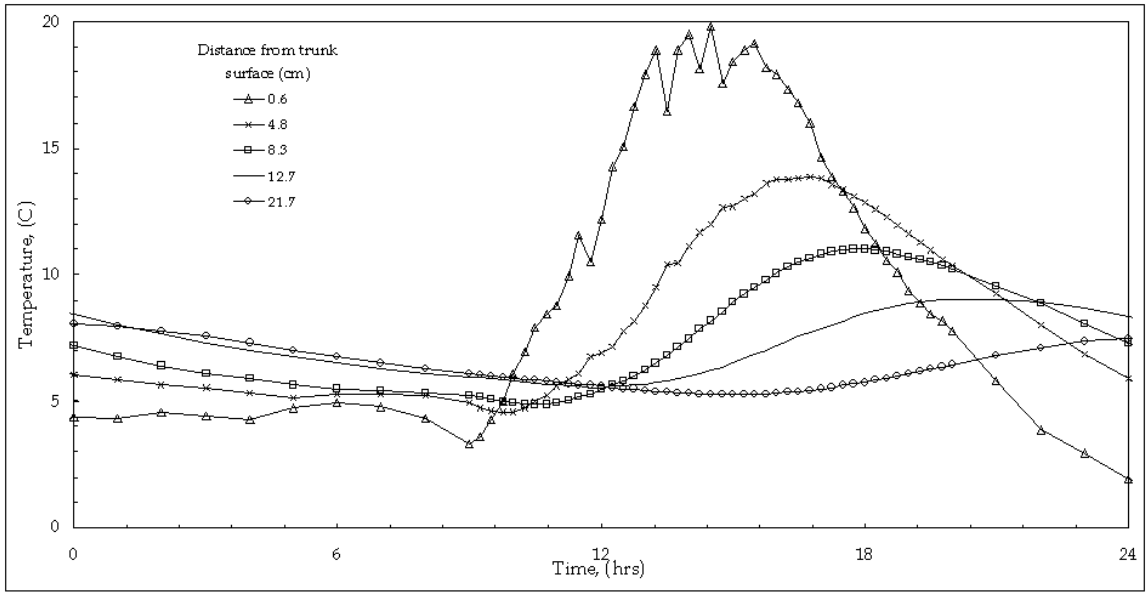


Figure 6.24 SRSS temperature history of the trunk at 0.6m along the south radius for 8 Jan 2009 (simulation Alpha)

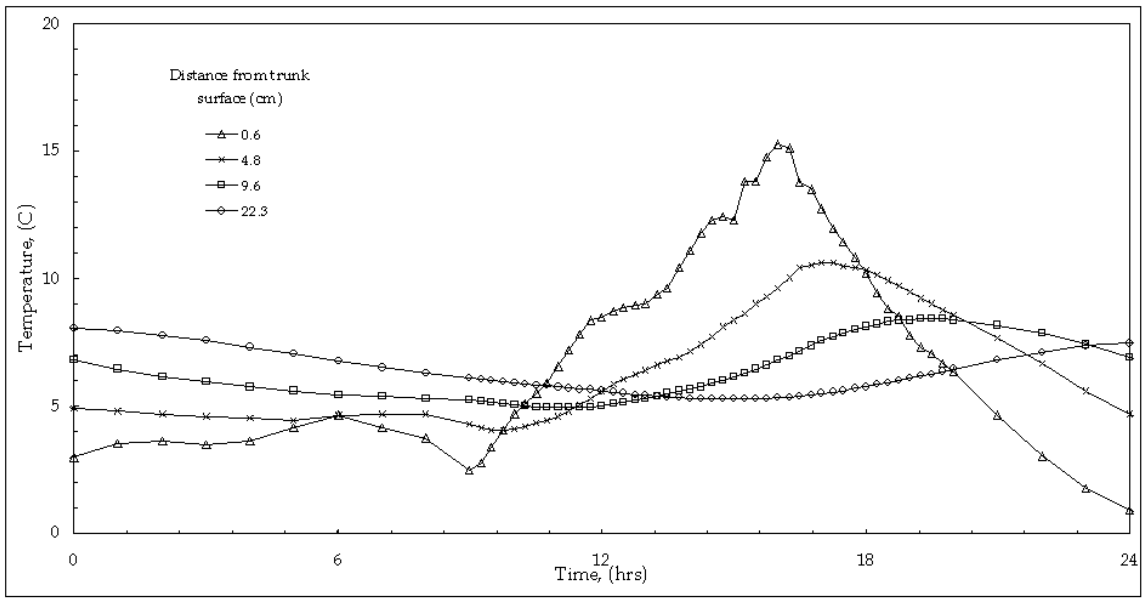


Figure 6.25 SRSS temperature history of the trunk at 0.6m along the west radius for 8 Jan 2009 (simulation Alpha)

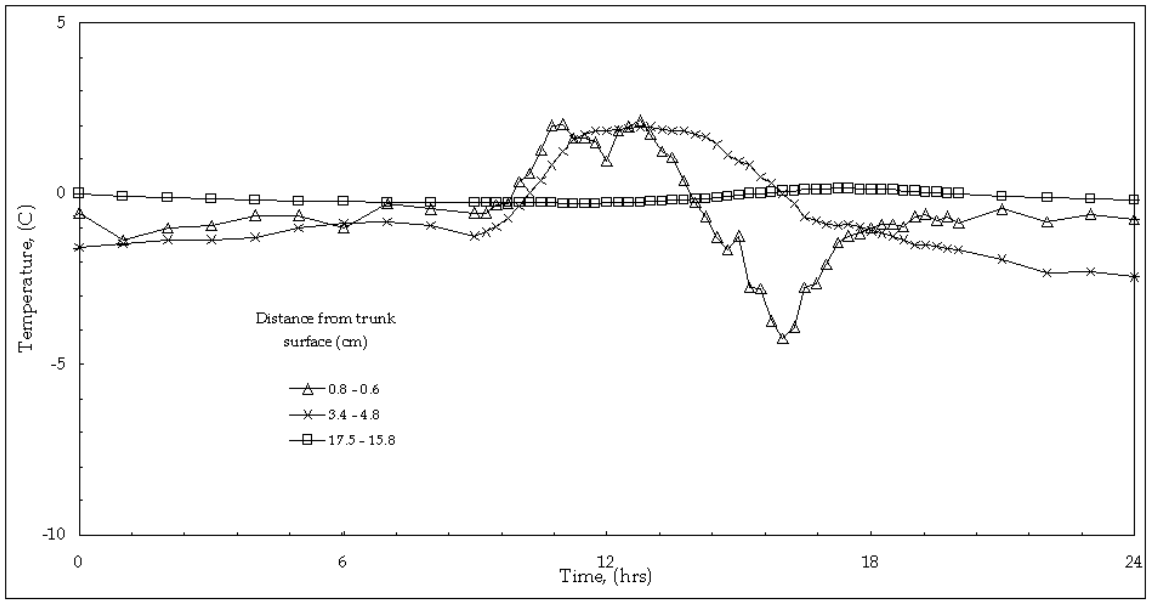


Figure 6.26 Temperature difference in the trunk at 0.6m between the east and west radius for 8 Jan 2009 (simulation Alpha)

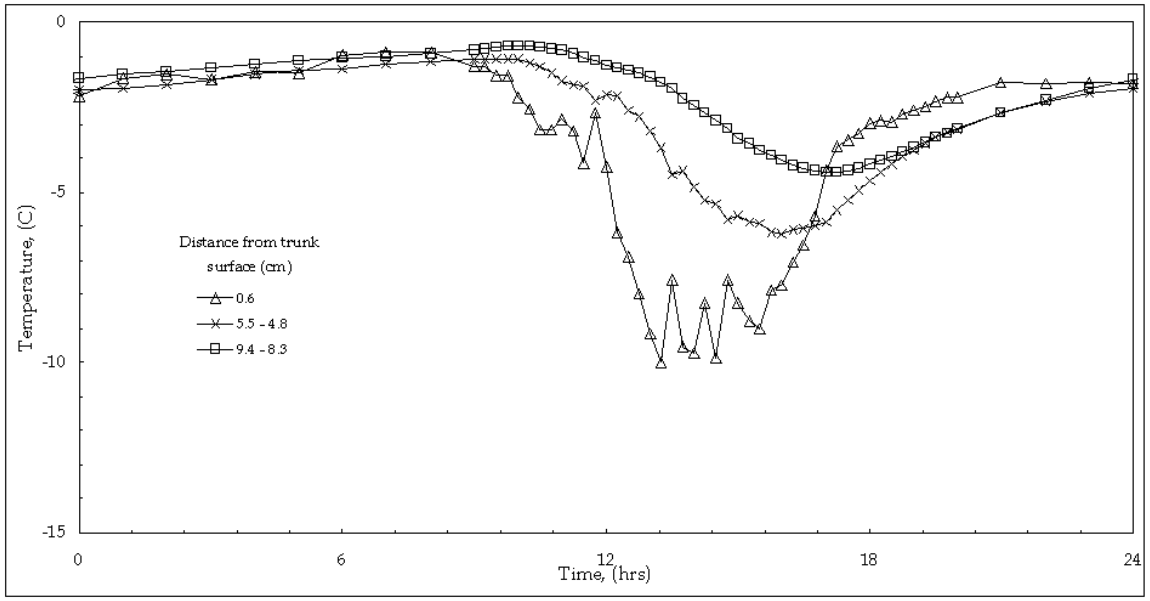


Figure 6.27 Temperature difference in the trunk at 0.6m between the north and south radius for 8 Jan 2009 (simulation Alpha)

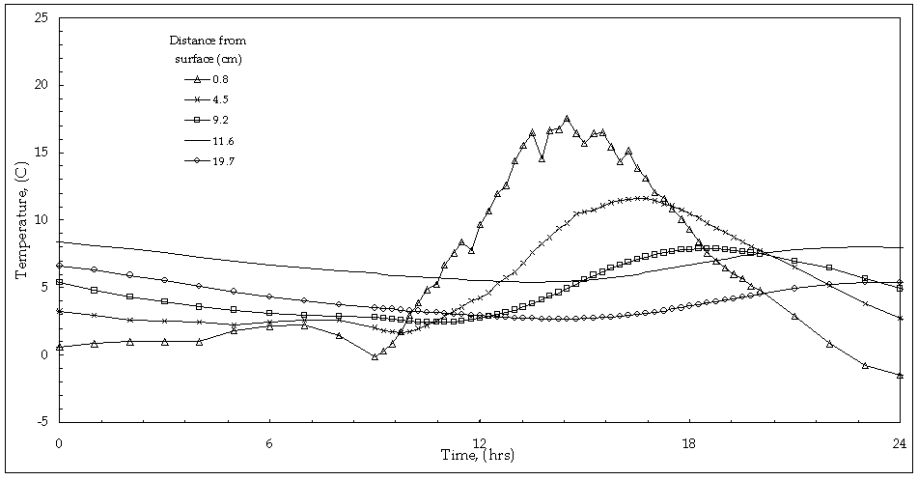


a) 1.3m

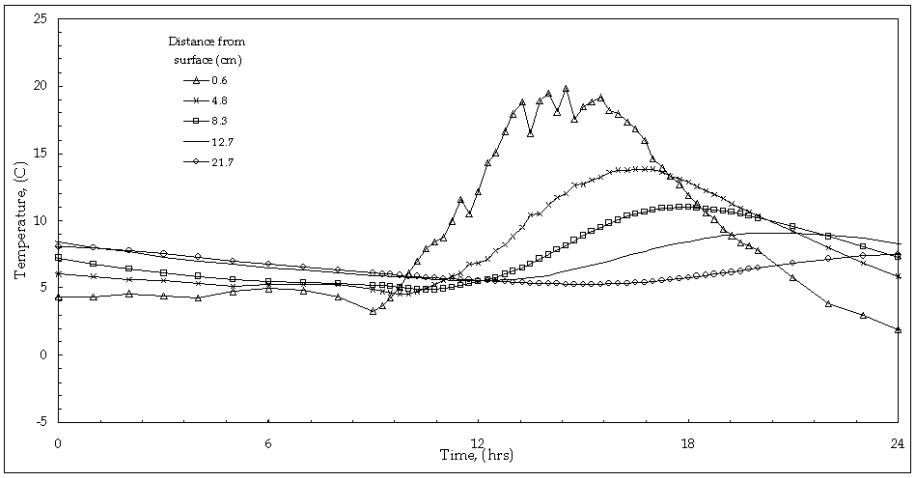


b) 0.6m

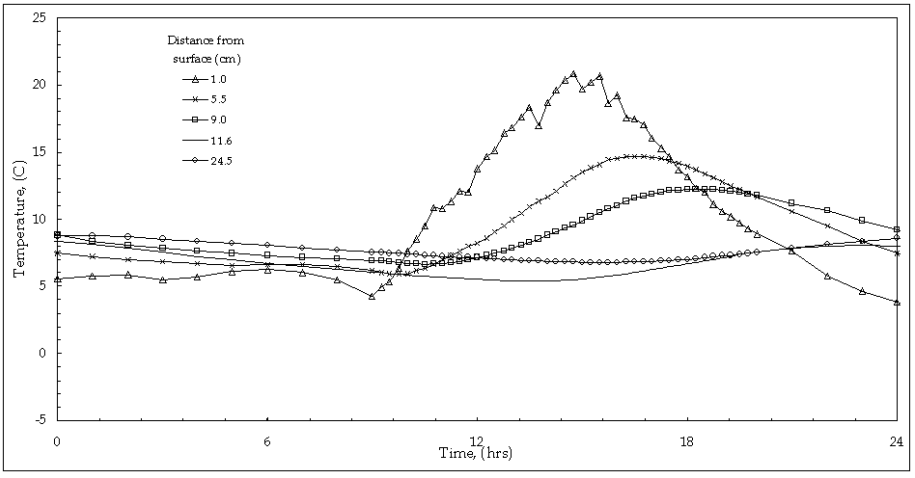


c) 0.3m

Figure 6.28 SRSS temperature history of the trunk along the south radius at 1.3, 0.6, and 0.3m above the soil surface 8 Jan 2009 (simulation Alpha).

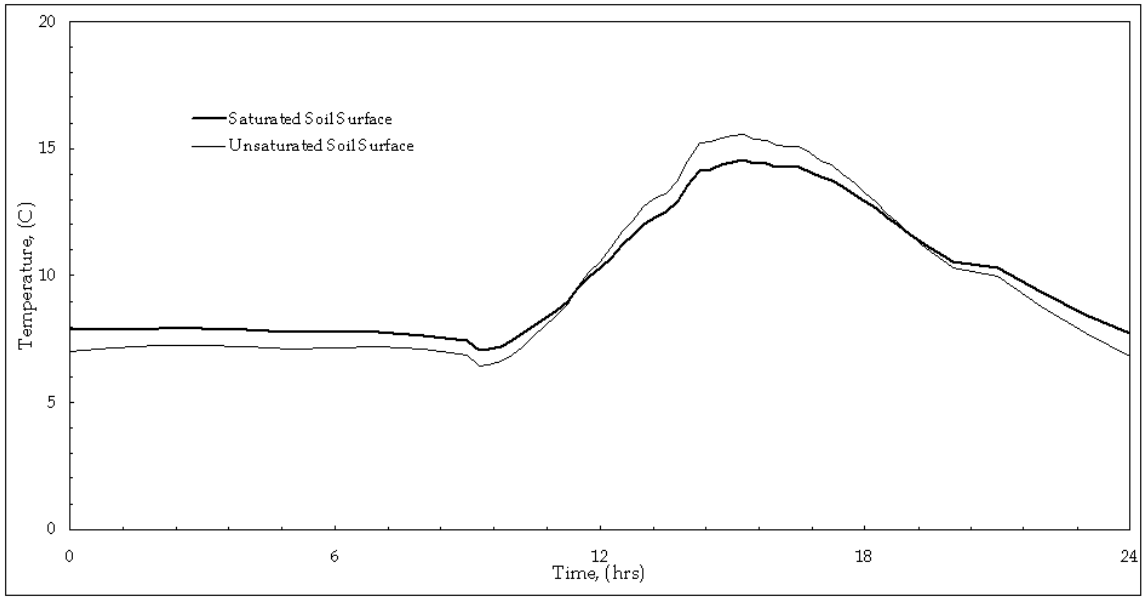


Figure 6.29 SRSS simulated surface temperatures for the winter unsaturated (Bravo) and saturated (Alpha) soil conditions

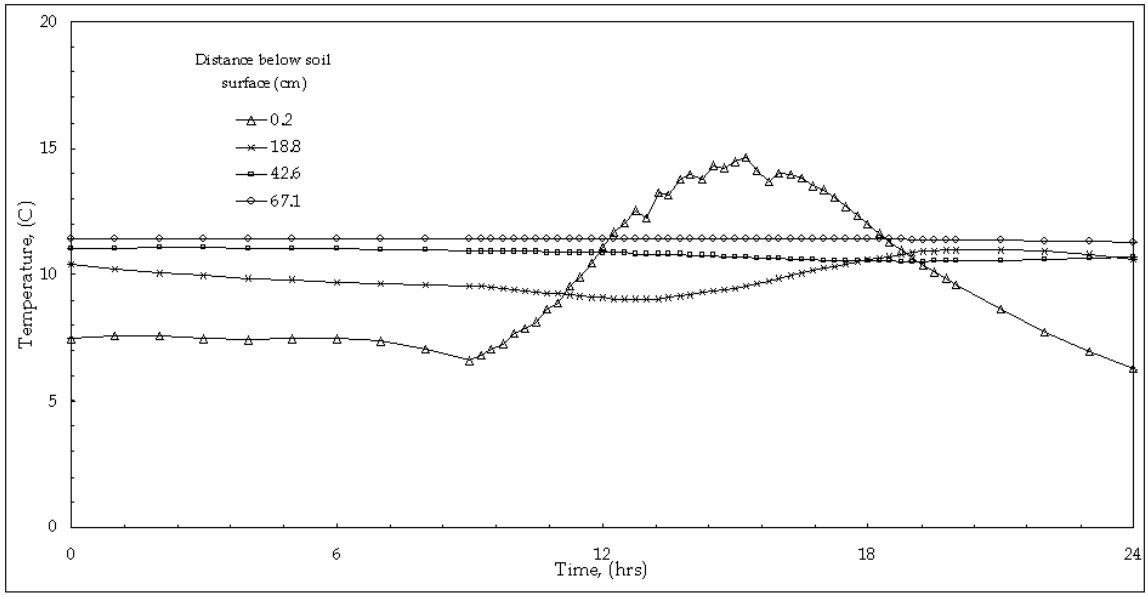


Figure 6.30 SRSS simulated soil temperatures at depth for the winter saturated soil conditions (simulation Alpha)

## 6.4 Summer Simulation Results

This section of the results presents the four early summer simulations as described in Table 6.4. Three of the simulations (Charlie, Delta, and Echo) concern the permutations of fluid flow and soil state. The remaining simulation (Foxtrot) is an open canopy that is used to examine the effects of neglecting the radiative energy of the surrounding forest canopy. The temporal span of the simulations is 2-4 May 2010. This temporal span represents days of clear skies with high solar radiation and no precipitation.

### 6.4.1 Early Summer Solar Radiation SRSS Results

Figure 6.31 and Figure 6.33 illustrate the simulation results of the total shortwave radiation under a fully leafed deciduous forest canopy (Figure 6.11a) for the Charlie, Delta, and Echo simulations. The mapping represents the dense foliage coverage of the forest during early summer. The gaps in the forest canopy produces the speckled patterns observed on the ground and on the trunk. For most of the time, 0800-1700 hrs, the trunk is shaded and receives only diffuse radiation. Incidentally, this is similar to the assumptions of the simulations conducted by Herrington [54]. Exceptions to this are during 1000-1100 hrs where a gap in the overhead canopy allows for direct radiation to reach the trunk.

As a contrast, Figures 6.32 and 6.34 provide the total shortwave radiation simulation results of an open canopy for the same time period. In this open canopy simulation (simulation Foxtrot), all the surrounding trees and foliage are removed, leaving only the foliage of the center tree that produces self-shadowing. Differences between the two simulations are an increase of solar radiation incident to the soil and trunk surfaces.

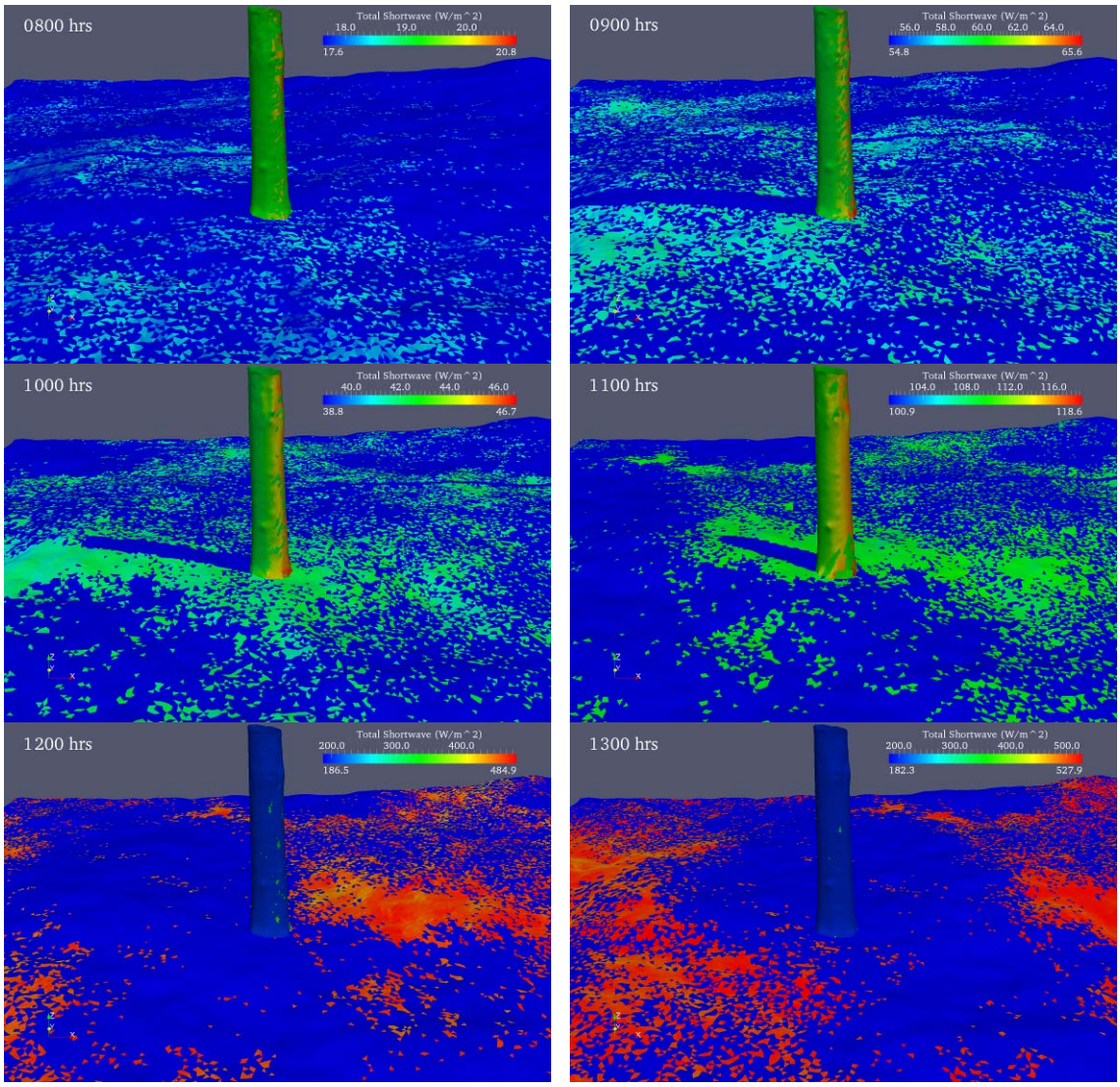


Figure 6.31 SRSS results of total shortwave radiation for 0800-1300 hrs, 2 May 2010 for simulations Charlie, Delta, and Echo.

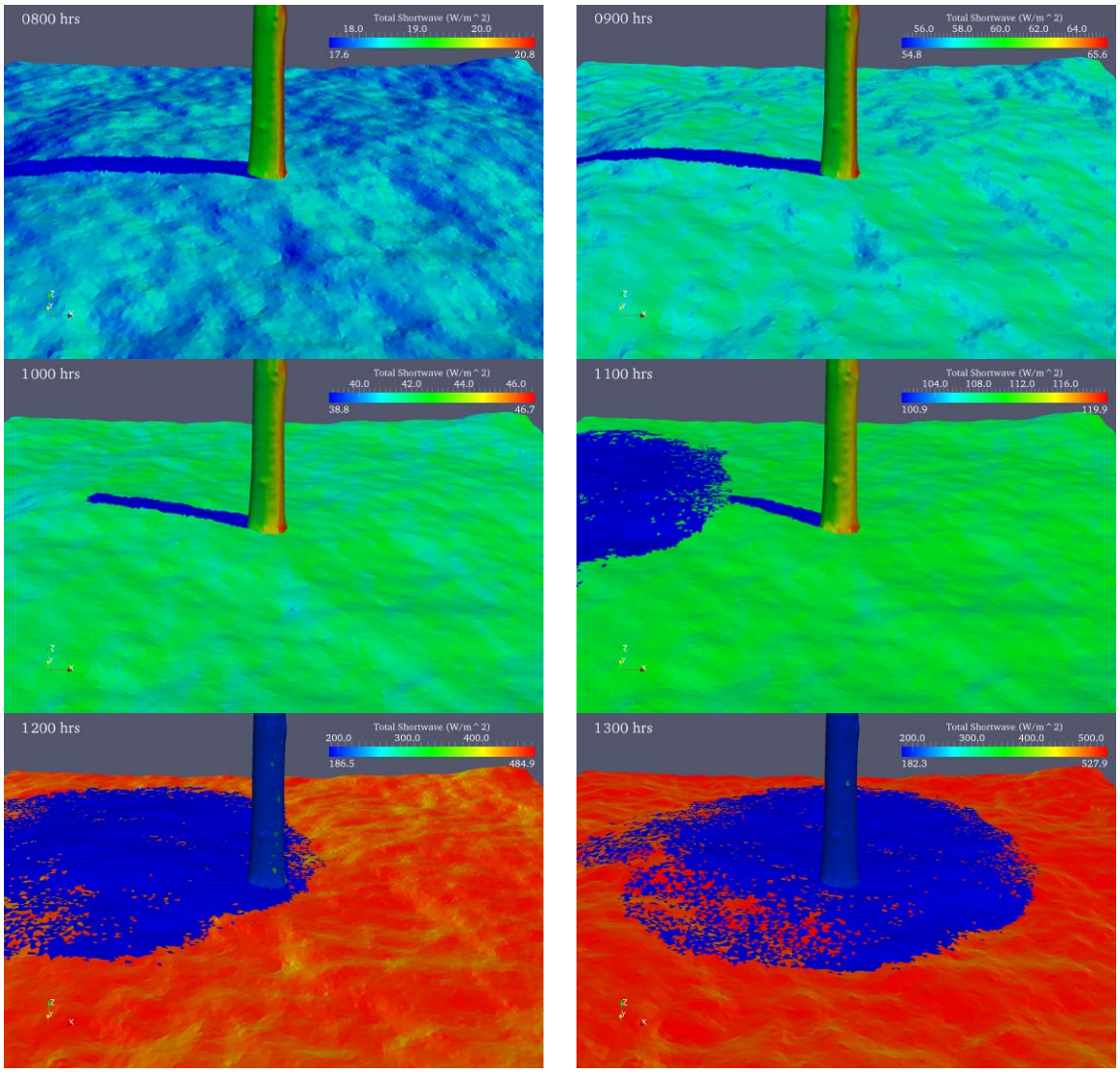


Figure 6.32 SRSS results of total shortwave radiation in open canopy for 0800-1300 hrs, 2 May 2010 for simulation Foxtrot

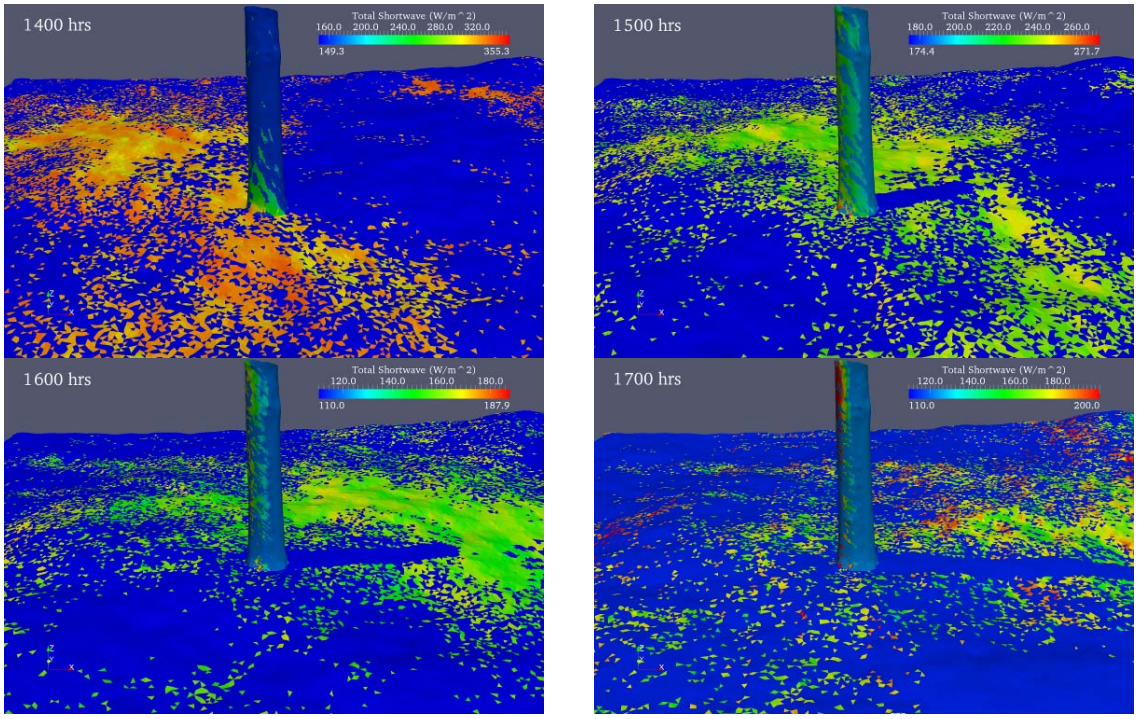


Figure 6.33 SRSS results of total shortwave radiation for 1400 – 1700 hrs, 2 May 2010 for simulation Charlie, Delta, and Echo.

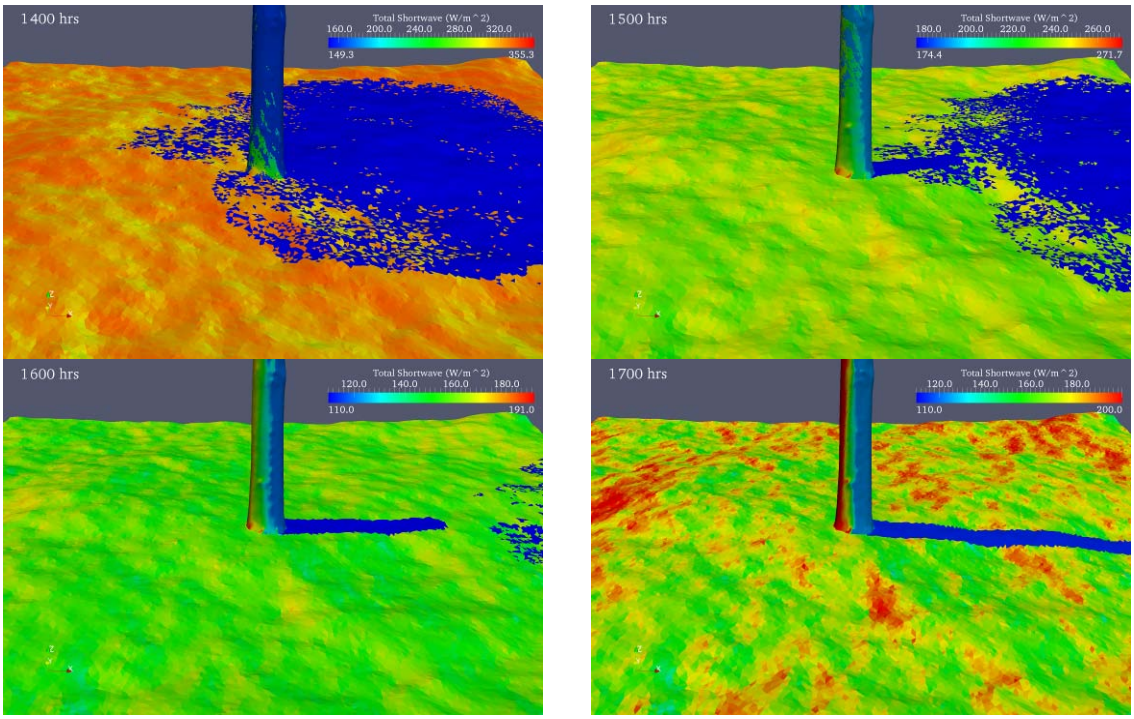


Figure 6.34 SRSS results of total shortwave radiation in open canopy for 1400-1700 hrs, 2 May 2010 for simulation Foxtrot

### 6.4.2 Fluid Flow and Moisture Distribution Results for Early Summer

The boundary conditions for fluid flow due to transpiration have been previously described and shown in Figure 6.10. The velocity demand is converted into a pressure head that is imposed on the top of the stem. The pressure gradient begins at 0800 and ends at 2000 hrs with the peak occurring at 1300 hrs. This specified pressure gradient is determined by using Darcy's law and applied uniformly to the nodes at the top of the computational domain. The boundary condition at the root tips is designed to allow the passage of fluid from the soil into the roots but not conversely.

Figure 6.35 illustrates the spatial distribution of velocity across the trunk at 0.6m at 1300 hrs for simulation Echo. The low or zero velocities shown are expected in the bark and in the heartwood region. The velocity is attenuated by the hydraulic

conductivity and porosity of the wood. All the observed velocity are in the three layers of xylem. Over time the velocities increase and decrease as shown in Figure 6.36 for fluid velocity along the south axis.

Ultimately the fluid flowing through the trunk and roots is extracted from the soil. For the described simulation, the soil is initially saturated to represent the ideal conditions for fluid flow in the soil (Figure 6.37). The saturated soil has the highest hydraulic conductivity, and the boundary conditions at the bottom of the soil provide a limitless supply of water to the system. As the demand for fluid in the tree increases, water is removed from the soil. The tree begins to draw fluid from the soil, and depending on the hydraulic characteristics of the soil, the fluid withdrawal rate from the soil exceeds the rate of replenishment from the surrounding soil making the soil unsaturated. The hydraulic conductivity in these soil regions decreases, and the fluid uptake is shifted to roots that are still surrounded by saturated soil and altering the fluid velocity in the roots (Figures 6.37-6.44). Figures 6.45-47 provide the results of this desaturation and spread of the unsaturated soil over time from 0800 to 2500 hrs. For the first 24 hrs from a fully saturated state, there exist areas that do not recover full saturation. Over a period of time, these areas will grow until they reach a quasi-steady state in the soil. Consequences for the unsaturated regions are twofold. First, the hydraulic conductivity of the soil drops significantly (see Figures 6.8-6.9) causing the root system to draw fluid from other surrounding saturated areas and also increasing velocity in those parts of the roots. The second consequence is that the unsaturated soil will have differing thermal properties (specific heat capacity, thermal diffusivity, and thermal conductivity) from the surrounding soil, resulting in different thermal responses and temperature history.


Figure 6.35 Spatial distribution of flow velocity across the trunk at 0.6m for 1300 hrs 2 May 2010 for simulations Echo and Foxtrot

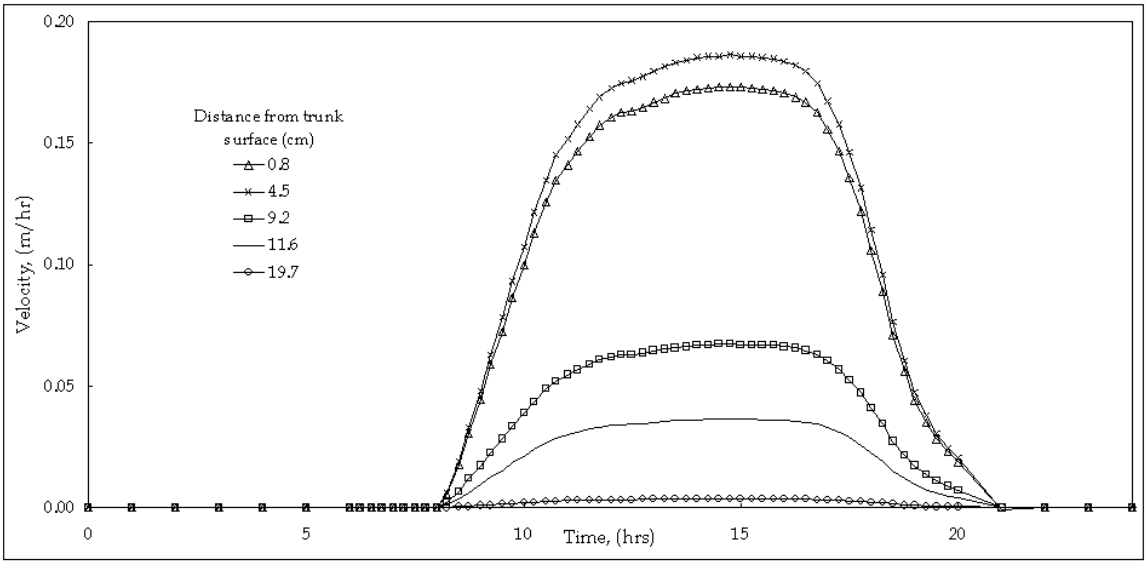


Figure 6.36 Flow velocity history along the south radius of the trunk at 0.6m for early summer for simulations Echo and Foxtrot

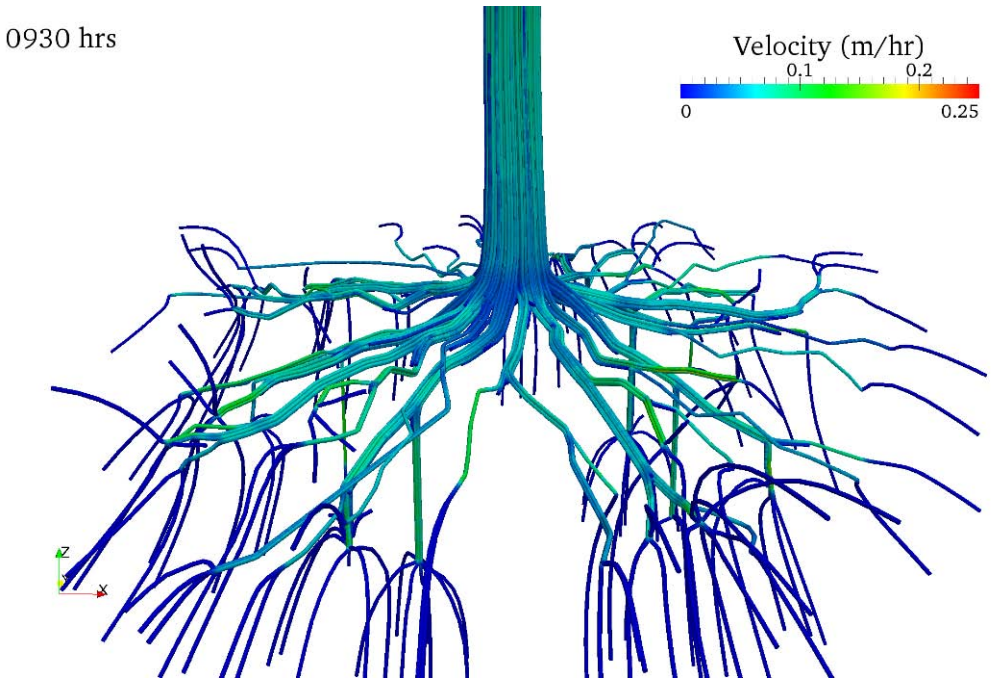


Figure 6.37 Fluid flow lines and velocity for saturated soil conditions 0930 hrs, 2 May 2010 for simulation Echo

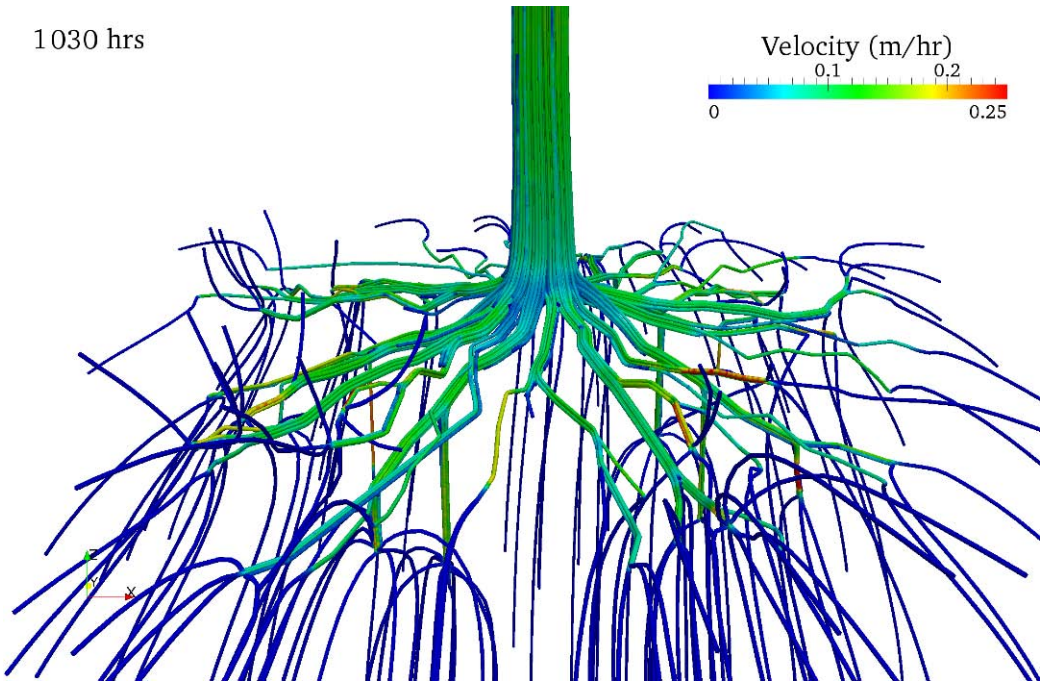


Figure 6.38 Fluid flow lines and velocity for saturated soil conditions 1030 hrs, 2 May 2010 for simulation Echo

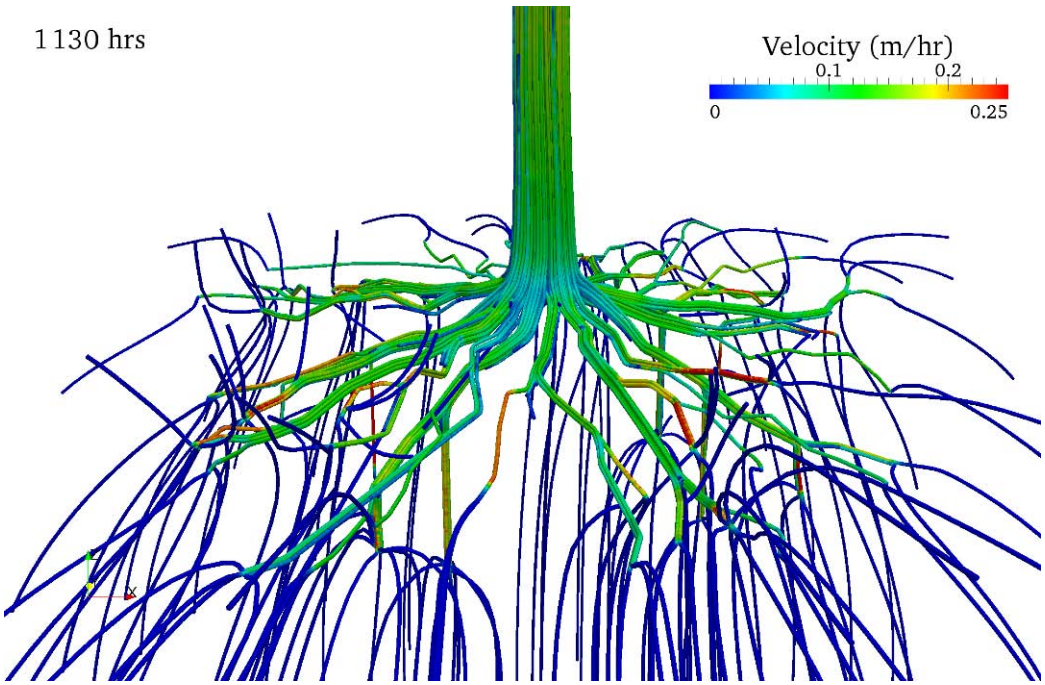


Figure 6.39 Fluid flow lines and velocity for saturated soil conditions 1130 hrs, 2 May 2010 for simulation Echo

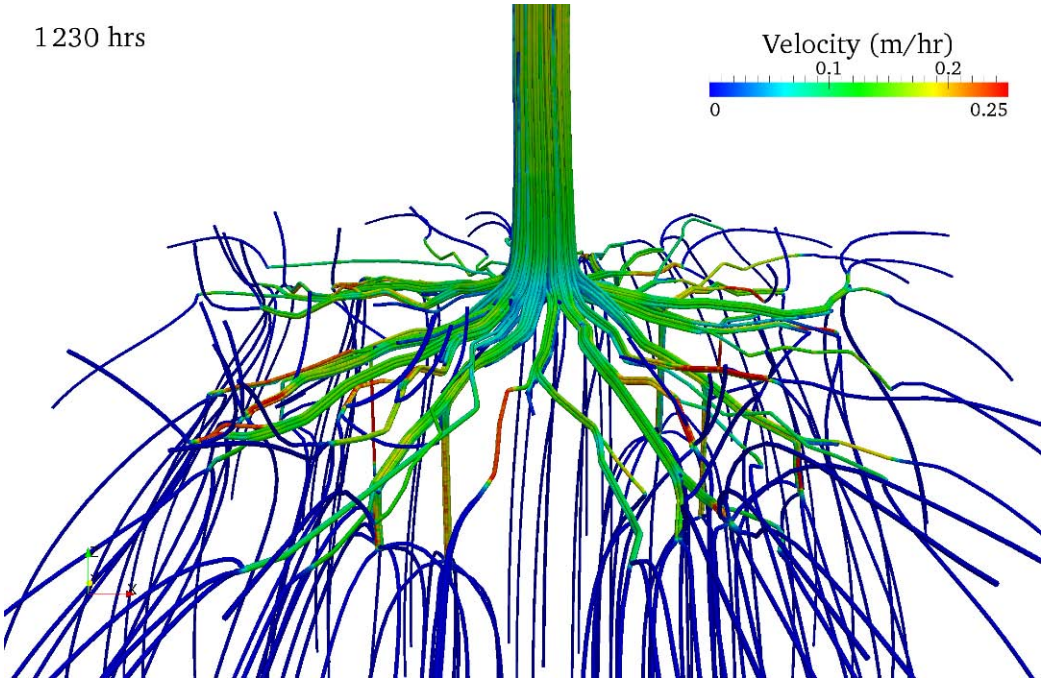


Figure 6.40 Fluid flow lines and velocity for saturated soil conditions 1230 hrs, 2 May 2010 for simulation Echo

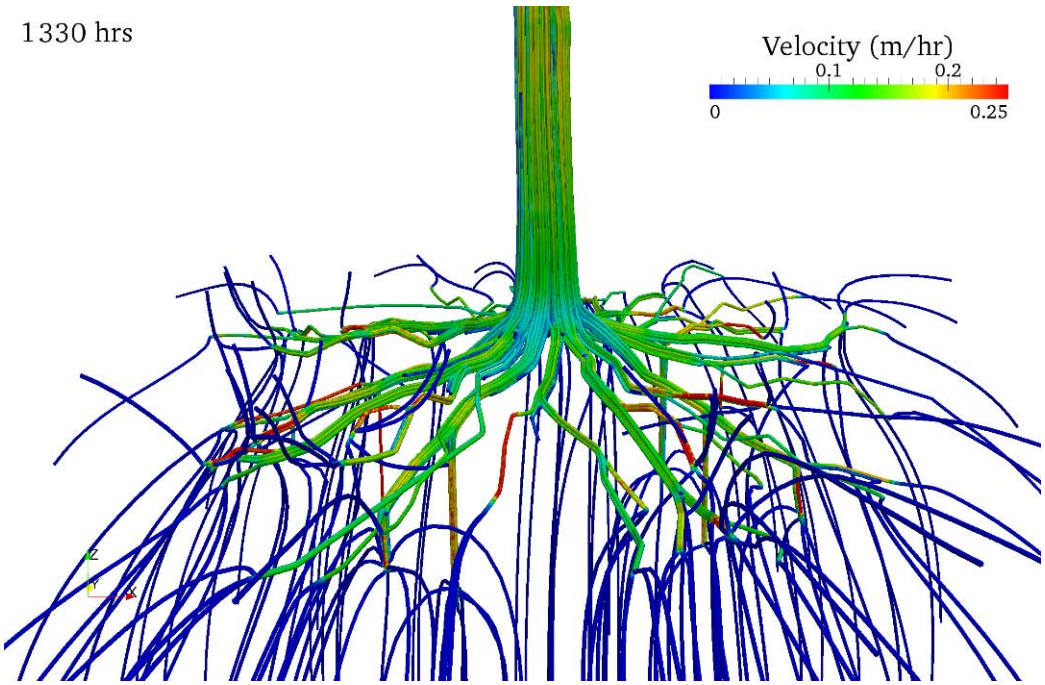


Figure 6.41 Fluid flow lines and velocity for saturated soil conditions 1330 hrs, 2 May 2010 for simulation Echo

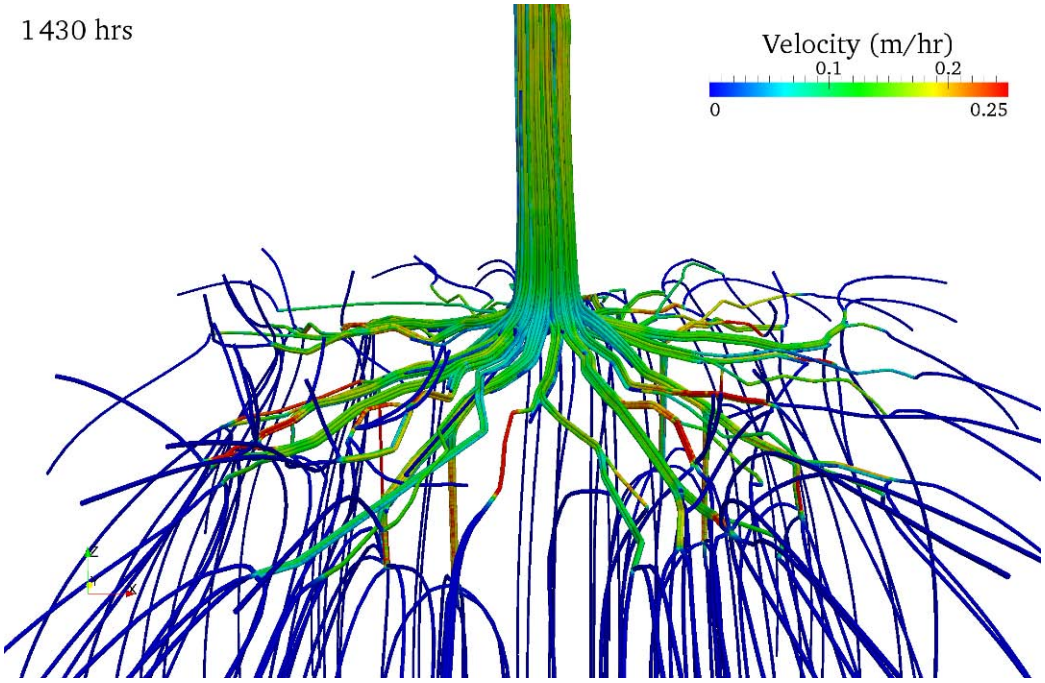


Figure 6.42 Fluid flow lines and velocity for saturated soil conditions 1430 hrs, 2 May 2010 for simulation Echo

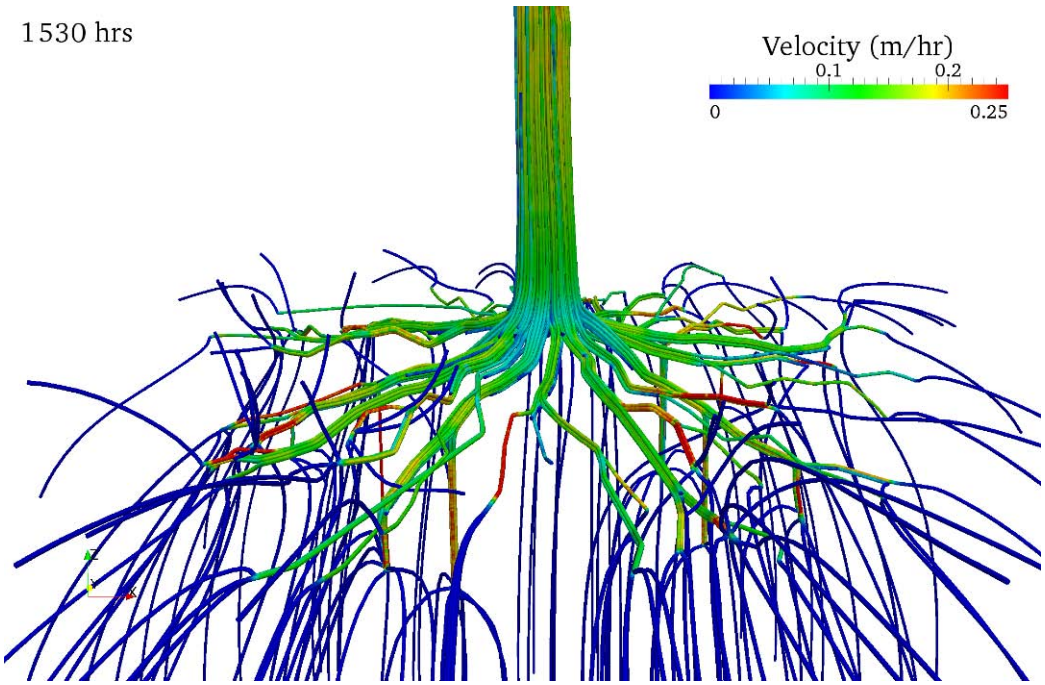


Figure 6.43 Fluid flow lines and velocity for saturated soil conditions 1530 hrs, 2 May 2010 for simulation Echo

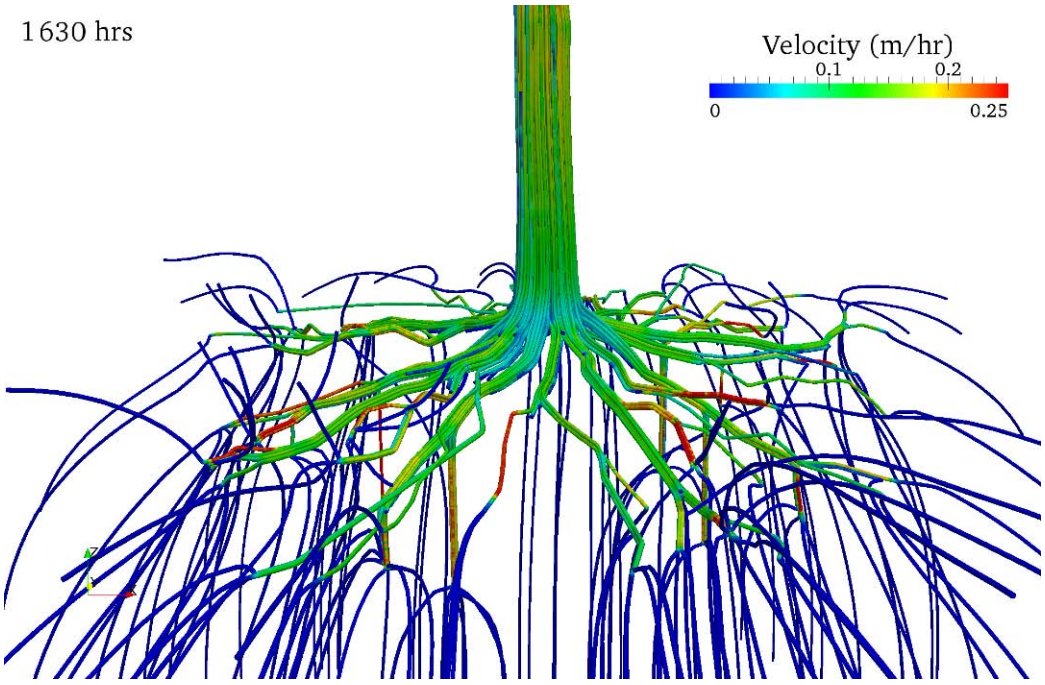


Figure 6.44 Fluid flow lines and velocity for saturated soil conditions 1630 hrs, 2 May 2010 for simulation Echo

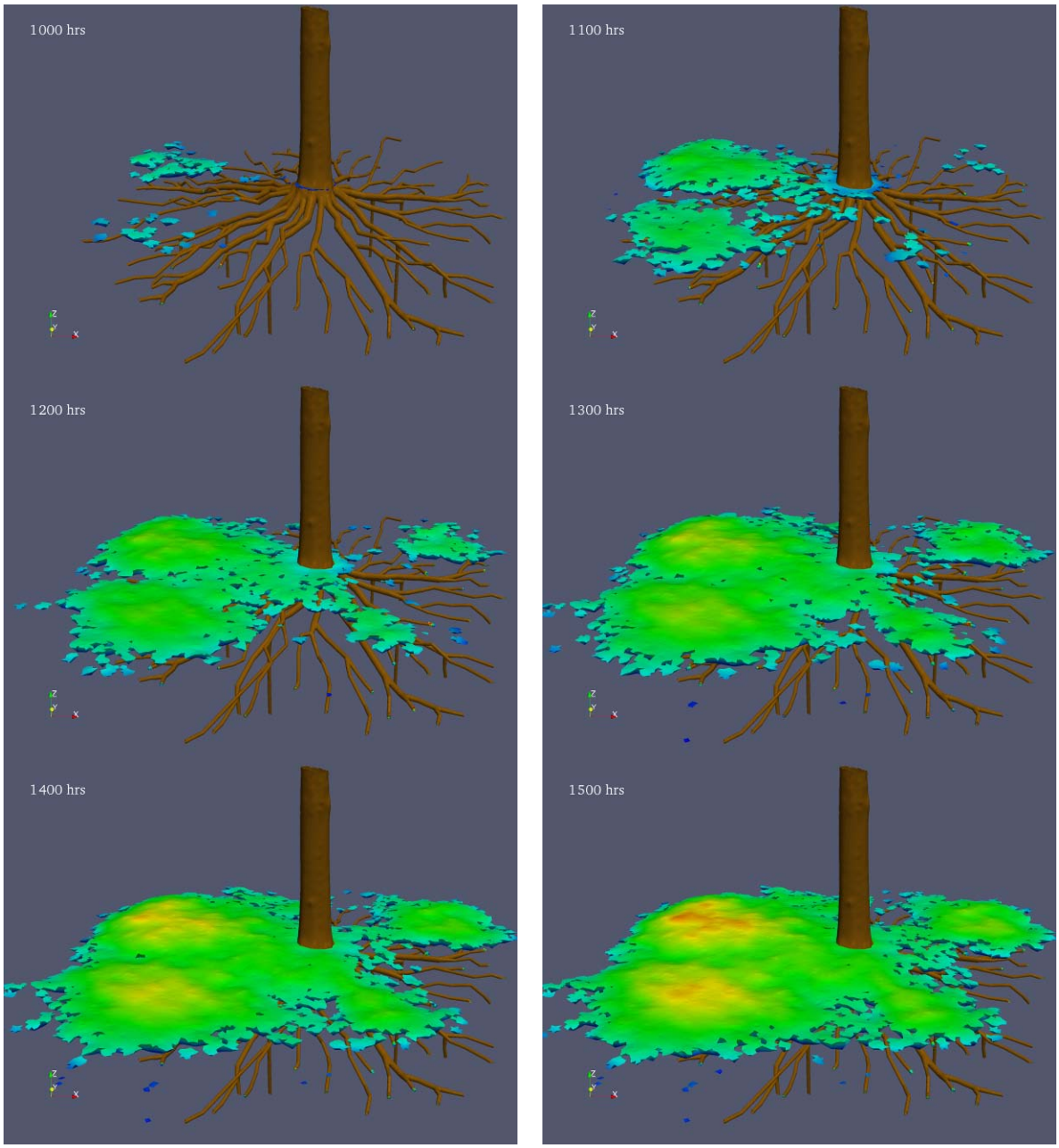


Figure 6.45 SRSS results of the development of unsaturated soil area indicated by a negative pressure head from 1000 – 1500 hrs, 2 May 2010 for simulation Echo.

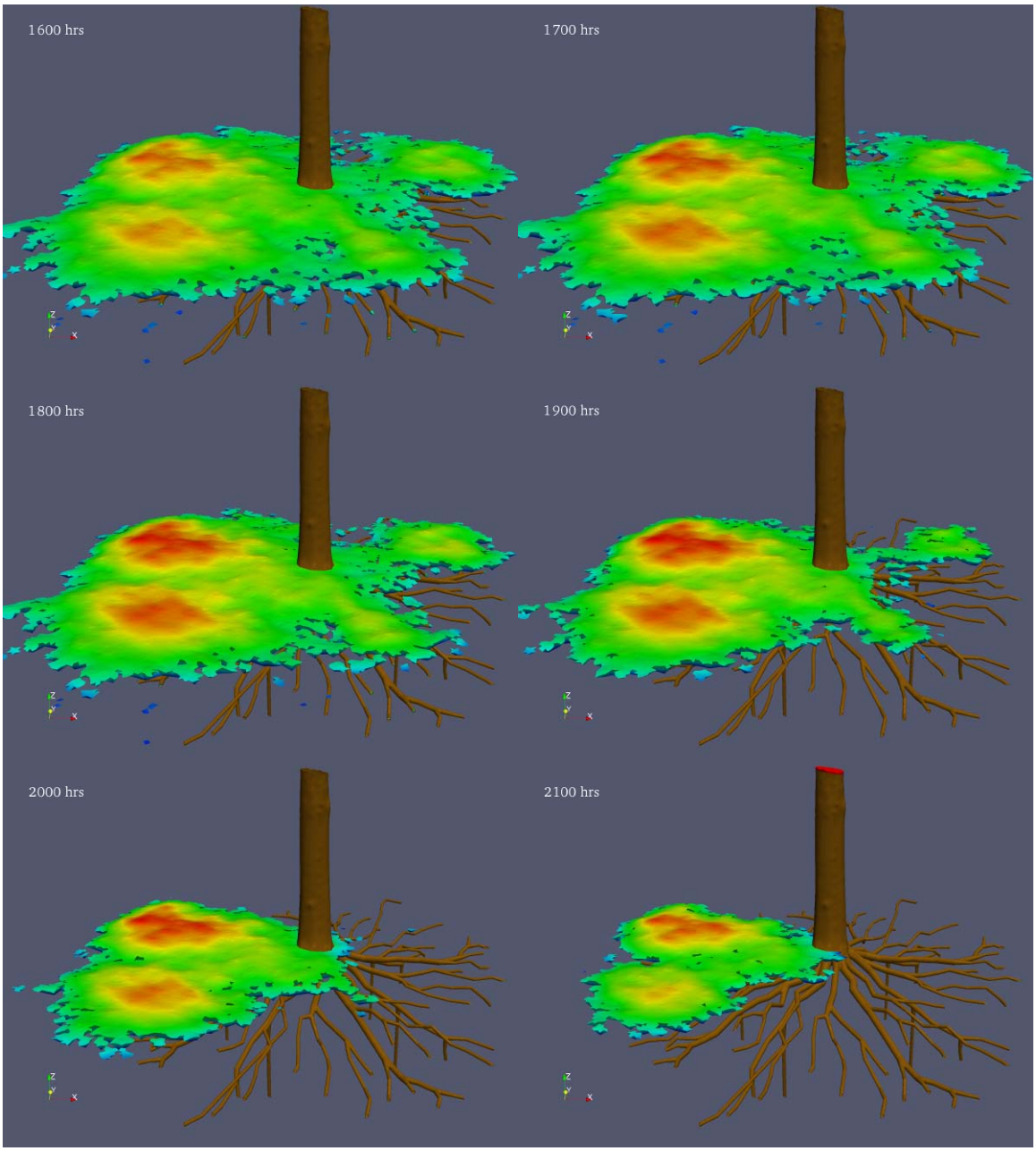


Figure 6.46 SRSS results of the development of unsaturated soil area from 1600-2100 hrs, 2 May 2010 for simulation Echo

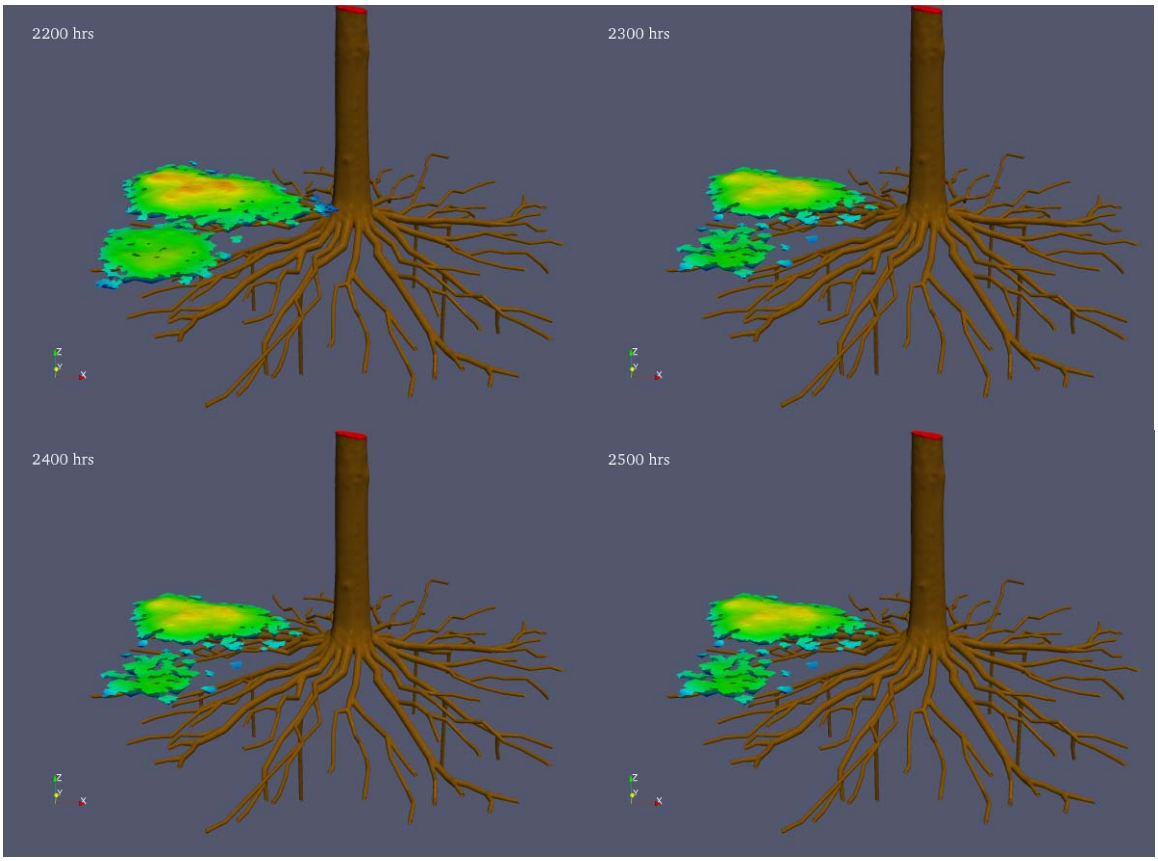


Figure 6.47 SRSS results of the development of unsaturated soil area from 2200-2500 hrs, 2-3 May 2010 for simulation Echo

### 6.4.3 Tree Trunk Early Summer Temperature History

Figures 6.48 – 6.51 present the temperature history of the trunk at a height of 0.6-m above the ground for both flow (simulation Echo) and no-flow (simulation Charlie) early summer conditions in a saturated soil. Similar to the discussion in Section 6.3.2, the temperatures presented in these figures are from nodal temperatures in the mesh along the cardinal axis radius from the trunk surface towards the center of the trunk (Figure 6.21). Temperatures of the north radius (Figure 6.48) are similar to the simulated temperatures of the east radius (Figure 6.49) except for the times between 1130 – 1500 hrs at depths shallower than 0.06-m when the temperatures along the east radius are 0.5

deg C warmer. In contrast, the temperature history of the south and west radii are slightly different, specifically around 1500 hrs when a gap in the forest canopy increases the solar illumination on the west side of the trunk (Figure 6.33, 1500 hrs). The effect of this illumination and subsequent heating of the surfaces is evident in the temperature spike at 1500 hrs on the west radius at a depth of 0.06-m (Figure 6.51). A time history of the temperature differences (north – south and east - west) are detailed in Figure 6.52 and Figure 6.53. In all these cases, the temperature differences are considered small (less than 1 deg C), a result of the dense canopy blocking the majority of the direct short-wave solar radiation.

Next the temperature history is examined for the same cardinal directions in the trunk at the same height, but for this case the fluid flow is stopped. All boundary conditions are kept the same for the no flow simulations except that no flow occurs during the day. Comparing the results of the no flow simulations along the same axis to the flow conditions, significant temperature differences are observed. Figure 6.54 - Figure 6.57 provide the difference history plots of the temperatures along the cardinal axis subtracting the no flow temperature (simulation Charlie) from the flow temperature (simulation Echo). In Figure 6.54, from the beginning of the flow at 0800 hrs, by 1200 hrs an increase in temperature of more than 1 deg C occurs in the flow conditions than in the no-flow conditions. This trend continues up to 1700 hrs, when the flow rate starts diminishing. The majority of the heating occurs from 0.03 – 0.05-m in the trunk, which is the same distance from the surface as the maximum velocity in the sap wood (Figure 6.35). Fifteen hours later (Figures 6.54 – 6.57), the temperature difference in the flow region of the trunk is reduced to near 1 deg C. As this diurnal trend continues, the center of the trunk is warmed to near the same temperature as the soil at roughly a 0.5-m depth

below ground surface. Along all four axes, this significant warming of the trunk is occurring.

The results for temperatures at three different heights along the south axis are shown in Figure 6.58 and Figure 6.59. Figure 6.58 for flow reveals a general decrease in temperature the farther the point is from the ground. The results are similar for the no flow conditions (Figure 6.59) although overall the temperatures are cooler compared to the flow conditions. Figure 6.60 and Figure 6.61 further illustrates the decrease in temperature as a function of heights for the mesh nodes just within the bark surface. The temperatures also appear to continue to decrease over time out to 30 hrs in the simulation where the difference between the 0.3m and 1.3m is over 5 deg C. But vertically increasing the height to the 0.6m position, the difference is only approximately 3-4 deg C. Radiative heating from the soil is apparent in the 0.3m temperatures.

Lastly, the results for the open canopy (Foxtrot) simulation are compared with the full canopy (Echo) simulation. Both of these simulations include flow conditions, so any temperature differences observed can only be attributed to the shortwave and longwave changes. For Figures 6.62 – 6.65, the results of the temperature difference between the flow and open canopy simulations are provided for all four cardinal axes. In these figures, a negative temperature indicates that the open canopy simulation is warmer, and a positive temperature indicates that the full canopy simulation is warmer. The north and east radii show small differences, and all are less than 1 deg C. The south radius temperature differences are larger than the north and east, and most of the temperatures are negative indicating that the open canopy temperatures are warmer. The west radius temperature differences show the largest differences compared to the other radii directions. As shown in Figure 6.34 at 1700 hrs, these west radius temperature

differences are caused by continuous solar radiative heating for the open canopy (Foxtrot) simulation compared to the closed canopy (Echo) simulation. Ultimately, these solar radiation conditions simulated in the open canopy (Foxtrot) simulation show persistent warmer temperatures in the soil, and in the trunk.

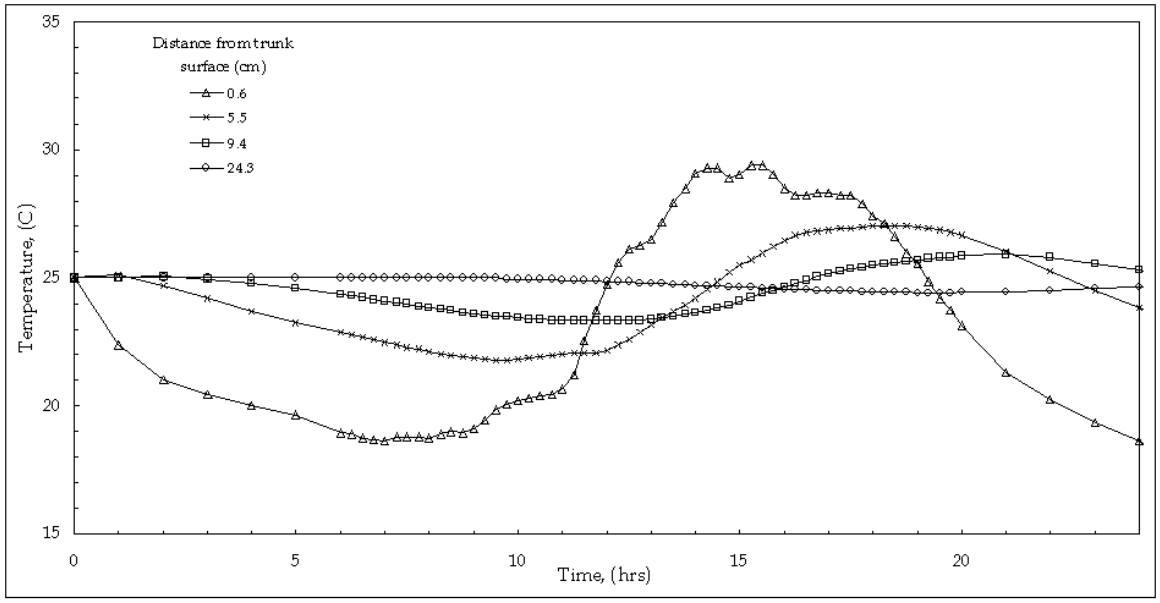


Figure 6.48 SRSS temperature history of the trunk at 0.6m along the north radius with flow for 2 May 2010 for simulations Charlie and Delta

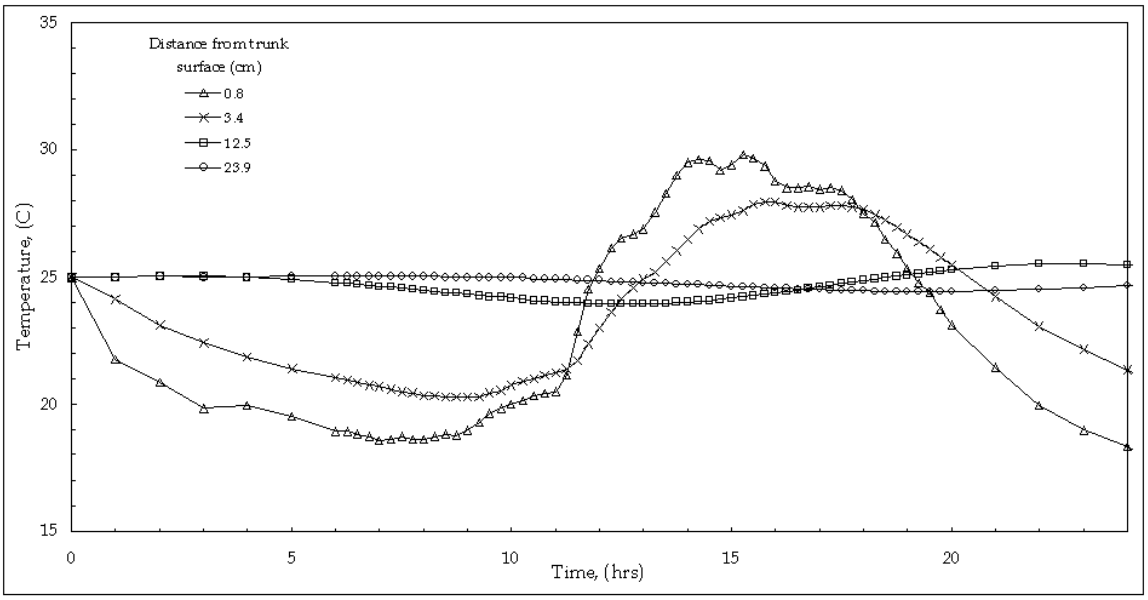


Figure 6.49 SRSS temperature history of the trunk at 0.6m along the east radius with flow for 2 May 2010 for simulations Charlie and Delta

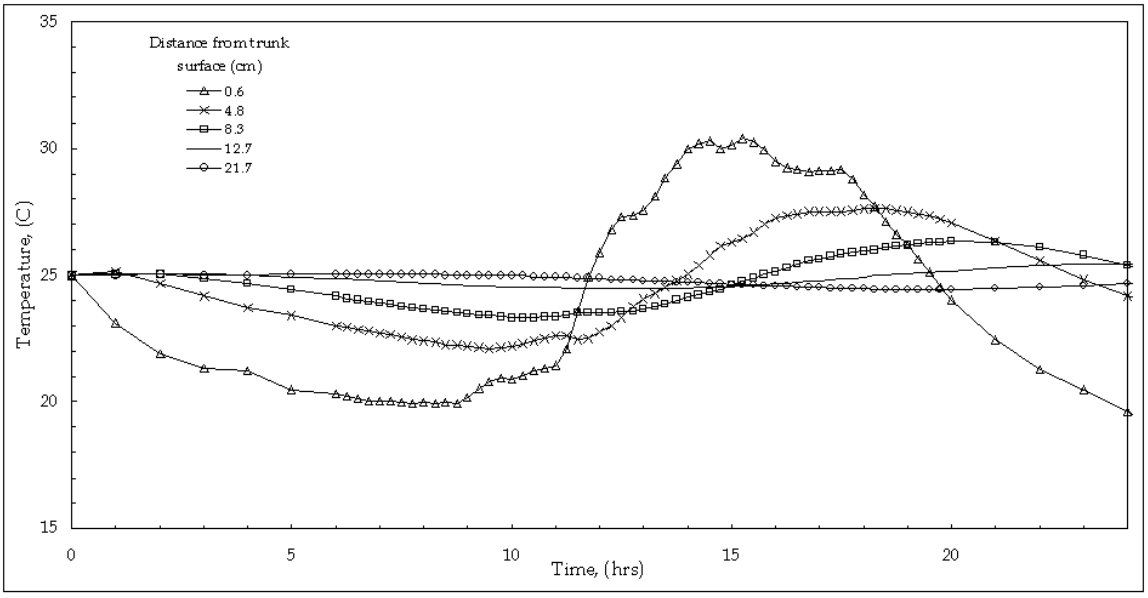


Figure 6.50 SRSS temperature history of the trunk at 0.6m along the south radius with flow for 2 May 2010 for simulations Charlie and Delta

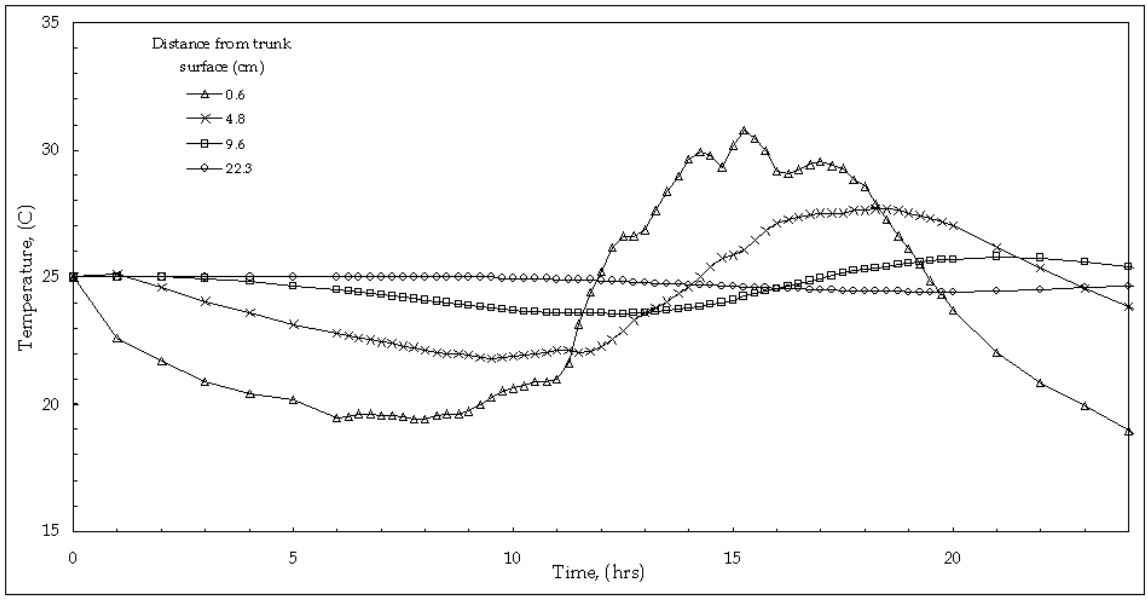


Figure 6.51 SRSS temperature history of the trunk at 0.6m along the west radius with flow for 2 May 2010 for simulations Charlie and Delta

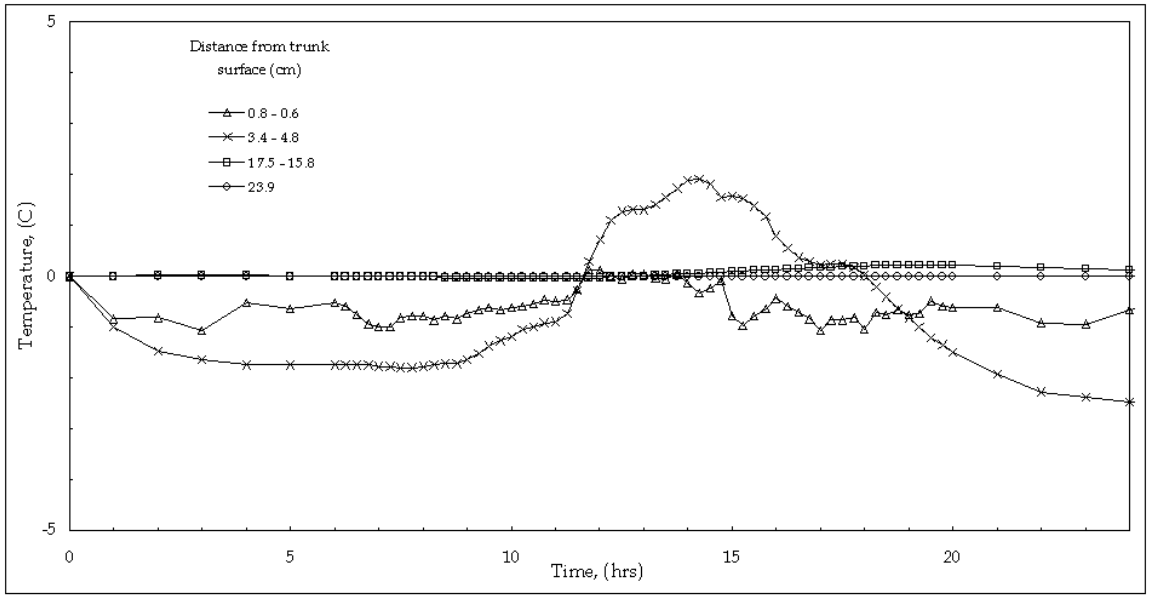


Figure 6.52 Temperature difference in the trunk at 0.6m between the east and west radius for 2 May 2010 for simulations Charlie and Delta

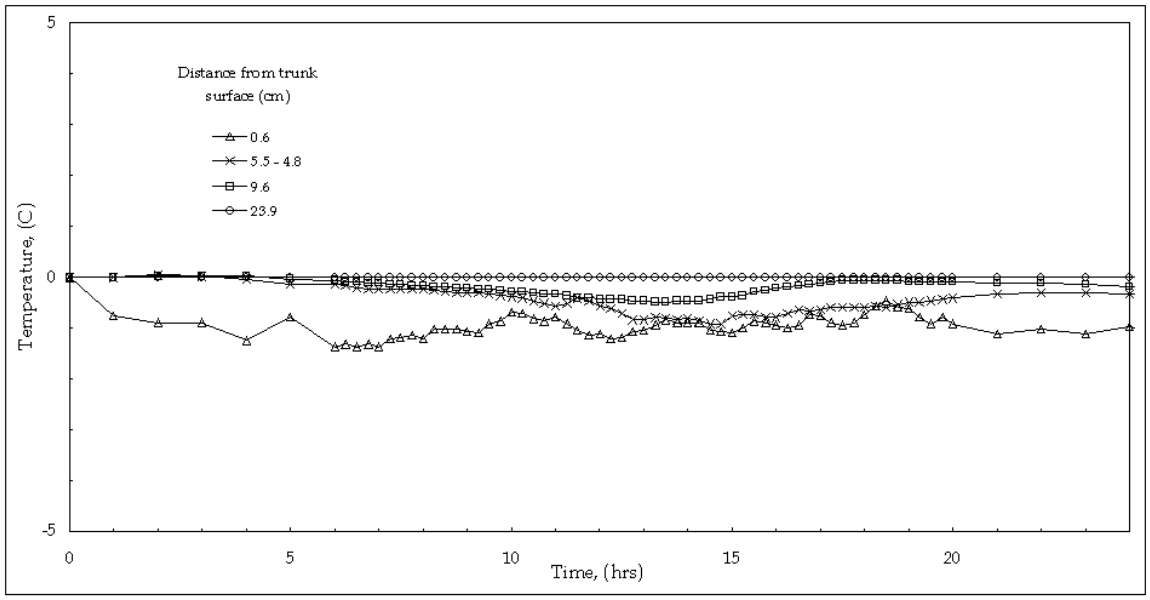


Figure 6.53 Temperatures difference in the trunk at 0.6m between the north and south radius for 2 May 2010 for simulations Charlie and Delta

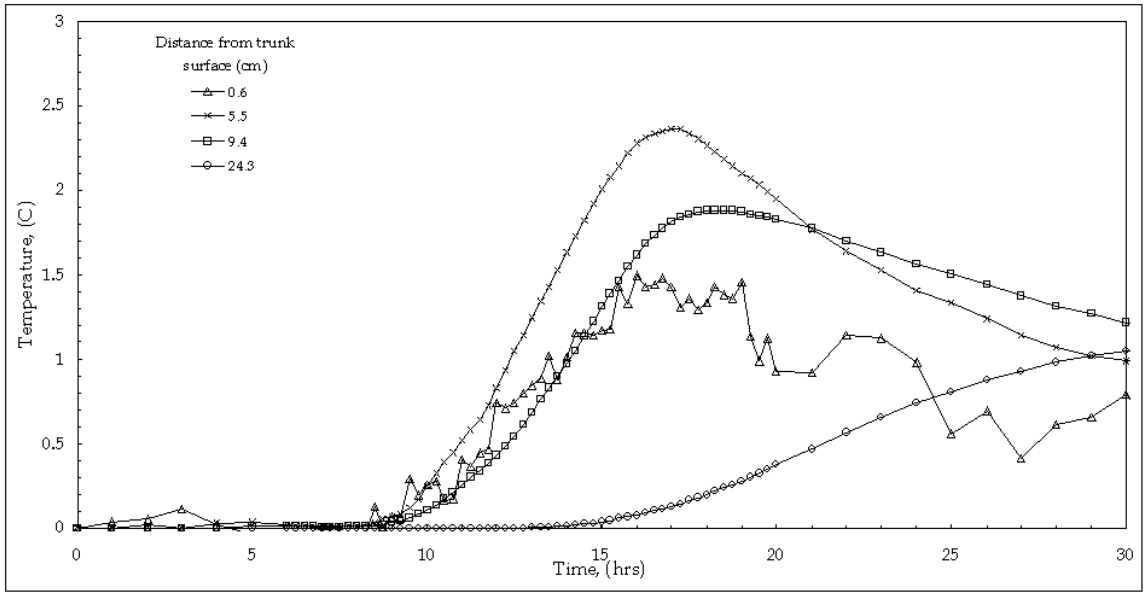


Figure 6.54 SRSS Temperature difference history between the flow (Echo) and no flow (Charlie) simulations along the north radius at 0.6m for 2 May 2010. (shown: flow – no flow)

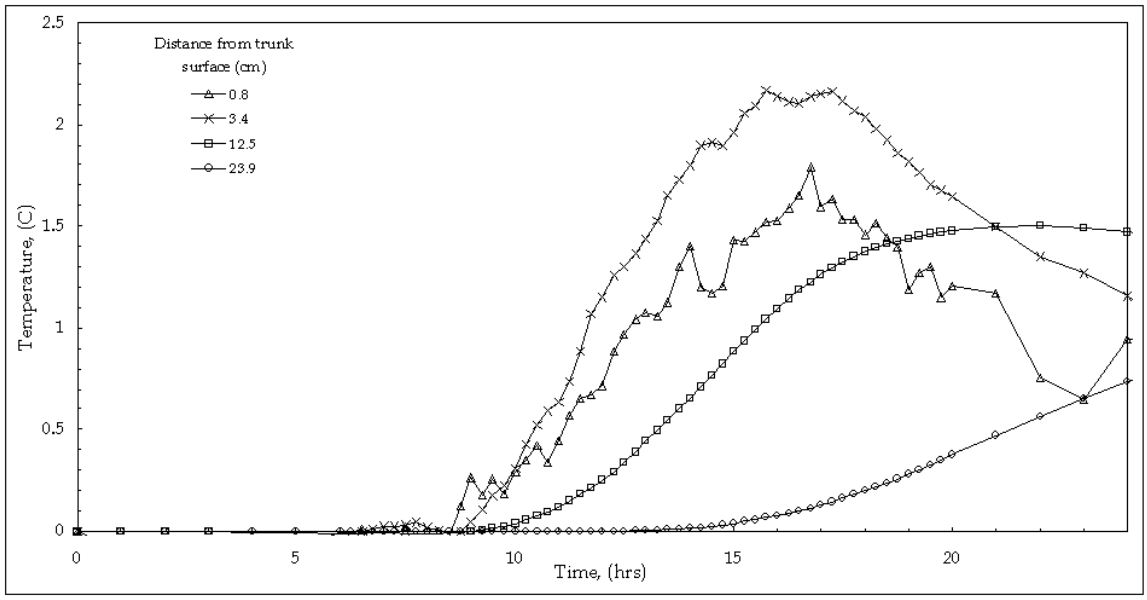


Figure 6.55 Temperature difference history between the flow (Echo) and no flow (Charlie) simulations along the east radius at 0.6m for 2 May 2010. (shown: flow – no flow)

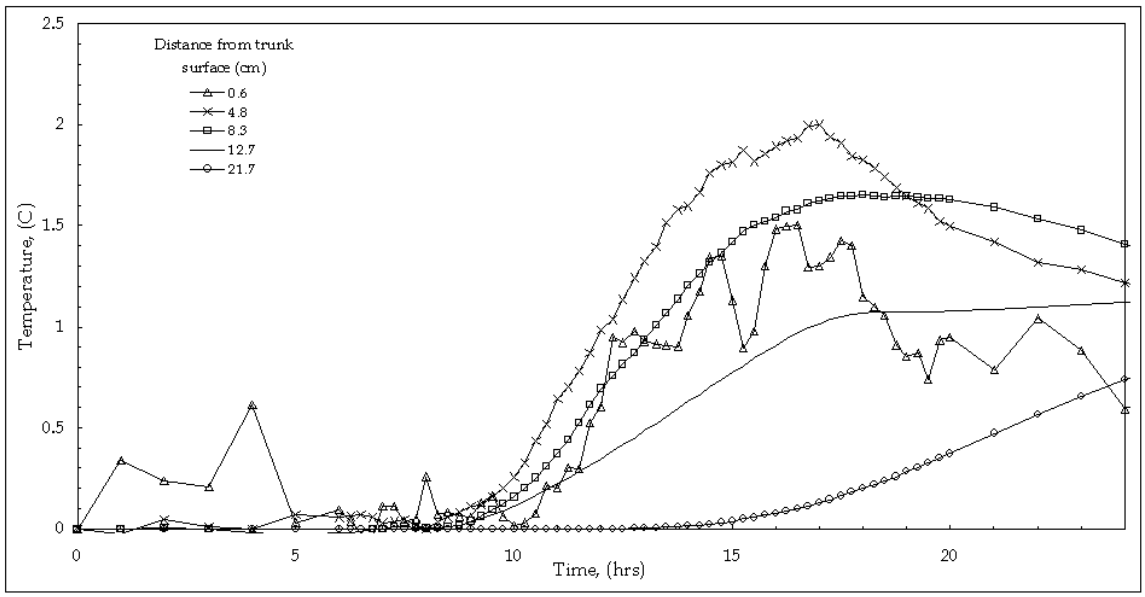


Figure 6.56 Temperature difference history between the flow (Echo) and no flow (Charlie) simulations along the south radius at 0.6m for 2 May 2010. (shown flow – no flow)

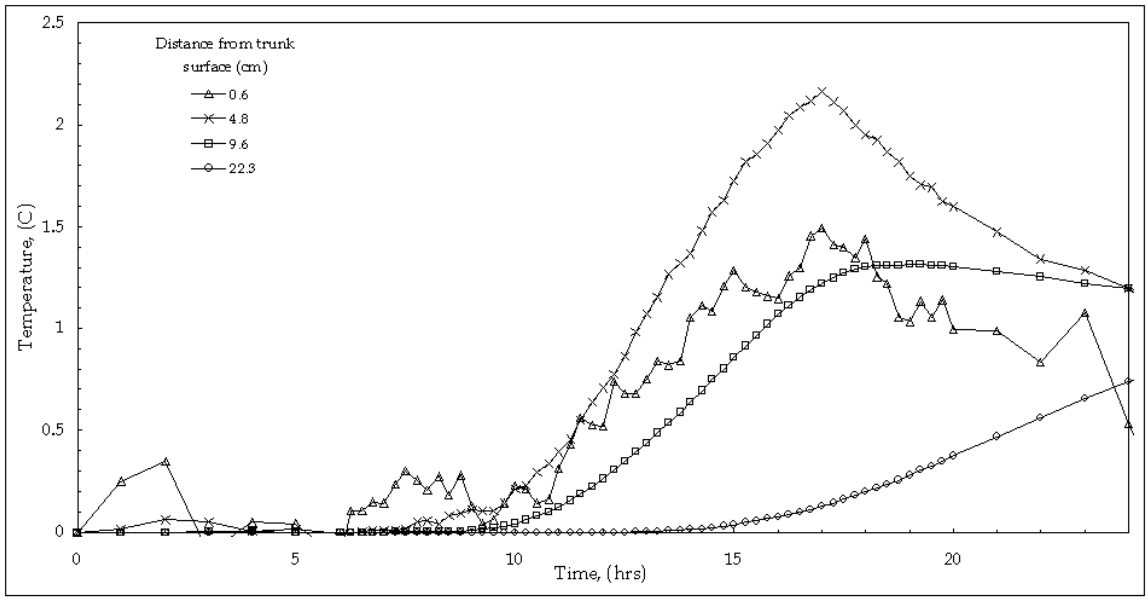


Figure 6.57 SRSS Temperature difference history between the flow (Echo) and no flow (Charlie) simulations along the west radius at 0.6m for 2 May 2010. (shown flow – no flow)

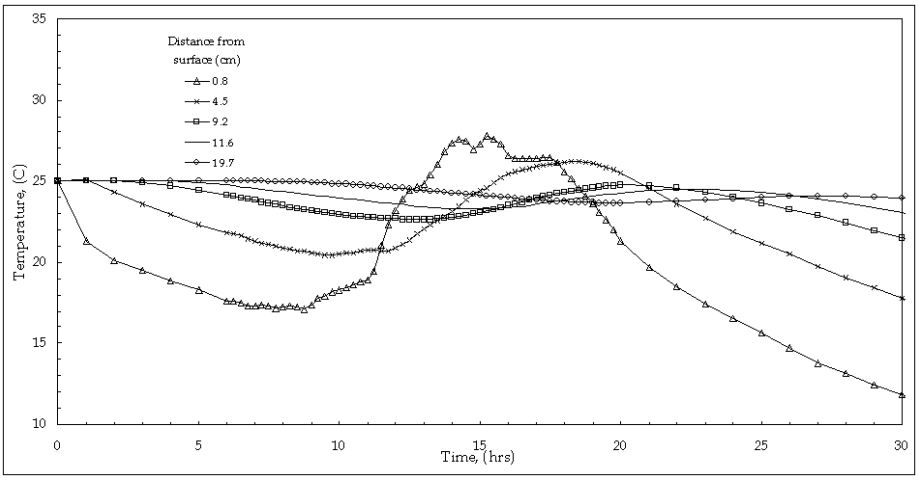


a) 1.3m

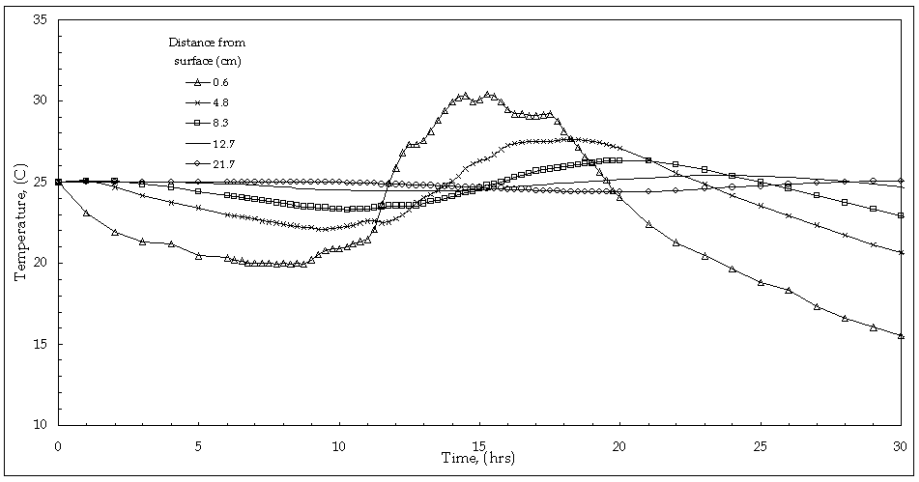


b) 0.6m

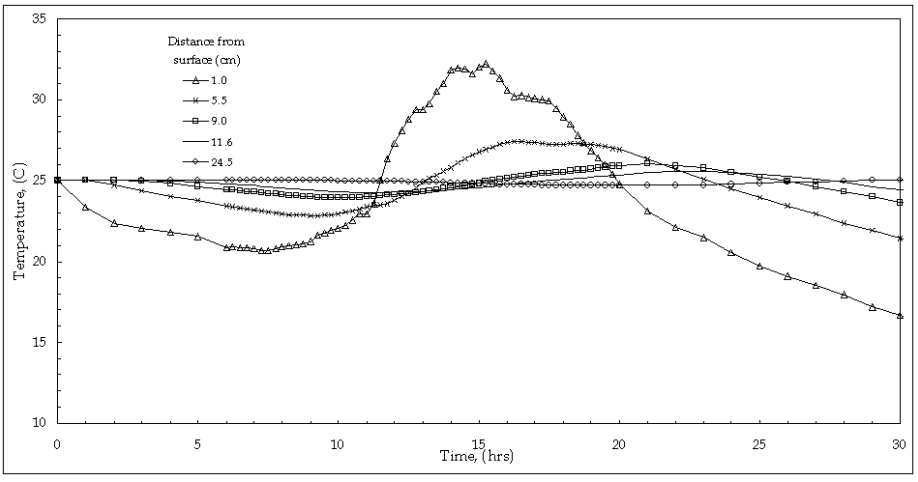


c) 0.3m

Figure 6.58 SRSS Temperature history of the trunk along the south radius at 1.3, 0.6, and 0.3m with fluid flow for 2 May 2010 for simulation Echo.

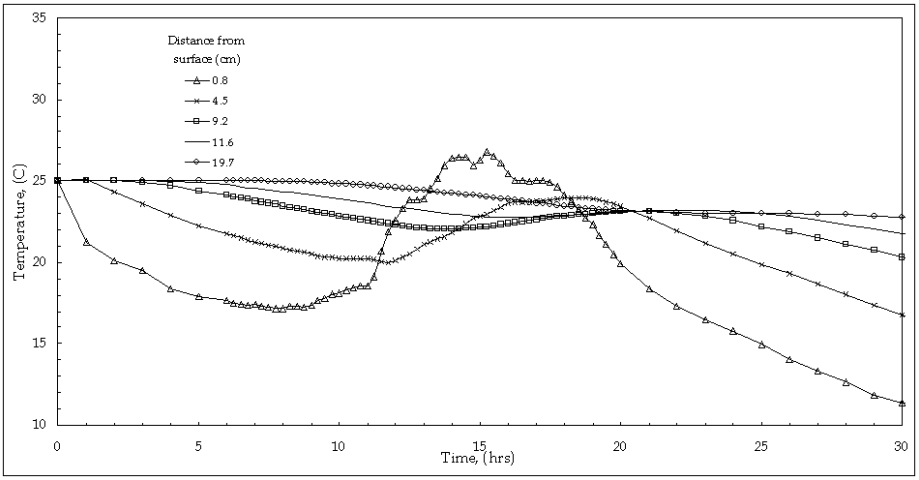


a) 1.3m

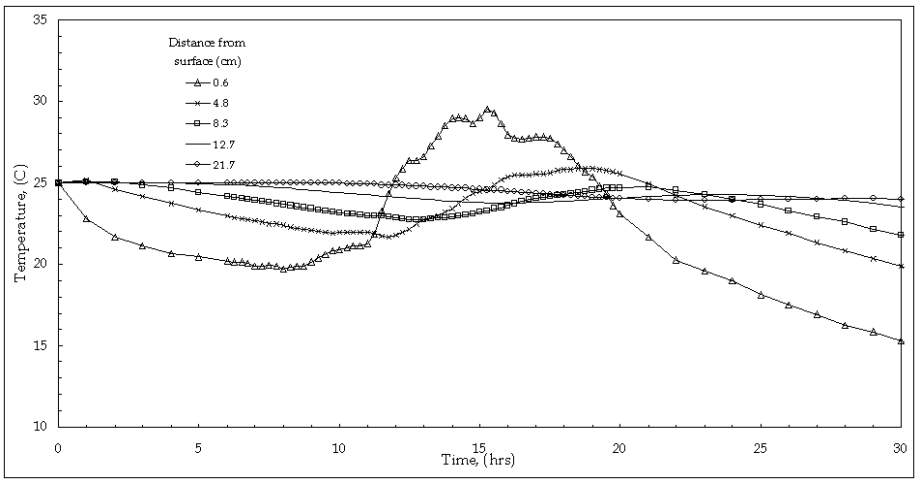


b) 0.6m

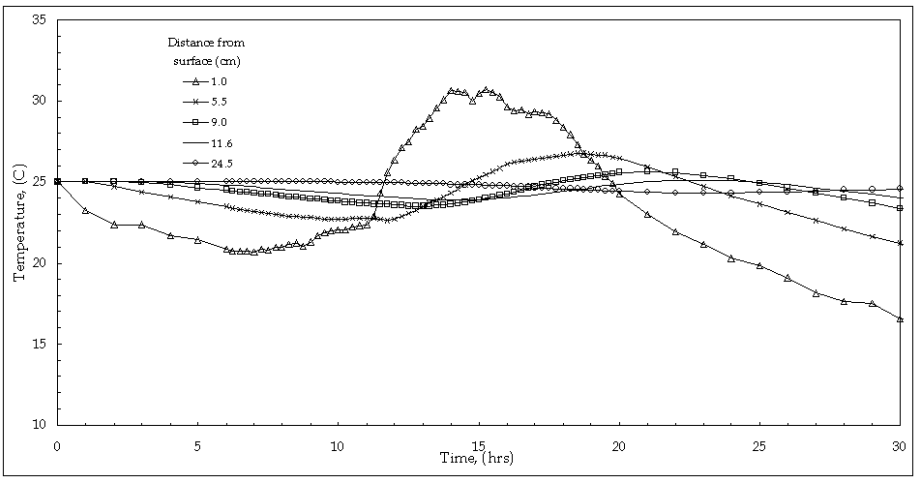


c) 0.3m

Figure 6.59 SRSS Temperature history of the trunk along the south radius at 1.3, 0.6, and 0.3m above the ground with no fluid flow for 2 May 2010 for simulation Charlie.

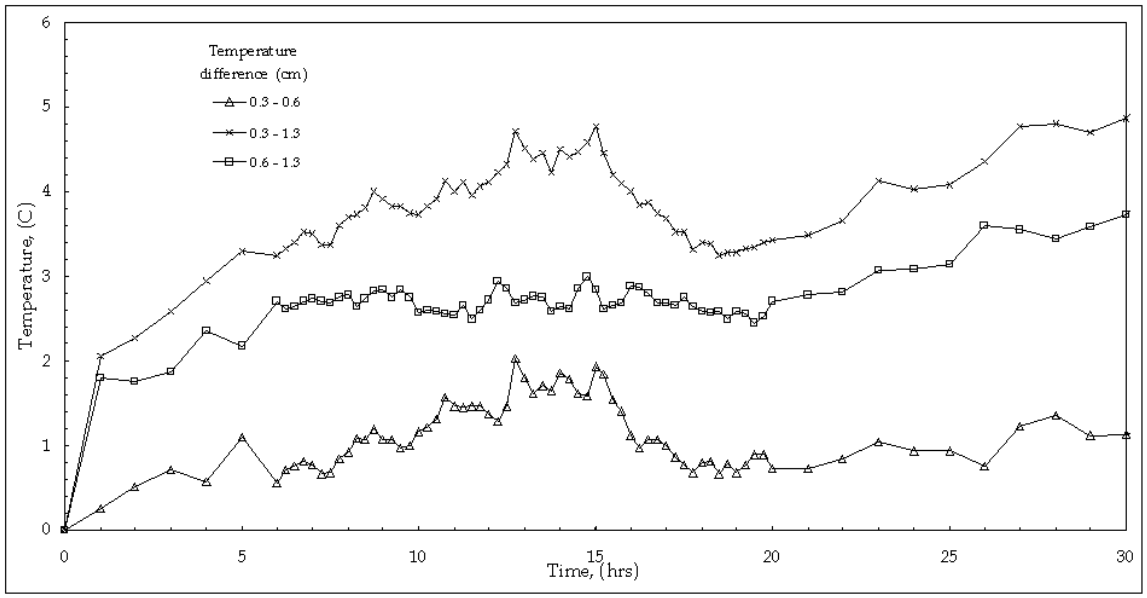


Figure 6.60 Temperature difference history between south radius temperatures at 1.3, 0.6, and 0.3m above the ground with fluid flow for 2 May 2010 (simulation Echo)

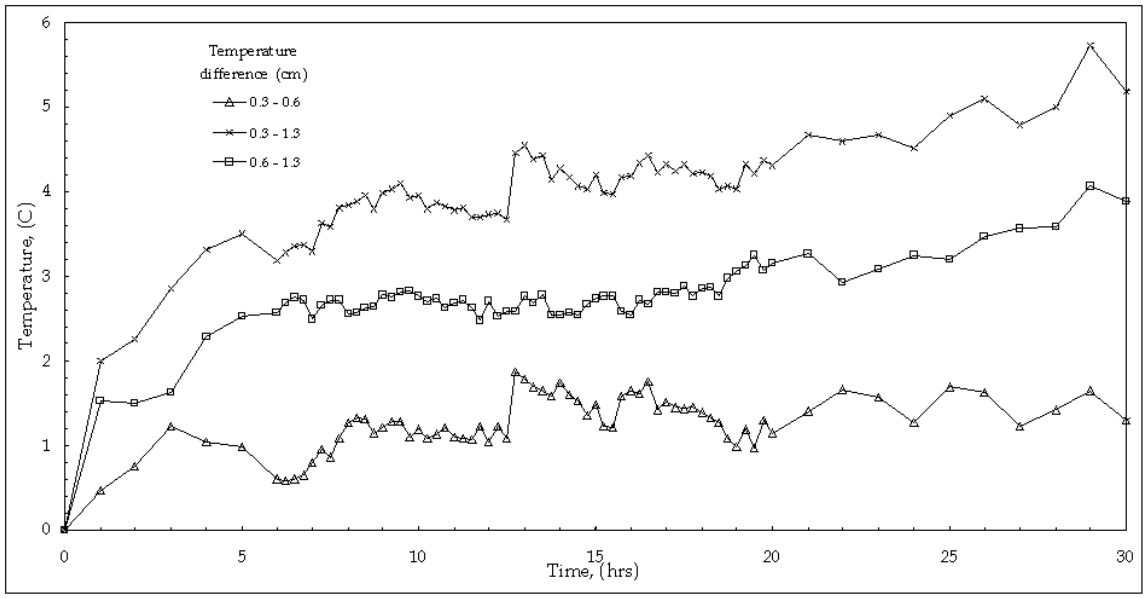


Figure 6.61 SRSS Temperature difference history between south radius temperatures at 1.3, 0.6, and 0.3m above the ground with no fluid flow for 2 May 2010 (simulation Charlie)

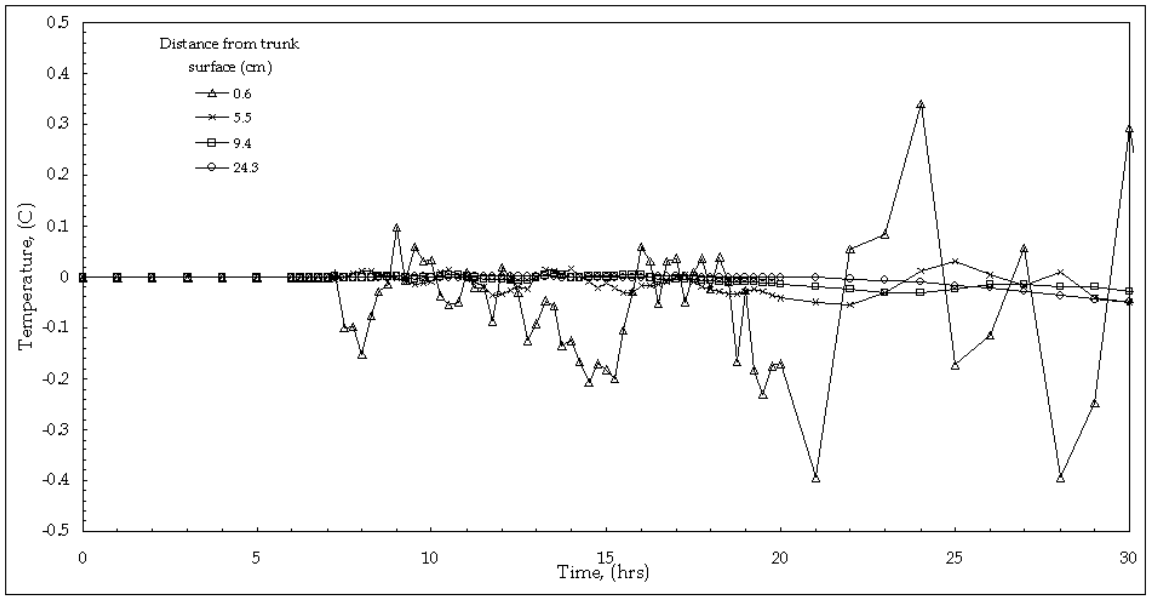


Figure 6.62 SRSS temperature difference history between the flow (Echo) and open canopy (Foxtrot) simulations along the north radius for 2 May 2010

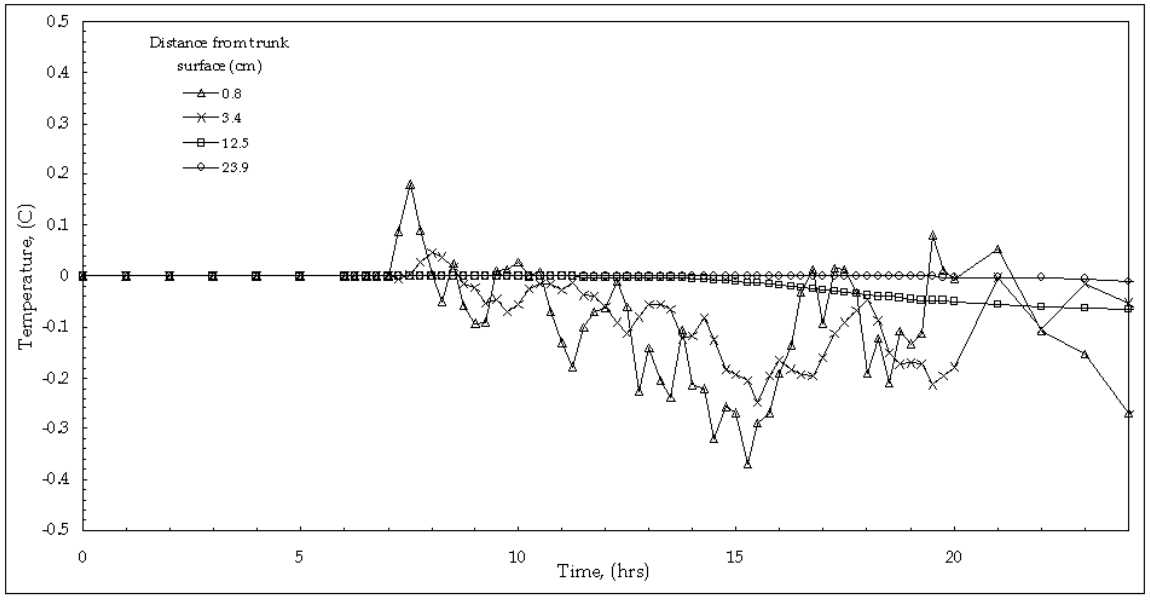


Figure 6.63 SRSS temperature difference history between the flow (Echo) and open canopy (Foxtrot) simulations along the east radius for 2 May 2010

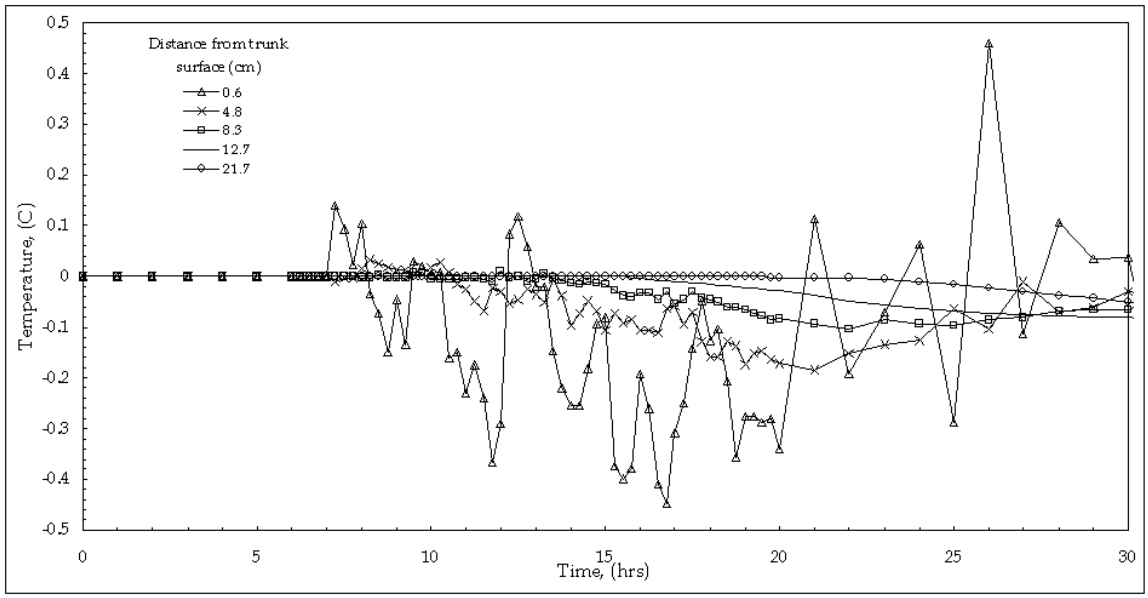


Figure 6.64 SRSS temperature difference history between the flow (Echo) and open canopy (Foxtrot) simulations along the south radius for 2 May 2010

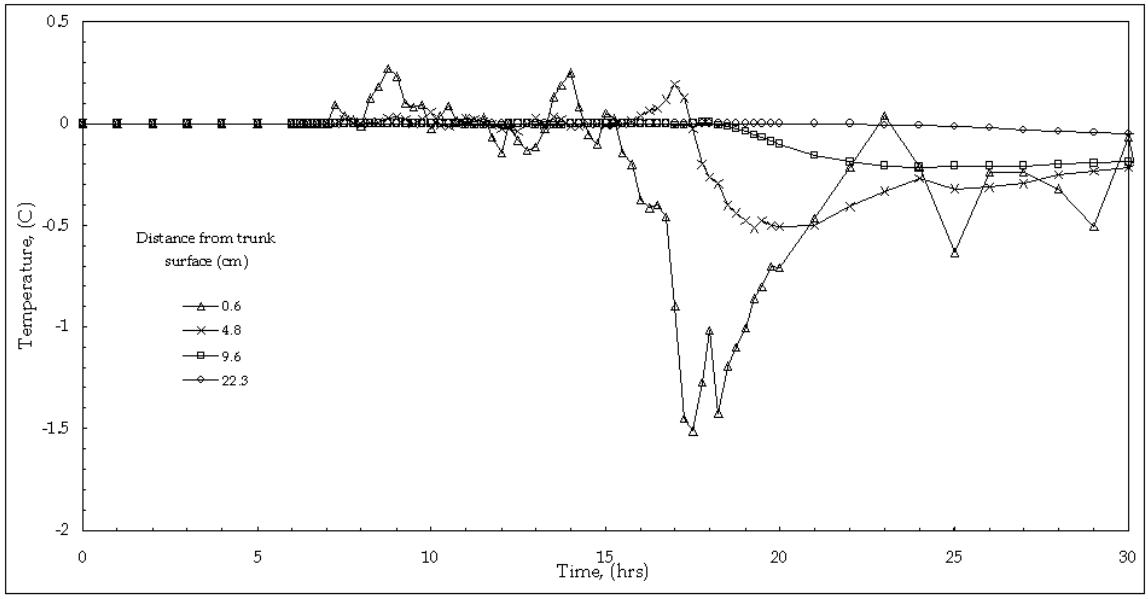


Figure 6.65 SRSS temperature difference history between the flow (Echo) and open canopy (Foxtrot) simulations along the west radius for 2 May 2010

## 6.5 Summary

This chapter describes the SRSS predictions of the thermal and hydraulic behavior of a tree in a deciduous forest during winter and early summer seasons. Results from the winter simulations indicate that the primary influence of temperature in the trunk is solar radiation and radiative energy from the soil and surrounding trees. Diurnal temperature ranges of 17 deg C were observed on the south axis of the trunk contrasted with temperatures ranges of 7 deg C on the north axis of the trunk. Results from the summer simulations differed from previous results indicating that the flow of fluid in the trunk was the primary influence of temperature change with secondary effects attributed to the radiative energy from the soil. Comparing flow and no flow simulations in the summer, the SRSS showed up to a 2 deg C internal wood temperature difference for a 0.3 m/hr flow rate. Other early summer simulation results show that with sap flow, as the soil around the roots became unsaturated, the flow path for the roots was changed to areas where the soil was still saturated, and also the velocity in those root areas increased.

# CHAPTER VII

# SUMMARY AND FUTURE WORK

This document described the development of a three-dimensional computational tool that simulates the radiative energy, conductive heat, and mass transfer interaction in a soil-root-stem system (SRSS). The completion of the SRSS required the development of a Monte-Carlo radiative transfer code (MCRT), modification of a ground water flow code, and verification of the individual components of the simulation. The end result is the creation of a tool that was shown to predict the three-dimensional diurnal, internal and external temperatures, internal fluid distribution, and heat flow in the soil, roots, and trunk in a seasonally varying deciduous forest. The individual components of the SRSS were validated with analytical solutions, and the composite results of the SRSS were compared with published measured and simulation studies.

The development and addition of the Monte-Carlo radiative transfer code combined with a hemispherical mapping of the surrounding trees and foliage was sufficiently accurate to simulate the entire spectrum of radiative effects of the surrounding forest without explicit modeling of the entire forest. Simulations during the early summer (May 2010) indicated that, in the presence of low to moderate sap flow velocities (0.3 m/hr), the internal temperatures of the stem can vary as much as 2.5 deg C at 0.6 m above the ground surface when compared with the same conditions during no flow. The magnitudes of the internal stem temperature differences are correlated to the current soil temperature at depth and are small when compared to radiative fluxes.

Winter simulations (Jan 2009) of the SRSS indicate that incident solar radiation on the trunk results in dramatically larger observed temperature ranges than those found during the early summer simulations. These simulation results are consistent with observations.

The root system and subsequent uptake of fluid from the soil were shown in simulation to develop an unsaturated soil region. This soil region had a distinct development, starting at the surface of the soil and gradually growing down into the soil, and expanded continually while the uptake occurred. Recovery from the unsaturated soil region back to saturated conditions during the evening was slow, and the rate depended on the hydraulic conductivity of the soil media. The change from saturated to unsaturated soil altered the thermal properties of the soil and consequently exhibited differing temperature histories. It is observed that as areas of unsaturated soil developed, the soil hydraulic conductivity decreased, and fluid demand was increased to those roots in areas of saturated soil. The change in fluid demand also increased the fluid velocity in the same roots.

There exist several main areas for future work with the SRSS: inclusion of dense vegetation in the simulation, long-term full season studies, drought simulations, and additional validation studies using experimental studies. Inclusion and simulation of dense understory surface vegetation on the surface and around the tree will alter the external thermal and radiative energy budget of the system. It is unclear if the surrounding foliage significantly affects the internal temperature of the stem. For the area of long-term full season simulations, a simulation from early summer to late summer would be required to fully examine the growth and extent of the unsaturated soil zone around the tree and subsequent effects on moisture uptake by the system. As the SRSS is presently configured, this long-term simulation would require significant computational

resources (90 simulated days = ~60M CPU hours) mainly dedicated to the Monte-Carlo radiative transfer code. For this particular type of simulation, the thermal radiative transfer calculations could be simplified, reducing the computational requirements down to a reasonable level. Simulation of a drought or prolonged periods of little rainfall is one of the other areas of future study that pose a computational challenge. During a drought as the soil saturation decreases, the pressure required to extract moisture from the soil increases exponentially (see Figure 6.9 as an example) causing steep pressure gradients between the root tips and the soil. Solving these steep pressure gradients can cause numerical instability. Data and studies addressing these pressure gradients during unsaturated soil conditions are rare. Additionally, simulation studies are required to determine if the steep pressure gradients are caused by the macroscale modeling of a microscale event. Finally, more validation studies using experimental and measured data are required to improve the confidence in the SRSS results. Above-ground measurements (sap velocity, surface radiation distribution, solar radiation energy budgets, and stem temperatures) are expensive but readily obtainable. Subsurface measurement methods such as nondestructive temporal and spatial measurement of soil moisture content under and around the root system are extremely difficult to obtain. Consequently, full validation of the SRSS subsurface processes may have to wait until the measurement technology improves.

# REFERENCES


[1] R. K. Dixon, A. M. Solomon, S. Brown, R. A. Houghton, M. C. Trexier and J. Wisniewski, "Carbon Pools and Flux of Global Forest Ecosystems," *Science*, 263, no. 5144, 1994, pp. 185-190.

[2] T. J. Griffis, T. A. Black, D. Gaumont-Guay, G. B. Drewitt, Z. Nesic, A. G. Barr, K. Morgenstern and N. Kljun, "Seasonal Variation and Partitioning of Ecosystem Respiration in a Southern Boreal Aspen Forest," *Agricultural and Forest Meteorology*, 125, no. 3-4, 2004, pp. 207-223.

[3] J.-A. Subke and J. D. Tenhunen, "Direct Measurements of Co2 Flux Below a Spruce Forest Canopy," *Agricultural and Forest Meteorology*, 126, no. 1-2, 2004, pp. 157-168.

[4] M. Kondo, H. Muraoka, M. Uchida, Y. Yazaki and H. Koizumi, "Refixation of Respired Co2 by Understory Vegetation in a Cool-Temperate Deciduous Forest in Japan," *Agricultural and Forest Meteorology*, 134, no. 1-4, 2005, pp. 110-121.

[5] B. D. Amiro, A. G. Barr, T. A. Black, H. Iwashita, N. Kljun, J. H. McCaughey, K. Morgenstern, S. Murayama, Z. Nesic, A. L. Orchansky and N. Saigusa, "Carbon, Energy and Water Fluxes at Mature and Disturbed Forest Sites, Saskatchewan, Canada," *Agricultural and Forest Meteorology*, 136, no. 3-4, 2006, pp. 237-251.

[6] D.-X. Guan, J.-B. Wu, X.-S. Zhao, S.-J. Han, G.-R. Yu, X.-M. Sun and C.-J. Jin, "Co2 Fluxes over an Old, Temperate Mixed Forest in Northeastern China," *Agricultural and Forest Meteorology*, 137, no. 3-4, 2006, pp. 138-149.

[7] J. H. McCaughey, M. R. Pejam, M. A. Arain and D. A. Cameron, "Carbon Dioxide and Energy Fluxes from a Boreal Mixedwood Forest Ecosystem in Ontario, Canada," *Agricultural and Forest Meteorology*, 140, no. 1-4, 2006, pp. 79-96.

[8] C. J. Moore and G. Fisch, "Estimating Heat Storage in Amazonian Tropical Forest," *Agricultural and Forest Meteorology*, 38, no. 1-3, 1986, pp. 147-168.

[9] C. A. Federer, "Solar Radiation Absorption by Leafless Hardwood Forests," *Agricultural Meteorology*, 9, 1971, pp. 3-20.

[10] D. D. Baldocchi, D. R. Matt, B. A. Hutchison and R. T. McMillen, "Solar Radiation within an Oak--Hickory Forest: An Evaluation of the Extinction Coefficients for Several Radiation Components During Fully-Leafed and Leafless Periods," *Agricultural and Forest Meteorology*, 32, no. 3-4, 1984, pp. 307-322.

[11] G. B. Bonan, D. Pollard and S. L. Thompson, "Effects of Boreal Forest Vegetation on Global Climate," *Nature*, 359, no. 6397, 1992, pp. 716-718.

[12] P. J. Crutzen and M. O. Andreae, "Biomass Burning in the Tropics: Impact on Atmospheric Chemistry and Biogeochemical Cycles," *Science*, 250, no. 4988, 1990, pp. 1669-1678.

[13] M. Génard, J. Dauzat, N. Franck, F. Lescourret, N. Moitrier, P. Vaast and G. Vercambre, "Carbon Allocation in Fruit Trees: From Theory to Modelling," *Trees - Structure and Function*, 2008,

[14] C. P. A. Bourque, P. A. Arp, R. B. B. Dickison and R. E. Mickle, "Destabilization of the Lower Atmosphere above a Forest: A Model," *Agricultural and Forest Meteorology*, 47, no. 1, 1989, pp. 49-74.

[15] K. T. Paw U, Y. Brunet, S. Collineau, R. H. Shaw, T. Maitani, J. Qiu and L. Hipps, "On Coherent Structures in Turbulence above and within Agricultural Plant Canopies," *Agricultural and Forest Meteorology*, 61, no. 1-2, 1992, pp. 55-68.

[16] M. Mölder and A. Lindroth, "Thermal Roughness Length of a Boreal Forest," *Agricultural and Forest Meteorology*, 98-99, 1999, pp. 659-670.

[17] A. Venäläinen, H. Zeng, H. Peltola, A. Talkkari, H. Strandman, K. Wang and S. Kellomäki, "Simulations of the Influence of Forest Management on Wind Climate on a Regional Scale," *Agricultural and Forest Meteorology*, 123, no. 3-4, 2004, pp. 149-158.

[18] Y. Ouyang, "Phytoremediation: Modeling Plant Uptake and Contaminant Transport in the Soil-Plant-Atmosphere Continuum," *Journal of Hydrology*, 266, no. 1-2, 2002, pp. 66-82.

[19] Y. Ouyang, "Phytoextraction: Simulating Uptake and Translocation of Arsenic in a Soil-Plant System," *International Journal of Phytoremediation*, 7, no. 1, 2005, pp. 3 - 17.

[20] J. T. Bushey, S. D. Ebbs and D. A. Dzombak, "Development of a Plant Uptake Model for Cyanide," *International Journal of Phytoremediation*, 8, no. 1, 2006, pp. 25 - 43.

[21] X.-Z. Yu, S. Trapp, P.-H. Zhou and L. Chen, "Effect of Temperature on the Uptake and Metabolism of Cyanide by Weeping Willows," *International Journal of Phytoremediation*, 9, no. 3, 2007, pp. 243 - 255.

[22] Y. Ouyang, "Modeling the Mechanisms for Uptake and Translocation of Dioxane in a Soil-Plant Ecosystem with Stella," *Journal of Contaminant Hydrology*, 95, no. 1-2, 2008, pp. 17-29.

[23] D. H. Greer, J. N. Wünsche, C. L. Norling and H. N. Wiggins, "Root-Zone Temperatures Affect Phenology of Bud Break, Flower Cluster Development, Shoot Extension Growth and Gas Exchange of 'Braeburn' (*Malus Domestica*) Apple Trees," *Tree Physiology*, 26, 2005, pp. 105-111.

[24] J.-w. Seo, D. Eckstein, R. Jalkanen, S. Rickebusch and U. Schmitt, "Estimating the Onset of Cambial Activity in Scots Pine in Northern Finland by Means of the Heat-Sum Approach," *Tree Physiology*, 28, no. 1, 2007, pp. 105-112.

[25] L. M. Hanks, T. D. Paine, J. G. Millar, C. D. Campbell and U. K. Schuch, "Water Relations of Host Trees and Resistance to the Phloem-Boring Beetle Phoracantha Semipunctata F. (Coleoptera: Cerambycidae)," *Oecologia*, 119, no. 3, 1999, pp. 400-407.

[26] C. A. Geiger and A. P. Gutierrez, "Ecology of Heteropsylla Cubana (Homoptera: Psyllidae): Psyllid Damage, Tree Phenology, Thermal Relations, and Parasitism in the Field.," *Environmental Entomology*, 29, no. 1, 2000, pp. 76-86.

[27] J. Sivinski, T. Holler, R. Pereira and M. Romero, "The Thermal Environment of Immature Caribbean Fruit Flies, *Anastrepha Suspensa* Diptera:Tephritidae)," *Florida Entomologist*, 90, no. 2, 2007, pp. 347-357.

[28] B. Wermelinger and M. Seifert, "Analysis of the Temperature Dependent Development of the Spruce Bark Beetle Ips Typographus (L.) (Col., Scolytidae)," *Journal of Applied Entomology*, 122, no. 4, 1998, pp. 185-191.

[29] H. Chen and M. Tang, "Spatial and Temporal Dynamics of Bark Beetles in Chinese White Pine in Qinling Mountains of Shaanxi Province, China," *Environmental Entomology*, 36, no. 5, 2007, pp. 1124-1130.

[30] P. Li and T. E. Martin, "Nest-Site Selection and Nesting Success of Cavity-Nesting Birds in High Elevation Forest Drainages," *The Auk*, 108, no. 2, 1991, pp. 405-418.

[31] M. C. Kalcounis and R. M. Brigham, "Secondary Use of Aspen Cavities by Tree-Roosting Big Brown Bats," *Journal of Wildlife Management*, 62, no. 2, 1998, pp. 603-611.

[32] K. L. Wiebe, "Microclimate of Tree Cavity Nests: Is It Important for Reproductive Success in Northern Flickers?," *The Auk*, 118, no. 2, 2001, pp. 412-421.

[33] C. Körner, "A Re-Assessment of High Elevation Treeline Positions and Their Explanation," *Oecologia*, 115, no. 4, 1998, pp. 445-459.

[34] C. Körner and G. Hoch, "A Test of Treeline Theory on a Montane Permafrost Island," *Artic, Antarctic, and Alpine Research*, 38, no. 1, 2006, pp. 113-119.

[35] S. Mayr, G. Wieser and H. Bauer, "Xylem Temperatures During Winter in Conifers at the Alpine Timberline," *Agricultural and Forest Meteorology*, 137, no. 1-2, 2006, pp. 81-88.

[36] M. Y. Bader, M. Rietkerk and A. K. Bregt, "Vegetation Structure and Temperature Regimes of Tropical Alpine Treelines," *Artic, Antarctic, and Alpine Research*, 39, no. 3, 2007, pp. 353-364.

[37] G. R. Fahenstock and R. C. Hare, "Heating of Tree Trunks in Surface Fires," *Journal of Forestry*, 62, 1964, pp. 799-805.

[38] R. G. Vines, "Heat Transfer through Bark, and the Resistance of Trees to Fire," *Australian Journal of Botany*, 16, 1968, pp. 499-514.

[39] L. P. Herrington, *A Theoretical and Experimental Investigation of the Temperature Field in Tree Stems*. Ph. D. thesis, Yale University, 1964.

[40] R. W. Derby and D. M. Gates, "The Temperature of Tree Trunks - Calculated and Observed," *American Journal of Botany*, 53, no. 6, 1966, pp. 580-587.

[41] J. R. Hummel, J. R. Jones, D. R. Longtin and N. L. Paul, "Development of a 3-D Tree Thermal Response Model for Energy Budget and Scene Simulation Studies," LTR 91-002, SPARTA, Inc., Lexington, MA, 1991.

[42] C. Doussan, G. Vercambre and L. Page, "Modelling of the Hydraulic Architecture of Root Systems: An Integrated Approach to Water Absorption--Distribution of Axial and Radial Conductances in Maize," *Annals of Botany*, 81, no. 2, 1998, pp. 225-232.

[43] J. R. Jones, "User's Guide for Treetherm: A 3-D Thermal Model for Single Trees," SCI-RPT 9, Sparta, Inc., Lexington, MA, USA, 1998.

[44] L. Wu, M. B. McGechan, N. McRoberts, J. A. Baddeley and C. A. Watson, "Spacsys: Integration of a 3d Root Architecture Component to Carbon, Nitrogen and Water Cycling--Model Description," *Ecological Modelling*, 200, no. 3-4, 2007, pp. 343-359.

[45] J. L. Jones, B. W. Webb, D. Jimenez, J. Reardon and B. Butler, "Development of an Advanced One-Dimensional Stem Heating Model for Application in Surface Fires," *Canadian journal of forest research*, 34, 2004, pp. 20-30.

[46] J. L. Jones, *Development of an Advanced Stem Heating Model*. Master of Science, Brigham Young University, 2003.

[47] T. R. Oke, *Boundary Layer Climates*, (London ; New York: Routledge), 1992.

[48] S. E. Howington, *Discrete Network Modeling for Field-Scale Flow and Transport through Porous Media*. Ph. D. thesis, University of Colorado, 1997.

[49] T. T. Kozlowski and S. G. Pallardy, *Physiology of Woody Plants*, (San Diego, CA: Academic Press), 1997.

[50] N. M. Holbrook and M. A. Zwieniecki, *Vascular Transport in Plants*, (Burlington, MA: Elsevier Academic Press), 2005.

[51] A. M. Gill and D. H. Ashton, "The Role of Bark Type in Relative Tolerance to Fire of Three Central Victorian Eucalypts," *Australian Journal of Botany*, 16, 1968, pp. 491-498.

[52] F. M. Turrell and S. W. Austin, "Comparative Nocturnal Thermal Budgets of Large and Small Trees," *Ecology*, 46, no. 1/2, 1965, pp. 25-34.

[53] F. M. Turrell, S. W. Austin, D. McNee and W. J. Park, "Thermal Conductivity of Functional Citrus Tree Wood," *Plant Physiology*, 42, no. 8, 1967, pp. 1025-1034.

[54] L. P. Herrington, *On Temperature and Heat Flow in Tree Stems*, (New Haven,: Yale University), 1969.

[55] C. R. Barnes, "The Significance of Transpiration," *Science*, 15, 1902, p. 460.

[56] E. D. Woodhouse, "Sap Hydraulics," *Plant Physiology*, 8, no. 2, 1933, pp. 177-202.

[57] R. H. Swanson, "Significant Historical Developments in Thermal Methods for Measuring Sap Flow in Trees," *Agricultural and Forest Meteorology*, 72, no. 1-2, 1994, pp. 113-132.

[58] D. C. Marshall, "Measurement of Sap Flow in Conifers by Heat Transport," *Plant Physiology*, 33, 1958, pp. 385-396.

[59] M. R. Kaufmann and P. J. Kramer, "Phloem Water Relations and Translocation," *Plant Physiology*, 42, no. 2, 1967, pp. 191-194.

[60] J. Cermak, E. Cienciala, J. Kucera and J.-E. Hallgren, "Radial Velocity Profiles of Water Flow in Trunks of Norway Spruce and Oak and the Response of Spruce to Severing," *Tree Physiology*, 10, 1992, pp. 367-380.

[61] A. Granier, T. Anfodillo, M. Sabatti, H. Cochard, E. Dreyer, M. Tomasi, R. Valentini and N. Breda, "Axial and Radial Water Flow in the Trunks of Oak Trees: A Quantitative and Qualitative Analysis," *Tree Physiology*, 14, 1994, pp. 1383-1396.

[62] A. Granier and D. Loustau, "Measuring and Modelling the Transpiration of a Maritime Pine Canopy from Sap-Flow Data," *Agricultural and Forest Meteorology*, 71, no. 1-2, 1994, pp. 61-81.

[63] A. Granier, P. Biron and D. Lemoine, "Water Balance, Transpiration and Canopy Conductance in Two Beech Stands," *Agricultural and Forest Meteorology*, 100, no. 4, 2000, pp. 291-308.

[64] N. Nadezhdina, H. Tributsch and J. Cermak, "Infra-Red Images of Heat Field around a Linear Heater and Sap Flow in Stems of Lime Trees under Natural and Experimental Conditions," *Annals of Forest Science*, 61, 2004, pp. 203-213.

[65] F. C. Meinzer, J. R. Brooks, J. C. Domec, B. L. Gartner, J. M. Warren, D. R. Woodruff, K. Bible and D. C. Shaw, "Dynamics of Water Transport and Storage in Conifers Studied with Deuterium and Heat Tracing Techniques," *Plant, Cell & Environment*, 29, no. 1, 2006, pp. 105-114.

[66] G. M. Dusinberre, *Heat Transfer Calculations by Finite Differences.*, (Scranton, PA: International Textbook Co.), 1961.

[67] F. C. Rego and E. Rigolot 1990 Heat Transfer through Bark: A Simple Predictive Model. In: *In Proceedings of the Third International Symposium on Fire Ecology*, ed J G Goldammer and M J Jenkins (Freiburg, Germany: SPD Academic Publishing) pp 157-161.

[68] B. E. Potter and J. A. Andresen, "A Finite-Difference Model of Temperatures and Heat Flow within a Tree Stem," *Canadian journal of forest research*, 32, no. 3, 2002, pp. 548-555.

[69] W. Simpson and A. TenWolde, "Physical Properties and Moisture Relations of Wood," *Wood Handbook - Wood as an Engineering Material*, (Madison, WI: U.S. Department of Agriculture, Forest Service, Forest Products Laboratory) 1999.

[70] R. E. Martin, "Thermal Properties of Bark," *Forest Products Journal*, 13, no. 10, 1963, pp. 419-426.

[71] I. R. Cowan, "Transport of Water in the Soil-Plant-Atmosphere System," *The Journal of Applied Ecology*, 2, no. 1, 1965, pp. 221-239.

[72] P. Farnum and G. F. Carey, "Moisture Transport in a Soil-Plant System: A Mathematical Model and Finite Element Analysis," *Advances in Water Resources*, 4, no. 2, 1981, pp. 67-76.

[73] J. S. Sperry, U. G. Hacke, R. Oren and J. P. Comstock, "Water Deficits and Hydraulic Limits to Leaf Water Supply," *Plant, Cell & Environment*, 25, no. 2, 2002, pp. 251-263.

[74] K. A. McCulloh, J. S. Sperry and F. R. Adler, "Water Transport in Plants Obeys Murray's Law," *Nature*, 421, no. 6926, 2003, pp. 939-942.

[75] J. S. Sperry, V. Stiller and U. G. Hacke, "Xylem Hydraulics and the Soil-Plant-Atmosphere Continuum: Opportunities and Unresolved Issues," *Agronomy Journal*, 95, no. 6, 2003, pp. 1362-1370.

[76] J. W. Deardorff, "Efficient Prediction of Ground Surface Temperature and Moisture, with Inclusion of a Layer of Vegetation," *Journal of Geophysical Research*, 83, no. C4, 1978, pp. 1889-1903.

[77] K. L. Bristow, G. S. Campbell, R. I. Papendick and L. F. Elliott, "Simulation of Heat and Moisture Transfer through a Surface Residue--Soil System," *Agricultural and Forest Meteorology*, 36, no. 3, 1986, pp. 193-214.

[78] G. S. Campbell and J. M. Norman, *An Introduction to Environmental Biophysics*, (New York: Springer-Verlag), 1998.

[79] G. D. Buchan, "Predicting Bare Soil Temperature. I. Theory and Models for the Multi-Day Mean Diurnal Variation," *European Journal of Soil Science*, 33, no. 2, 1982, pp. 185-197.

[80] I. Braud, A. C. Dantas-Antonino, M. Vauclin, J. L. Thony and P. Ruelle, "A Simple Soil-Plant-Atmosphere Transfer Model (Sispat) Development and Field Verification," *Journal of Hydrology*, 166, no. 3-4, 1995, pp. 213-250.

[81] I. Braud, N. Varado and A. Olioso, "Comparison of Root Water Uptake Modules Using Either the Surface Energy Balance or Potential Transpiration," *Journal of Hydrology*, 301, no. 1-4, 2005, pp. 267-286.

[82] C. L. Wu, K. W. Chau and J. S. Huang, "Modelling Coupled Water and Heat Transport in a Soil-Mulch-Plant-Atmosphere Continuum (Smpac) System," *Applied Mathematical Modelling*, 31, no. 2, 2007, pp. 152-169.

[83] J. F. Siau, *Transport Processes in Wood,* (New York: Springer-Verlag), 1984.

[84] J. D. MacLean, "Thermal Conductivity of Wood," *Heading, piping, and air conditioning*, 13, 1941, pp. 380-391.

[85] J. Siau, "A Geometrical Model for Thermal Conductivity," *Wood and Fiber Science,* 1, no. 4, 1970, pp. 302-307.

[86] J. F. Siau, *Flow in Wood,* (Syracuse, New York: Syracuse University Press), 1971.

[87] J. F. Siau, *Wood: Influence of Moisture on Physical Properties*, (Virginia Tech.: Department of Wood Science and Forest Products), 1995.

[88] B. M. Suleiman, J. Larfeldt, B. Leckner and M. Gustavsson, "Thermal Conductivity and Diffusivity of Wood," *Wood Science and Technology*, 33, no. 6, 1999, pp. 465-473.

[89] H. Gu, *Structure Based, Two-Dimensional, Anisotropic, Transient Heat Conduction Model for Wood.* Dissertation, Virginia Polytechnic Institute and State University, 2001.

[90] H.-m. Gu and A. Zink-Sharp, "Geometric Model for Softwood Transverse Thermal Conductivity. Part I," *Wood Science*, 37, no. 4, 2005, pp. 699-711.

[91] H. Gu and J. Hunt, "Two-Dimensional Finite Element Heat Transfer Model of Softwood. Part Ii. Macrostructural Effects," *Wood and Fiber Science,* 38, no. 4, 2006, pp. 599-608.

[92] H. Gu and J. Hunt, "Two-Dimensional Finite Element Heat Transfer Model of Softwood. Part Iii. Effect of Moisture Content on Thermal Conductivity," *Wood and Fiber Science*, 39, no. 1, 2007, pp. 159-166.

[93] Y. Hiraiwa and T. Kasubuchi, "Temperature Dependence of Thermal Conductivity of Soil over a Wide Range of Temperature (5-75 Deg C)," *European Journal of Soil Science,* 51, no. 2, 2000, pp. 211-218.

[94] P. Cosenza, R. Guérin and A. Tabbagh, "Relationship between Thermal Conductivity and Water Content of Soils Using Numerical Modelling," *European Journal of Soil Science*, 54, 2003, pp. 581-587.

[95] D. A. de Vries 1963 Thermal Properties of Soils. In: *Physics of plant environment.,* ed W R van Wijk (Amsterdam: North-Holland Publishing Company) pp 210-235.

[96] T. E. Ochsner, R. Horton and T. Ren, "A New Perspective on Soil Thermal Properties," *Soil Science Society of America Journal*, 65, no. 6, 2001, pp. 1641-1647.

[97] J. Côté and J.-M. Konrad, "A Generalized Thermal Conductivity Model for Soils and Construction Materials," *Canadian Geotechnical Journal*, 42, 2005, pp. 443-458.

[98] J. Côté and J.-M. Konrad, "Thermal Conductivity of Base-Course Materials," *Canadian Geotechnical Journal*, 42, 2005, pp. 61-78.

[99] O. Johansen, *Thermal Conductivity of Soils*. Ph.D., University of Trondheim, 1975.

[100] S. Lu, T. Ren, Y. Gong and R. Horton, "An Improved Model for Predicting Soil Thermal Conductivity from Water Content at Room Temperature," *Soil Science Society of America Journal*, 71, no. 1, 2007, pp. 8-14.

[101] L. Richards, "Capillary Conduction of Liquids through Porous Mediums," *Physics*, 1, no. 5, 1931, pp. 318-333.

[102] M. T. van Genuchten, "A Closed-Form Equation for Predicting the Hydraulic Conductivity of Unsaturated Soils," *Soil Science Society of America Journal*, 44, 1980, pp. 892-898.

[103] J. C. Tannehill, D. A. Anderson and R. H. Pletcher, *Computational Fluid Mechanics and Heat Transfer,* (New York: Taylor & Francis), 1997.

[104] M. F. Modest, *Radiation Heat Transfer,* (New York: Academic Press), 2003.

[105] R. Siegel and J. R. Howell, *Thermal Radiation Heat Transfer,* (Taylor and Francis, New York), 2002.

[106] S. E. Howington, J. F. Peters, J. R. Ballard, Jr., O. J. Eslinger, J. R. Fairley, R. V. Kala, R. A. Goodson, S. J. Price, A. M. Hines and L. D. Wakeley, "Using Computer Simulation to Explore the Importance of Hydrogeology in Remote Sensing for Explosive Threat Detection," *Military Aspects of Hydrogeology: Past and Present,* ed J D Mather and E P F Rose (London, UK: Geological Society of London, Special Publications) 2011.

[107] H. A. Van der Vorst, "Bi-Cgstab: A Fast and Smoothly Converging Variant of Bi-Cg for the Solution of Nonsymmetric Linear Systems," *SIAM Journal on scientific and Statistical Computing,* 13, 1992, p. 631.

[108] J. R. Howell, "The Monte Carlo Method in Radiative Heat Transfer," *Journal of Heat Transfer,* 120, 1998, pp. 547-560.

[109] M. F. Modest, "Backward Monte Carlo Simulations in Radiative Heat Transfer," *Journal of Heat Transfer,* 125, no. 1, 2003, pp. 57-62.

[110] J. E. Jones and C. S. Woodward, "Newton-Krylov-Multigrid Solvers for Large-Scale, Highly Heterogeneous, Variably Saturated Flow Problems," *Advances in Water Resources,* 24, no. 7, 2001, pp. 763-774.

[111] D. A. Knoll and D. E. Keyes, "Jacobian-Free Newton-Krylov Methods: A Survey of Approaches and Applications," *Journal of Computational Physics,* 193, no. 2, 2004, pp. 357-397.

[112] J. S. Liu, *Monte Carlo Strategies in Scientific Computing,* (New York: Springer Verlag), 2008.

[113] P. Hsu and H. Robbins, "Complete Convergence and the Law of Large Numbers," *Proceedings of the National Academy of Sciences of the United States of America,* 33, no. 2, 1947, p. 25.

[114] S. A. Dupree and S. K. Fraley, *A Monte Carlo Primer : A Practical Approach to Radiation Transport,* (New York: Kluwer Academic/Plenum), 2002.

[115] Y. Jaluria and K. E. Torrance, *Computational Heat Transfer,* (New York: Taylor & Francis), 2003.

[116] J. R. Ballard, Jr., J. A. Smith and G. G. Koenig, "Towards a High Temporal Frequency Grass Canopy Thermal Ir Model for Background Signatures," *Proceedings of the SPIE.* Orlando, FL, USA, 2004.

[117] G. E. Myers, *Analytical Methods in Conduction Heat Transfer,* (New York: McGraw-Hill), 1971.

[118] A. Bejan, *Convection Heat Transfer,* (Hoboken, New Jersey: John Wiley & Sons), 2004.

[119] F. P. Incropera, D. P. Dewitt, T. L. Bergman and A. S. Lavine, *Fundamentals of Heat and Mass Transfer,* (Hoboken, NJ: John Wiley & Sons), 2007.

[120] J. H. Gruninger, D. C. Robertson and M. M. Pervaiz, "Data Analysis for Bark and Leaf Reflectance Measurements," PL-TR-92-2151, Spectral Sciences, Inc., Burlington, MA, 1992.

[121] Harvard Forest. 2010. Fisher Meteorological Station. http://harvardforest.fas.harvard.edu/hfmet/. Oct. 4, 2010.

[122] National Renewable Energy Laboratory, Solar Radiation Research Laboratory. 2010. Baseline Measurement System. http://www.nrel.gov/midc/srrl_bms/. Oct. 4, 2010.

[123] H. Si 2006 On Refinement of Constrained Delaunay Tetrahedralizations. In: *Proceedings of the 15th International Meshing Roundtable,* (Birmingham, AL, USA: Springer) pp 509-528.

[124] M. Sezgin and B. Sankur, "Survey over Image Thresholding Techniques and Quantitative Performance Evaluation," *Journal of Electronic imaging*, 13, 2004, p. 146.

[125] J. R. Ballard, Jr. and J. A. Smith, "Hyperspectral Canopy Reflectance Modeling and Eo-1 Hyperion," *SPIE Conference 4725 on Algorithms and Technologies for Multispectral, Hyperspectral, and Ultraspectral Imagery VIII.* Orlando, FL, 2002.